UNIVERSITÉ DE MONTRÉAL

ELECTROLYTE-GATED TUNGSTEN OXIDE TRANSISTORS: FABRICATION, WORKING MECHANISM, DEVICE PERFORMANCE

XIANG MENG

DÉPARTEMENT DE GÉNIE PHYSIQUE

ÉCOLE POLYTECHNIQUE DE MONTRÉAL

THÈSE PRÉSENTÉE EN VUE DE L'OBTENTION

DU DIPLÔME DE PHILOSOPHIAE DOCTOR

(GÉNIE PHYSIQUE)

SEPTEMBRE 2017

UNIVERSITÉ DE MONTRÉAL

ÉCOLE POLYTECHNIQUE DE MONTRÉAL

Cette thèse intitulée :

ELECTROLYTE-GATED TUNGSTEN OXIDE TRANSISTORS: FABRICATION, WORKING MECHANISM, DEVICE PERFORMANCE

présentée par : MENG Xiang

en vue de l'obtention du diplôme de : Philosophiae Doctor

a été dûment acceptée par le jury d'examen constitué de :

M. YELON Arthur, Ph. D., président

Mme SANTATO Clara, Doctorat, membre et directrice de recherche

M. DESJARDINS Patrick, Ph. D., membre

Mme HEMMER Eva, Dr. Ing., membre

M. BEVAN Kirk Huw, Ph. D., membre externe

ACKNOWLEDGEMENTS

First and foremost, I would like to express my deepest thanks to my supervisor, Professor Clara Santato, for giving me the opportunity to work in the Advanced Electroactive Materials group, and for her inspiring enthusiasm, scientific guidance, support and encouragement during these last five years. This thesis would never have become reality without her. I also very much appreciate her moral support.

I thank Professor Francesca Soavi for her support and help during my pre-doctoral exam and for working with me on my first paper. I thank Professor Fabio Cicoira for the opportunity to access his lab and for his valuable advice and discussions.

Many thanks to all the colleagues that have contributed to my research projects over the last years. I am very grateful to Patricia Moraille for help in AFM, Dr. Josianne Lefebvre for support during XPS measurements, Christophe Clément for assistance in microfabrication, Dr. Nima Nateghi for assistance in XRD measurements, Dr. Marta Maria Natile for assistance in BET measurements and Dr. Samir Elouatik for assistance in Raman and ATR-FTIR measurements. I also want to thank Yves Drolet, Francis Boutet and Daniel Pilon for their technical assistance in the laboratory.

Not less important, I would also like to thank my other colleagues and friends, former and present, Francis, Frederic, Shuang, Hao, Dilek, Jonathan, Julia, Prajwal, Irina, Fanny, Gaia, Guido, Martin, Eduardo, Tian, Xu, Zhaojing and Mengjiao for their support and advice in my research or just interesting discussions outside the laboratory. I will always remember them with their warm hearts and big smiles. Special thanks to Michelle Alexandra Gaspard for proofreading the French abstract.

Financial support from the China Scholarship Council is gratefully acknowledged. I am also grateful to CMC Microsystems for the funding provided for microfabrication through programs MNT Financial Assistance and Solutions.

Furthermore, I am grateful to the jury members, Profs. Arthur Yelon, Patrick Desjardins, Kirk Bevan and Eva Hemmer for their time and interest in my work.

Thanks to my beloved parents, parents-in-law, sisters, for their unconditional love and support.

Finally, I would like to give a very special thanks to my beloved husband and colleague, Shiming Zhang. We went through all the good and bad moments together in the past 8 years. At last, I would never forget to mention my little one, Mark, who makes my life different!

RÉSUMÉ

Le transistor est l'un des composants clés des ordinateurs, des téléphones cellulaires intelligents, des moniteurs et d'autres produits électroniques qui ont affecté le progrès technologique et scientifique de notre société.

Ces dernières années, l'attention a été consacrée à l'étude des transistors utilisant la commutation électrolytique, au lieu de diélectriques solides conventionnels. Bien que l'utilisation d'électrolytes dans l'électronique ne soit pas un nouveau concept, la commutation électrolytique est importante pour le développement de l'électronique flexible et biocompatible.

Les transistors à commutation électrolytique ont, en effet, attiré l'attention en raison de leur faible tension d'alimentation (< 2 V) ainsi que de la possibilité d'obtenir une densité de charge aussi élevée que 10^{14}-10^{15} cm^{-2} en raison de la capacité élevée de l'interface électrolyte/canal du transistor (1-10 $\mu F \cdot cm^{-2}$). Mis à part leur intérêt technologique intrinsèque, les transistors à commutation électrolytique constituent aussi une plateforme expérimentale pour étudier des aspects fondamentaux. Ils sont en effet utilisés pour étudier le transport combiné électronique et ionique, le transport de charge à haute densité de charge et le contrôle électrique des transitions de phase.

Différents électrolytes ont été utilisés comme grille électrolytique, tels que des solutions aqueuses d'électrolyte, des polyélectrolytes, des polymères électrolytiques et des liquides ioniques. Parmi ceux-ci, les liquides ioniques se distinguent par leurs propriétés physico-chimiques uniques. En effet, les liquides ioniques peuvent être conçus pour posséder des caractéristiques de volatilité limitée, bonne conductivité ionique, faible viscosité, stabilité thermique élevée et large fenêtre de stabilité électrochimique (jusqu'à environ 5 V), en sélectionnant la structure appropriée pour le cation et l'anion.

Les oxydes métalliques sont de candidats prometteurs en tant que matériaux de canal pour les transistors à grille électrolytique. Les semi-conducteurs à base d'oxydes de métaux ont été intensément étudiés au cours des dernières décennies pour les transistors, en particulier pour des applications de type affichage, en raison de leur mobilité de charge élevée, de leur transparence optique, de leur stabilité chimique, facilité de mise en forme et faible coût.

Dans cette thèse, nous nous concentrons sur l'oxyde de tungstène qui peut être synthétisé par de simples méthodes en solution, est sensible à la lumière visible et présente de transitions intéressantes isolant-métal (métallisation).

Le noyau de cette thèse est consacré à une meilleure compréhension du mécanisme de fonctionnement des transistors à grille électrolytique à base d'oxydes de métaux, afin d'optimiser leurs performances et de développer de dispositifs optoélectroniques flexibles. Pour étudier le processus de dopage aux interfaces oxyde/électrolyte, une combinaison de voltammétrie cyclique, diffraction aux rayons X et caractérisation de type transistor, complétée par des études spectroscopiques (Raman et infrarouge), a été utilisée. Sur la base de cette étude, un mécanisme de fonctionnement pour les transistors à commutation électrolytique à base d'oxyde de tungstène nanostructuré a été proposé, impliquant le dopage électrostatique, le dopage électrochimique conventionnel et le dopage électrochimique confiné à l'interface.

L'effet de la température du traitement thermique de couches minces semiconductrices d'oxyde de tungstène sur la performance de phototransistors correspondants a été étudié. A cet effet, des couches minces d'oxyde de tungstène traitées thermiquement à 300 °C et 550 °C ont été caractérisées pour leur comportement transistor et phototransistor. En absence de lumière, les transistors à base de couches minces traitées à basse température (300 °C) ont montré des ratios ON/OFF plus élevés que celles traitées à haute température (550 °C). Sous illumination, les couches minces traitées à 550 ºC, sous vide, montrent un phénomène de photoconductivité persistante, limitant ainsi leur intérêt pour des applications de type phototransistor. D'autre part, les couches minces traitées à 300 °C, ne montrent pas de photoconductivité persistante.

Compte tenu des applications optoélectroniques, la principale contribution de cette thèse est le développement de phototransistors flexibles à commutation électrolytique. En particulier, en ce qui concerne les substrats de SiO_2, les dispositifs fabriqués sur un polyimide flexible présentent des performances améliorées en termes de rapport ON/OFF et de photosensibilité. Ces couches minces d'oxyde de tungstène traitées à basse température, caractérisées pour leur performance de type transistor, *photosensibilité* et *photoresponsivité*, sont prometteuses pour une nouvelle génération de détecteurs de lumière flexibles de grande surface.

Cette thèse fournit de nouvelles hypothèses sur le mécanisme de fonctionnement des transistors à commutation électrolytique. La thèse démontre aussi la nécessité de considérer les effets de la température du traitement thermique et de la nature du substrat sur la performance de phototransistors. Nos résultats et les techniques que nous avons employées ouvrent la voie à une compréhension globale de la dynamique complexe de dopage à l'interface entre les oxydes métalliques et les électrolytes.

ABSTRACT

Transistors are one of the key components in computers, smart cell phones, monitors and other electronics products, which have affected the technological and scientific progress of our society.

In recent years, attention has been dedicated to the study of electrolyte-gated transistors, which utilize electrolytes as the gating layer instead of conventional solid dielectric. Although the use of electrolytes in electronics is not a new concept, new printable, fast-response electrolytes are expanding the potential applications of electrolyte-gated transistors in flexible, rollable and biocompatible electronics.

Electrolyte-gated transistors are indeed attracting attention because of their low driving voltages (< 2 V) as well as the possibility of achieving charge carrier density as high as ca. $10^{14}-10^{15}$ cm^{-2}, owing to the high capacitance of the electrolyte/transistor channel interface (ca. 1−10 $\mu F \cdot cm^{-2}$). The intrinsic technological interest of electrolyte-gated transistors is paralleled by their relevance as experimental platforms to study fundamental aspects of electrochemistry, solid state physics and electronic engineering. Particular attention is devoted to combined electronic and ionic transport, charge carrier transport at high charge density and electrical control of phase transitions.

Different electrolytes have been used as gating media in electrolyte-gated transistors, such as aqueous electrolyte solutions, polyelectrolytes, electrolyte polymers and ionic liquids. Among these, ionic liquids stand out due to their unique physicochemical properties. Indeed, ionic liquids can be designed to exhibit limited volatility, good ionic conductivity, low viscosity, high thermal stability, and a wide electrochemical stability window (up to ca. 5 V) by appropriate choice of structure for the cation and anion.

Promising channel material candidates for electrolyte-gated transistors are metal oxides. Metal oxide semiconductors have been intensively investigated over the past decades for transistors, particularly in display applications due to their high charge carrier mobility, high optical transparency, chemical stability, low temperature processability and low cost. In this thesis, we focus on tungsten oxide that features solution processability, insulator-to-metal transition and visible light sensitivity.

The core of this thesis is devoted to a better understanding of the operational mechanism of ionic liquid-gated metal oxide transistors, to optimize their performance and to develop flexible

optoelectronics. To investigate the doping process at oxide/electrolyte interfaces, a combination of cyclic voltammetry, X-ray diffraction, and transistor performance characterizations, complemented by spectroscopic (Raman and infrared) investigations were employed. We correlated the metal oxidation state and the charge transport properties of the metal oxide. Based on this study, a working mechanism for the ionic liquid-gated tungsten oxide was proposed, involving the electrostatic doping as field-effect, conventional electrochemical doping and nonconventional interface-confined electrochemical doping.

The effect of the thermal treatment temperature of the tungsten oxide semiconducting films on corresponding (photo)transistor performance was demonstrated. For this purpose, 550 °C and 300 °C thermally treated tungsten oxide films were characterized for their transistor and photoresponse behavior. In dark condition, low temperature (300 °C) tungsten oxide electrolyte-gated transistors showed higher ON/OFF ratios than high temperature (550 ºC) ones due to the amorphous structure. Under illumination, films treated at 550 ºC, operated in vacuum conditions, show persistent photoconductivity, thus limiting their interest for phototransistor applications. On the other hand, films treated at 300 °C, are persistent photoconductivity-free.

In view of optoelectronics applications, the main contribution of this thesis is the development of flexible electrolyte-gated phototransistors. In particular, with respect to SiO_2 substrates, devices fabricated on flexible polyimide show improved performance in terms of ON/OFF ratio and photosensitivity. These low temperature tungsten oxide films, characterized for their transistor, photosensitivity and photoresponsivity behavior, are promising for a new generation of large-area light detectors.

This thesis provides new insights into the working mechanism of electrolyte-gated transistors. It demonstrates the necessity to consider the effects of film thermal treatment temperatures and substrates on the device performance. Our findings and the techniques we employed pave the way for a comprehensive understanding of complex doping dynamics at the interface between metal oxide films and electrolytes and for developing flexible electronics.

TABLE OF CONTENTS

LIST OF TABLES

LIST OF FIGURES

LIST OF SYMBOLS AND ABBREVIATIONS

Beti	Bis(pentafluoroethylsulfonyl)imide
BMIM	1-butyl-3- methylimidazolium
BMMIM	1-buyl-2,3-dimethylimidazolium
c	Light speed
CBM	Conduction band minimum
C_0	Specific capacitance
CMOS	Complementary metal–oxide–semiconductor
CPU	Central processing unit
c-Si	Crystalline silicon
CV	Cyclic voltammetry
d	Dielectric thickness
D_{e-}	Electron diffusion coefficient
DEME	N, N-diethyl-N-(2-methoxyethyl)-N-methylammonium
D_{M^+}	Ion (M^+) diffusion coefficient
DOS	Density of state
e	Elementary charge
E	Electric field
E_C	Conduction band energy
ECT	Electrochemical transistor
EDL	Electrical double layer
EDLT	Electrical double layer transistor
E_F	Fermi level
E_{Fi}	Intrinsic Fermi level

E_g	Bandgap
EG	Electrolyte-gated
EMI	1-ethyl-3-methyl imidazolium
EMIM	1-ethyl-3-methylimidazolium
EMMIM	1-ethyl-2,3-dimethylimidazolium
E_V	Valance band energy
f	Frequency of the ac perturbation
FAP	Tris(perfluoroethyl)trifluorophosphate
FET	Field-effect transistors
g_m	Transconductance
h	Planck constant
H	Hydrogen
HMIM	1-hexyl-3-methylimidazolium
HMDS	Hexamethyldisilazane
I_{ds}	Source-drain current
I_{dsat}	Saturation source-drain current
IL	Ionic liquid
Im	bis(triflouromethylsulfonyl)amide
I_{off}	Off state current
I_{on}	On state current
ITO	Indium tin oxide
JFET	Junction field effect transistors
L	Channel length
MEH-PPV	Poly[2-methoxy-5-(2-ethylhexyloxy)-1,4-phenylenevinylene]

MO	Metal oxide
MOSFET	Metal–oxide–semiconductor field-effect transistor
NMP	N-methyl pyrrolidone
NPN	p-Si bulk, n-doped Si electrodes
OTf	Trifluoromethanesulfonate
p	Charge carrier density
P13	N-methyl-N-propyl-pyrrolidinium
P14	1-butyl-1-methylpyrrolidium
P3HT	Poly(3-hexylthiophene-2,5-diyl)
PEG	Poly (ethylene glycol)
PEN	Polyethylene naphthalate
PF6	Hexafluorophosphate
PNP	n-Si bulk, p-doped Si electrodes
PQT-12	Poly (3,3‴-didodecylquaterthiophene
PVDF	Polyvinylidene fluoride
Q	Doping charge
RC	Resistor-capacitor
S	Subthreshold swing
TCB	Tetracyanoborate
TFSI	Bis(trifluoromethylsulfonyl)imide
TFT	Thin film transistor
T_{MI}	Metal-insulator transition temperature
VBM	Valence band maximum
V_{ds}	Source-drain voltage

V_{gs}	Gate-source voltage
V_{th}	Threshold voltage
W	Channel width
α	Absorption coefficient
μ_n	Electron mobility
ν	Photon frequency
υ_n	Electron drift velocity
ε_0	Vacuum permittivity
ε	Relative permittivity of dielectric
λ	Wavelength

LIST OF APPENDICES

CHAPTER 1 INTRODUCTION

In this chapter, we give a brief overview of transistor technology as well as the structure and the working principle of metal oxide semiconductor field-effect transistors, MOSFET, to provide the background needed to understand the scientific and technological findings of this PhD thesis. Electrolyte gating principles are also discussed. Research issues, motivation, main objective, specific objectives and organization of the work are included.

History of transistors

Two revolutionary historic events changed the communication between human beings. The first one, the "Age of Discovery," started in the early 15th century and continued to the 17th century. During this period, Europeans explored Africa, America, Asia and Oceania, connecting humans geographically. The second one is the development of the "Internet" in the early 1960s, which rapidly spread to the whole world, and connected and synchronized our thinking.[1] Mobile electronic devices are the carriers of the Internet and the "brain" of mobile devices is the central processing unit (CPU). The CPU contains billions of tiny field-effect transistors (FET) to manipulate the flow of electrons in semiconductors, to allow the processing or storage of information. In 1926, the first FET was patented by Lilienfeld but FET failed to achieve fame at that time because of the poor quality of semiconductor materials.[2] In 1950, the more practical junction FET (JFET) was invented by the Japanese engineers Nishizawa and Watanabe.[3] In 1952, the researchers Bardeen, Brattain, and Shockley of Bell Labs independently invented the JFET.[4] In particular, Shockley's attempt to commercialize the FET in the 1950s led to California's "Silicon Valley" that became a hotbed of electronics innovation. Finally, in 1956, these three scientists were jointly awarded the Nobel Prize in Physics for "their researches on semiconductors and their discovery of the transistor effect."[5] In 1959, Kahng and Atalla at Bell Labs invented the MOSFET.[6] Since then, MOSFET has become the most common transistor used in digital circuits. Two complementary configurations of MOSFET, the n-channel MOSFET and the p-channel MOSFET, were then fabricated.[7] Electronic circuit design becomes very versatile when these two types of devices are used in the same circuit. These circuits are referred to as complementary MOS (CMOS) circuits. Millions of CMOS FET integrated together build the basic units of a memory chip, microprocessor and CPU, which are the fundamental units of the electronics we are using now, such as cameras, smart phones and the computers.

Transistors, featuring different structures, are presently experiencing an explosive evolution towards lightweight, flexible, stretchable and biocompatible electronics, e.g. for next-generation wearable and textile integrated systems,[8-10] flexible and rollable displays,[11, 12] medical implants[13] and artificial skin.[14, 15]

1.1 Introduction to MOSFET

1.1.1 Working principle of MOSFET

Here we will discuss the working principle of the MOSFET, which is important to understand the content of this thesis. The core of a MOSFET is analogous to a capacitor where one plate is the gate electrode and the other plate is the semiconductor (Figure 1-1). A dielectric layer is sandwiched between these two plates. For a PNP MOSFET, when we apply a negative electrical bias to the gate, positive charge accumulates on the semiconductor side. In the case of the N-silicon channel shown in Figure 1.1, this happens via hole transport from the bulk of the semiconductor to the interface with the dielectric.

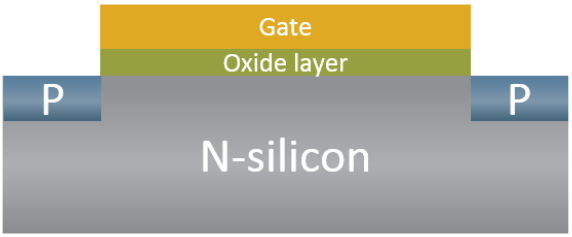

Figure 1-1 Basic structure of a PNP MOSFET showing gate, bulk (n-Si), source (p-doped Si) and drain (p-doped Si) electrodes. The gate is separated from the bulk semiconductor by an oxide layer.

The hole accumulation at the dielectric/semiconductor interface can be related to the energy level bending, as shown in Figure 1-2. For n-Si, upon application of a positive bias at the gate, the conduction band (E_C), valence band (E_V), and the intrinsic Fermi energy (E_{Fi}) levels all "bend down" (Figure 1-2a). Therefore, E_c is closer to the Fermi level (E_F), indicating a higher electron density at the interface with the dielectric. Analogously, when we apply a negative bias, a corresponding positive net charge will be induced at the n-silicon/dielectric interface. The positive

charge “bends up” the energy levels so that E_V is closer to E_F, indicating a higher hole density in the channel (Figure 1-2b).

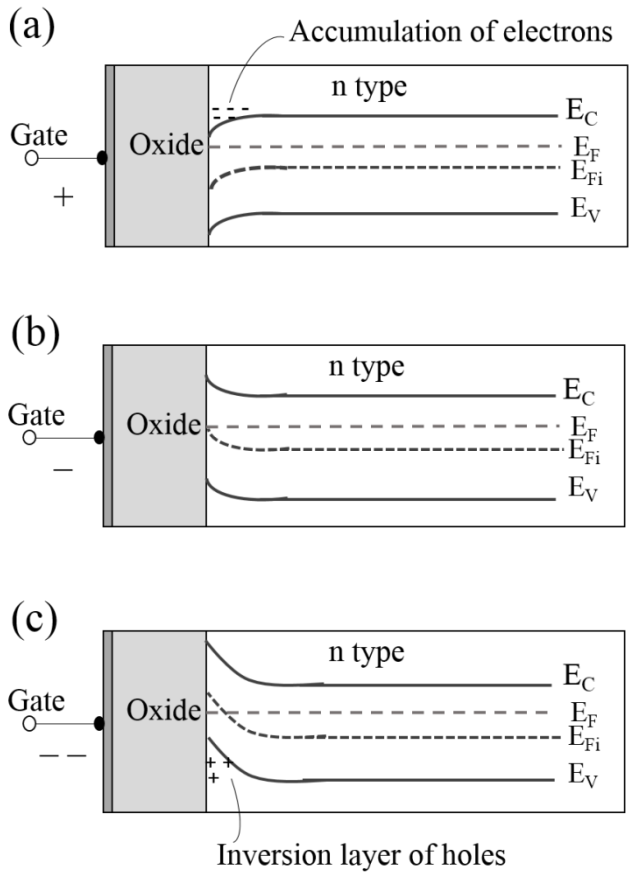

Figure 1-2 The energy-band diagram of a PNP MOSFET under (a) an applied positive gate bias, (b) a moderate negative gate bias, and (c) a “large” negative gate bias.

When we continue to increase the negative bias, the bands will bend up more strongly. When a sufficiently large bias is applied, the E_{Fi} can bend above E_F. This is of great importance since it means the holes became the majority charge carrier at the interface. In this case, the conduction type in n-Si at the interface with the insulator has been inverted from n- to p-type (Figure 1.2c). This p-type surface layer is induced not by chemical doping but simply by applying an electrical bias to the gate (electrostatic doping). An analogous mechanism is applicable to NPN MOSFET in which the conduction type in the p-Si can be inverted from p- to n-type. The inversion layer is the

key to MOSFET operation because it creates a connection between source and drain electrodes, creating current flow between them (Figure 1-3).

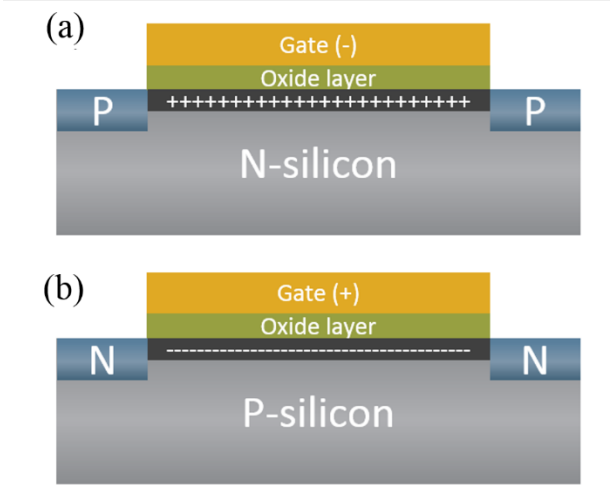

Figure 1-3 Inversion layer formed (a) at the n-Si/dielectric interface in a PNP MOSFET induced by applying a large negative bias at the gate; and (b) at the p-Si/dielectric interface in an NPN MOSFET induced by applying a large positive bias.

1.1.2 Voltage-current characteristics of MOSFET

For an NPN MOSFET, the n-type source and drain regions are diffused into a lightly doped p-type substrate and an oxide layer separates the gate electrode from the semiconductor. No significant current flows from source to drain without applying gate voltage (V_{gs}). When a positive V_{gs} is applied, the electron concentration increases in the channel. If we further increase V_{gs}, an inversion layer forms and the channel changes to n-type. The minimum V_{gs} required to invert the semiconductor from p-type to n-type is called threshold voltage (V_{th}). When $V_{gs} = V_{th}$, a current flow occurs from the source to the drain. However, actually, V_{gs} should be larger than V_{th} because of the presence of the source-drain voltage, V_{ds}.

In the following, we will discuss in detail the operation of an NPN MOSFET. An analogous behavior, taking into account the opposite polarities, is observed with PNP MOSFET.

i) Cut-off region of the transistor ($V_{gs} < V_{th}$)

In the cut-off region, as $V_{gs} < V_{th}$, the electron density increases because of the action of V_{gs}, but the surface of the semiconductor is either still p-type or a depletion layer is formed. In this mode, there

is negligible current flow from source to drain. However, when we shrink the device dimension (the channel length), the diffusion and drift of the electrons from the source electrode will result in a significant increase of the transistor current even when $V_{gs} < V_{th}$. In this case, the device works in the subthreshold region (details will be discussed later).

ii) Linear region ($V_{gs} > V_{th}$ and $V_{ds} < V_{gs} - V_{th}$)

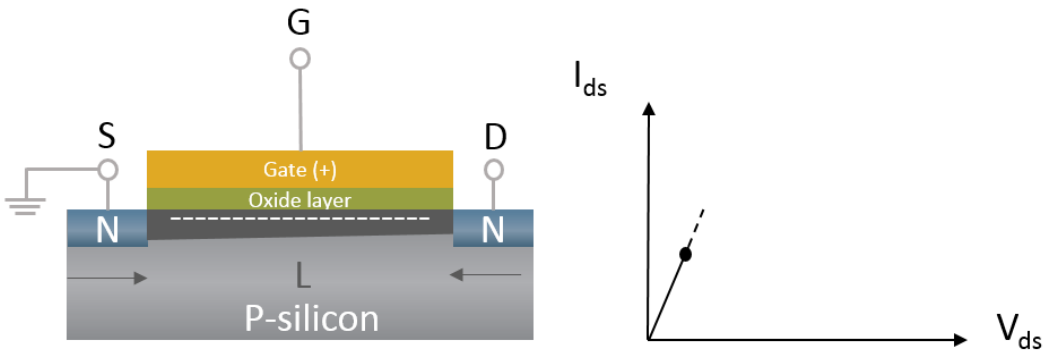

Figure 1-4 I_{ds} vs V_{ds} profile in the linear region of the NPN MOSFET represented in the scheme included in the figure. The black region in the scheme indicates the inversion layer thickness across the channel.

When we increase V_{gs}, an inversion layer forms at the interface and an n-type conducting channel is induced. Electrons are able to flow from the source to the drain upon application of a small V_{ds}. In this case, the channel behaves like a resistor. I_{ds} increases linearly with V_{ds} (Figure 1-4). The I_{ds} profile can be described by equation (1):

$$I_{ds} = C_0 \mu_n \frac{W}{L} (V_{gs} - V_{th}) V_{ds} \qquad (1)$$

Where $C_0 = \varepsilon_0 \varepsilon / d$ is the dielectric specific capacitance, ε_0 is the permittivity of the vacuum and has the value of 8.85×10^{-12} F·m^{-1}, ε is the relative permittivity for a given gate dielectric material, d is the thickness of the dielectric, μ_n is the electron mobility, W is the channel width and L is the channel length.

iii) Channel pinch-off ($V_{ds} = V_{gs} - V_{th}$)

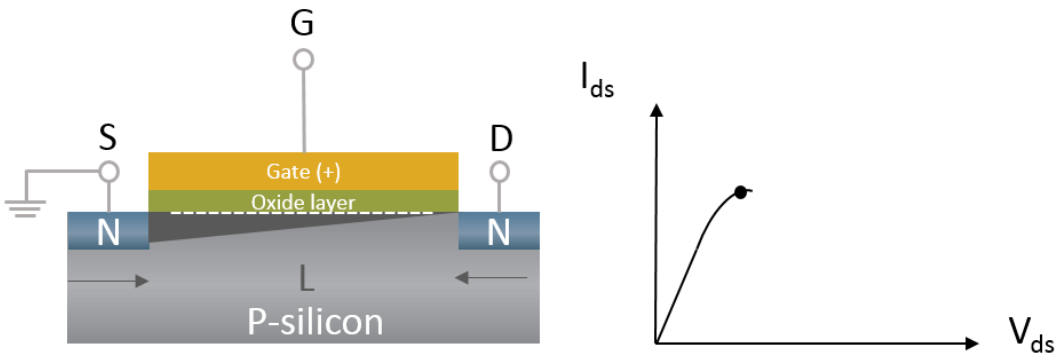

Figure 1-5 I_{ds} vs V_{ds} profile of the MOSFET represented in the scheme included in the figure, working at the pinch-off point. The black region in the device scheme indicates the inversion layer thickness across the channel.

Pinch-off is a key phenomenon in MOSFET. The effective voltage drop at the semiconductor/insulator interface is $V_{gs} - V_{ds}$. When V_{ds} is small, $V_{gs} - V_{th} >> V_{ds}$, device works in the linear region. However, when we further increase V_{ds} until $V_{gs} - V_{th} = V_{ds}$, the inversion layer thickness at the drain electrode will become zero. This is the channel pinch-off (Figure 1-5). The minimum V_{ds} required for the channel pinch-off is named $V_{d\,sat}$, and the corresponding I_{ds} is named $I_{d\,sat}$.

iv) Saturation region ($V_{gs} - V_{th} < V_{ds}$)

When V_{ds} further increases and $V_{ds} > V_{gs} - V_{th}$, the pinch-off point moves towards the source electrode (Figure 1-6). The additional voltage $V_{ds} - V_{d\,sat}$ drops only on the pinch-off region (space charge region). The extension of the pinch-off region increases with increasing V_{ds}, but because the space charge region has much higher resistance compared to the inversion layer and much smaller length (ΔL) compared to the total channel length (L), the electrical field $E = (V_{ds} - V_{d\,sat})/\Delta L$ is very strong. In this case, electrons flow in the channel from the source through the inversed channel toward the drain; they are then injected into the pinch-off area, where they are quickly swept by the strong E (even though the region is non-conductive) to the drain electrode. When we further increase V_{ds}, I_{ds} will saturate since the additional voltage applied ($V_{ds} - V_{d\,sat}$) will be absorbed by the pinch-off area (ΔL). For $V_{ds} > V_{d\,sat}$, the current does not change and $V_{d\,sat}$ can be described as follows:

$$V_{dsat} = V_{gs} - V_{th} \tag{2}$$

Considering the channel length L –ΔL ≈ L, the current-voltage profiles in equation (1) can be described by:

$$I_{dsat} = \frac{\mu_n C_0 W}{2L}\left(V_{gs} - V_{th}\right)^2 \tag{3}$$

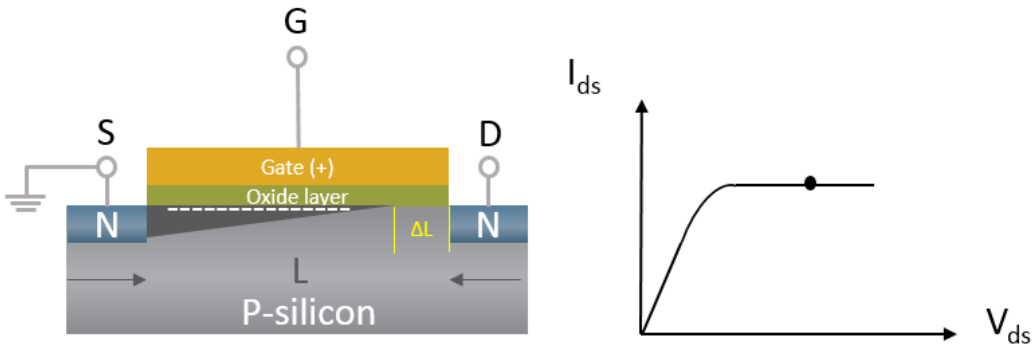

Figure 1-6 I_{ds} vs V_{ds} profile of the MOSFET represented in the scheme included in the figure, working in the saturation region. The black region of the scheme indicates the inversion layer thickness across the channel. ΔL indicates the length of the pinch-off extension.

v) Breakdown region

When V_{ds} reaches higher values than the reverse breakdown voltage for the PN junction at the drain region, the saturation current sharply increases and MOSFET starts to work in the breakdown region (Figure 1-7). This situation should be prevented since in most cases, the voltage-current characteristics are non-reversible and may destroy the MOSFET.

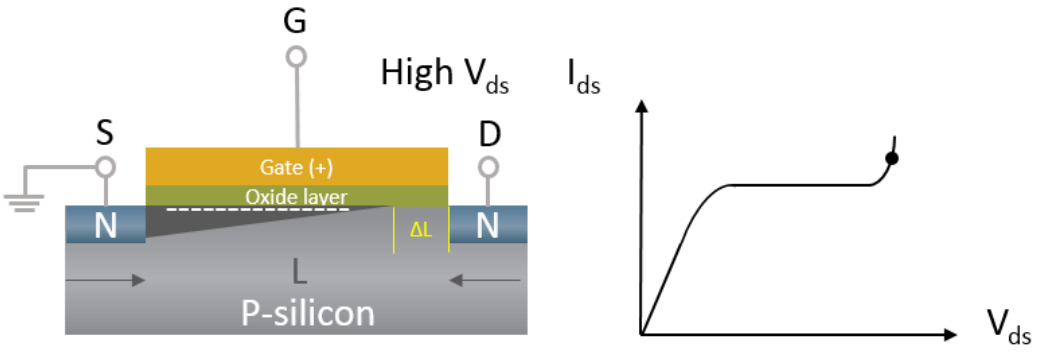

Figure 1-7 I_{ds} vs V_{ds} profile of the MOSFET represented in the scheme included in the figure, working in the breakdown region.

1.1.3 Transfer characteristics of MOSFET

The transfer characteristics relate I_{ds} to the input V_{gs}, at constant V_{ds}. When $V_{gs} < V_{th}$, the device works in the cut-off region, so the transistor current is negligible. When $V_{gs} > V_{th}$, I_{ds} increases with increasing V_{gs} due to the channel inversion (Figure 1-8).

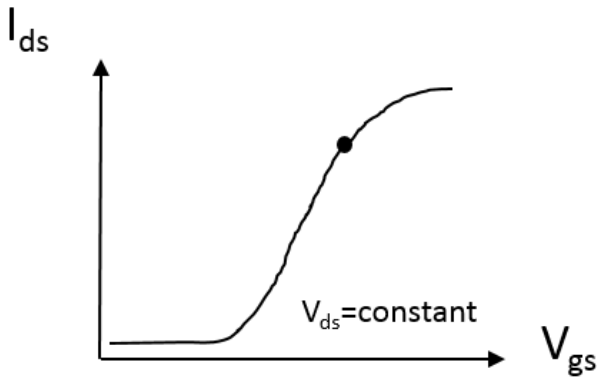

Figure 1-8 Illustration of a typical transfer curve (I_{ds} vs V_{gs}) of a MOSFET.

1.1.4 Short channel effect and subthreshold region

The assumption, $L - \Delta L \approx L$, for devices working in the saturation region is a good approximation only for long channel MOSFET. However, when the device dimension shrinks (e.g. the Intel 22 nm technology)[16] the channel length becomes very small. As a result, the ratio $\Delta L/L$ dramatically

increases and causes a considerable decrease in the effective channel length. This is the channel length modulation effect. In this case, the effective channel length L – ΔL decreases with increasing V_{ds} and consequently results in a resistance decrease. Thus, following equation (1), I_{ds} increases with V_{ds} and does not show saturation as V_{ds} increases. This is the short-channel effect. In the cut-off region, we discussed that the I_{ds} is negligible. This is a good approximation for long-channel devices. Taking the example of an NPN MOSFET, when the channel length decreases, the electrons from the source region can diffuse into the weak inversion layer ($V_{gs} < V_{th}$). In the weak inversion layer, the hole concentration decreases, so the electrons can travel through the P channel and can be collected by the drain region. As a result, a short channel device works even in the cut-off region ($V_{gs} < V_{th}$), i.e. there is I_{ds} flow in the device. Short-channel devices working in this mode are called to work in subthreshold mode.

1.1.5 Figures of merit of MOSFET

ON/OFF ratio: In a MOSFET, the saturation current (I_{dsat}) is referred to as the on-state current, I_{on}. The leakage current (cut-off region) is referred to as off-state current, I_{off}. I_{on}/I_{off} is the ON/OFF ratio. A high I_{on}/I_{off} indicates good switching properties, which is required for digital circuits application. In particular, a low I_{off} is needed in real devices. A small leakage current through the channel means that the device consumes less electricity, i.e. it requires a low standby power.

Transconductance: It is the change in I_{ds} with respect to the corresponding change in V_{gs}, expressed as follows:

$$g_m \equiv \frac{\partial I_{ds}}{\partial V_{gs}}\Big|_{Vds=\text{const}} \tag{4}$$

It indicates the I_{ds} sensitivity to V_{gs}; it is an important parameter, e.g. for sensor applications of transistors. Following equation (1), the g_m in the linear region is obtained:

$$g_m \equiv \frac{\partial I_{ds}}{\partial V_{gs}}\Big|_{V_{ds}=\text{const}} = C_0 \mu_n \frac{W}{L} V_{ds} \tag{5}$$

Following equation (3), the g_m in the saturation region is obtained:

$$g_m \equiv \frac{\partial I_{ds}}{\partial V_{gs}}\Big|_{V_{ds}=\text{const}} = \frac{C_0 \mu_n W}{L}\left(V_{gs} - V_{th}\right) \tag{6}$$

Mobility: In a semiconductor, the electron drift velocity (υ_n) is proportional to the applied electric field (E).

$$v_n = \mu_n E \tag{7}$$

The proportionality factor (μ_n) is the electron mobility, with units of $cm^2\ V^{-1}\ s^{-1}$. A high mobility is attractive for high frequency electronic devices.

The V_{th} and the mobility μ_n of semiconductor in a MOSFET can be calculated by linear fitting the equation (5). In the saturation region, both V_{th} and μ_n can be obtained by fitting the $I_{ds}^{1/2}$ versus V_{gs} using equation (3) as:

$$\sqrt{I_{dsat}} = \sqrt{\frac{\mu_n C_0 W}{2L}}\left(V_{gs} - V_{th}\right) \tag{8}$$

The slope permits us to extract μ_n and the intercept of I_{ds} at the V_{gs} axis permits us to extract V_{th}. μ_n is usually different from the intrinsic mobility of bulk material. This is because charge transport in MOSFET occurs in a narrow channel region close to the gate dielectric/semiconductor interface, where different sources of scattering are happening, such as Coulomb scattering from dielectric charges, surface roughness scattering and others.[17]

Subthreshold swing: As previously discussed, for a MOSFET, when there is a small increment in V_{gs}, a weak inversion layer changes to strong inversion layer and the device starts to work in the linear region. The subthreshold swing, which reflects the change of V_{gs} required to increase I_{ds} by an order of magnitude in the subthreshold region, is described by the following equation:

$$S \equiv \frac{dV_{gs}}{d\left(\log I_{ds}\right)} \tag{9}$$

A small subthreshold swing demonstrates a fast transition between the ON state and OFF state of a MOSFET, thus it is an important parameter in digital circuits or electrical switches that use ON (0) and OFF (1) as the fundamental units.

For more details of MOSFET model establishment, theory, equation derivation, one can refer to classic books on semiconductor physics and devices.[18-20]

1.1.6 Thin film transistors

The thin film transistor (TFT) is a special kind of field-effect transistor where the semiconductor is deposited as a thin film on an insulating substrate, such as glass or plastic. The first thin film FET was developed at RCA laboratories by Weimer in 1961 with polycrystalline cadmium sulphide (CdS) as the semiconducting thin film and silicon monoxide (SiO) as the dielectric.[21] Semiconductors used in TFT are commonly amorphous silicon and polysilicon.[22] Cadmium selenide,[23] metal oxides[17, 24, 25] and organic materials[26, 27] have also been widely used. The working principle of TFT refers to that of a MOSFET. One of the differences between the two types of transistors is that the source and drain regions are made of metal electrodes (rather than heavily doped p(n)-type regions in the n(p)-type substrate) so that the p(n)-type inversion layer is not needed to connect the p(n)-type source and drain regions. In this Ph. D. thesis, we will study metal oxide TFT, working in n-type accumulation mode.

Figure 1-9 shows four common device configurations used for TFT. The figure includes: (a) top gate (gate deposited on top of the dielectric), top source-drain contact (the contacts are deposited atop the semiconductor); (b) top gate, bottom contact (the contacts are deposited under the semiconductor); (c) bottom gate (dielectric deposited on top of the gate), top source-drain contact and (d) bottom gate, bottom source-drain contact. Selecting a proper device configuration is important since the configuration can affect the morphology of the channel material, the charge carrier mobility and other device characteristics.

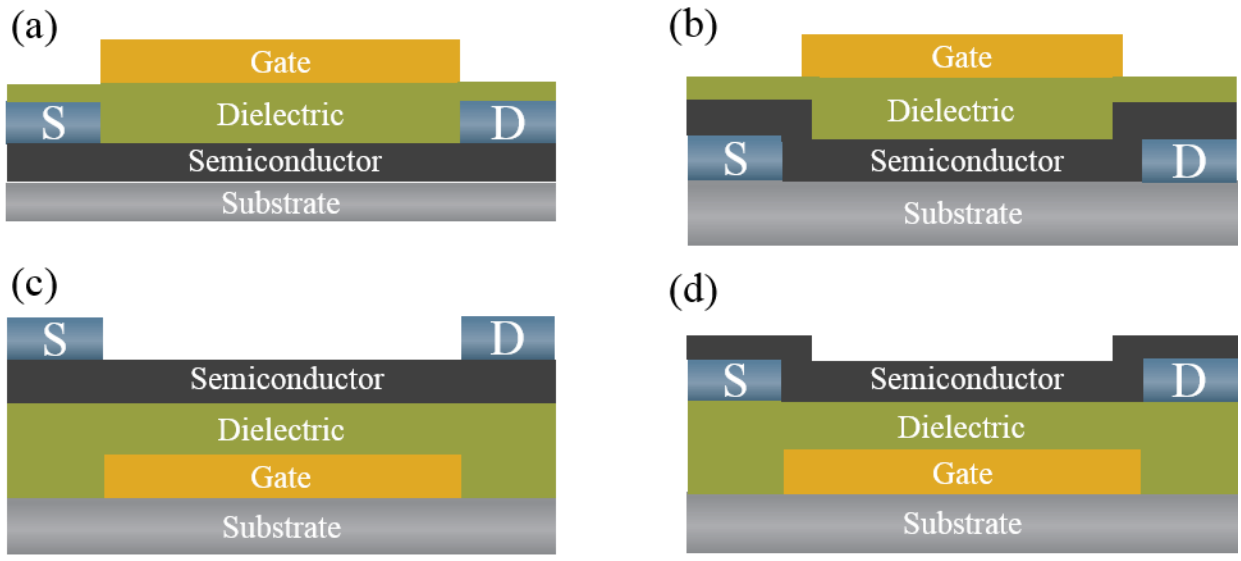

Figure 1-9 TFT structures: a) top gate, top source-drain contact; b) top gate, bottom source-drain contact; c) bottom gate, top source-drain contact; and d) bottom gate, bottom source-drain contact.

1.2 From FET to electrolyte-gated transistors (EGT)

Using transistors for applications such as in vivo,[28, 29] wearable[30, 31] and low power consumption requires transistors operating at low voltage.[32] To decrease the operation voltage, a high capacitance gate dielectric layer is needed. Towards this goal, many different strategies can be used, such as reducing the thickness of the gate dielectric and employing a high permittivity (κ) gate dielectric material.[33] The former strategy is often accompanied by a high leakage current; a decreased charge carrier mobility has been frequently reported for the latter,[34] due to additional energetic disorder that enhances charge carrier localization.

An interesting way to achieve high capacitance is electrolyte-gating, i.e. the use of electrolytes and ion including media (e.g. ionic liquids) as the gating medium. The key concept behind electrolyte-gating is the electric double layer (see Section 2.3). The capacitance of electrical double layers is typically on the order of 10 μF/cm^2, which makes it possible to operate electrolyte-gated transistor (EGT) at relatively low gate voltages (< 2 V) achieving large charge carrier densities (~10^{15} cm^{-2}) in the channel. This high charge carrier density explains the significant impact of EGT in solid-state physics; EGT enable novel functions and properties, which are extremely difficult or even impossible in conventional all-solid electronic devices (see section 2.4).

As in conventional FET, the gating dielectric, electronically insulating yet ionically conductive, is used to bridge the gap between the metal gate electrode and the channel. The redistribution of the ions at the electrode/electrolyte and electrolyte/channel interfaces upon application of gate voltage results in accumulation (depletion) of charge carriers in the channel. In terms of operating mechanism, EGT can be divided, at least, into two kinds of transistors, i.e. electrical double layer transistors (EDLT) and electrochemical transistors (ECT).[35] In case of EDLT, the semiconductor channel is impermeable to the ions of the electrolyte. Therefore, the application of an electrical bias to the gate electrode will cause migration of ions at the electrolyte/gate and electrolyte/semiconductor interfaces, paralleled by accumulation/depletion of charge carriers in the transistor channel, at the interface with the electrolyte (Figure 1-10a).[36] The resulting doping is electrostatic. In ECT, the semiconductor channel material allows the ions to enter the film (Figure1-10b). A reversible electrochemical doping (dedoping) process takes place. The doping/dedoping process is responsible for the conductivity change of the channel. Beside these two mechanisms, in 2013, Parkin et al. reported a different operating mechanism for metal oxide EGT. They found that the strong electric field between the ionic liquid gating medium 1-hexyl-3-methylimidazolium bis(trifluoromethylsulfonyl)-imide (HMIM-TFSI) and the VO_2 channel material induces oxygen vacancies in the VO_2 channel.[37] These results demonstrate that EGT permit the study of electronic phase transitions of metal oxide semiconductors.

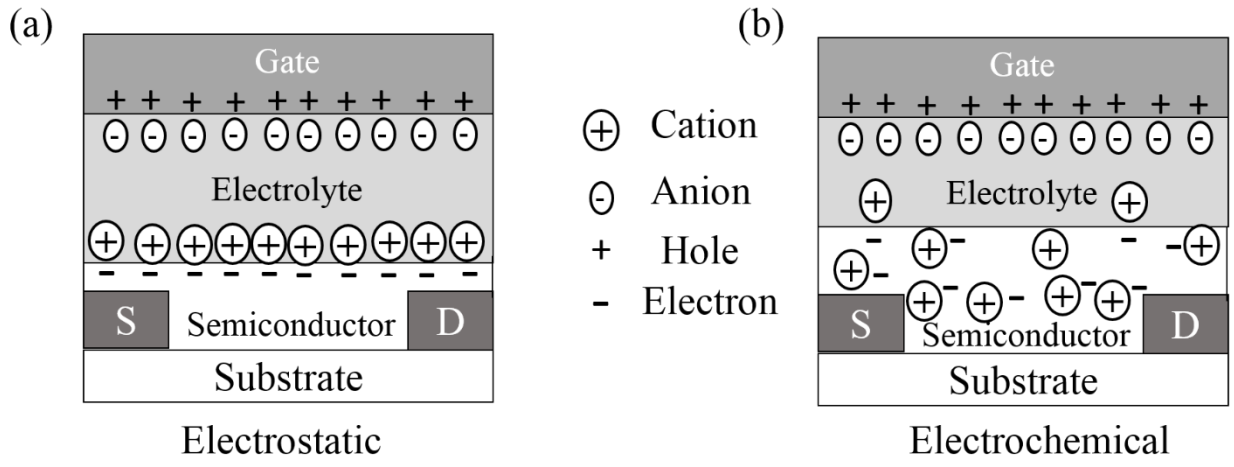

Figure 1-10 Working mechanism of an electrolyte-gated n-type transistor based on (a) electrostatic and (b) electrochemical doping mechanism.

1.3 Research issue

Despite the growing interest in EDLT and ECT, the physicochemical processes determining the device characteristics are still not well understood.

In particular, the nature of the electrical double layer at the interface between ionic media and porous semiconductors, e.g. nanostructured metal oxides, is still largely undiscovered. This type of interface is much more complex than a geometrically well-defined interface because the electrolyte can penetrate into the porous semiconductor. A slightly different doping mechanism can be hypothesized for these materials, in addition to electrostatic and conventional electrochemical doping, i.e. electrochemical doping confined at the electrolyte/metal oxide interface, especially for electrolytes made up of ions with relatively large size (e.g. ionic liquids), which may not be able to be inserted in the oxide lattice. Therefore, an in-depth study of the working mechanism of EGT based on nanostructured metal oxide channels and ionic liquid gating media could help to advance the knowledge of the doping mechanism at the fundamental level.

From an application point of view, while EGT offer great potential for flexible electronics, fabrication of high performance transistors with low processing temperature (e.g. 150 ºC in the case of polyethylene naphthalate (PEN) and 350 ºC for polyimide) is still a challenge. In addition, even though EGT have been used in logic circuits and memory devices, little is known about their application in optoelectronics, e.g. light-emitting transistors and phototransistors.

1.4 Motivation

Among metal oxide semiconductors, tungsten oxide is a promising material for applications such as electrochromic displays,[38, 39] gas sensors[40] and photodetectors[41]. Electrolyte gating is attracting growing interest for low operating voltage < 2 V transistors and high charge carrier density (up to $10^{15}/cm^2$) possibly leading to the discovery of novel electronic phases. Furthermore, electrolyte gating ideally suits possible flexible electronics developments. Fabricating electrolyte-gated transistors based on solution-processed nanostructured tungsten oxide thin films and shedding light on the transistor working principle will permit us to better assess their potential in the field of printable, flexible electronics and, considering the optical absorption properties of tungsten oxide, optoelectronics (e.g. phototransistors).

1.5 Objectives

The main objective of this thesis is to design, fabricate and characterize tungsten oxide transistors using the electrolyte gating approach, for flexible electronics applications.

Solution-processed tungsten oxide thin films with mesoporous nanostructure and high surface area are expected to have a peculiar doping mechanism, different from the mechanism proposed for its single crystal and nonporous film counterparts. Therefore, the first specific objective of this PhD thesis is:

1) Study the electrolyte gating process in transistors based on tungsten trioxide films with mesoporous nanostructure interfaced to ionic liquids to shed light on the doping mechanism.

The objective has been accomplished by extended cyclic voltammetry (CV), X-ray diffraction (XRD) and device characterization of EG transistors. The results enrich the current understanding of electron/ionic electroactivity at metal oxide/electrolyte interfaces.

Since the performance of transistors strongly depends on the morphology and structure of the channel materials, the second specific objective is:

2) Investigate the effect of the temperature of thermal treatment of the films and nature of the film substrate (conventional SiO_2 vs plastic) in establishing the transistor characteristics, to explore possible flexible developments of the devices.

The use of substrates different from conventional thermal silicon dioxide or glass, e.g. plastics, requires the use of low temperatures of thermal treatment. This temperature affects the morphology and structure of the channel, in turn affecting the doping process. Scanning Electron Microscopy, Atomic Force Microscopy, electrochemical and device characterization of novel electrolyte-gated transistors on polyimide were conducted.

Electrolyte-gated transistors based on photosensitive semiconductors can be interesting from the photodetection point of view because the high density of accumulated charge carriers can improve their photoresponsivity. The third specific objective is therefore the following:

3) Fabricate phototransistors in electrolyte gating configuration, exploiting the multifunctionality of metal oxides.

The combined electrical and photo response of tungsten oxide thin films in EGT configuration were investigated; the results permit to shed light on the working principle of electrolyte-gated phototransistors, in particular the photoresponsivity when the transistor is ON. In turn, the dual optical/electrical effect of such transparent transistors (90% transmittance at 600 nm of the semiconducting tungsten oxide films) can be relevant for numerous applications, such as touch screen, optical switch and photodetecting devices.

1.6 Organization of the work

An introduction to metal oxides and detailed physical and chemical properties of WO_3 are contained in Chapter 2. In this same chapter, we include a literature review about electrolyte-gated metal oxide transistors (channel materials, device structures, working mechanisms). Chapter 3 is the experimental part, where materials and techniques used in this thesis are described. Chapter 4, which addresses the first objective of this PhD thesis, is the reproduction of article "Electrolyte-Gated WO_3 Transistors: Electrochemistry, Structure, and Device Performance" published in the Journal of Physical Chemistry C. The electrochemical, structural, and device characteristics of EG transistors making use of mesoporous nanostructured WO_3 thin film channels and ionic liquids as the gating media were reported in this article. On the basis of the experimental results, several contributions were considered to explain the doping process. Chapter 5, corresponding to the second and third objectives, is the reproduction of article "Electrolyte-gated phototransistors based on tungsten oxide films" submitted to Advanced Materials Interfaces. This manuscript compares the performance of electrolyte-gated phototransistors that make use of tungsten oxide film channels on SiO_2 and on polyimide substrates, where the films have been treated at different thermal treatment temperatures. The study of the effect of the gate voltage on the sensitivity and photo responsivity gave insight into the working principle of electrolyte-gated phototransistors.

Chapter 6 is a general discussion on the results of this PhD thesis. Finally, conclusions are drawn and perspectives on future work are given in Chapter 7. Supplementary information for Chapters 4 and 5, a list of publications not included in the thesis and conferences attended during the PhD are included in the Appendix.

CHAPTER 2 LITERATURE REVIEW

This chapter starts with a brief introduction to metal oxide semiconductors (Section 2.1), followed by a description of the structural, electrical, optical and electrochemical properties of tungsten oxide (Section 2.2). Following this, electric double layer models and corresponding capacitance are reviewed (Section 2.3). Section 2.4 is an overview of the current knowledge about ionic liquid-gated transistors including channel materials, device structure and working mechanism.

2.1 Metal oxide semiconductors

Metal oxide semiconductors are investigated for transparent electronics and thin film transistors, due to their electrical properties and high reliability.[25] Electronic structure and charge transport mechanism in metal oxides are quite different from conventional covalent semiconductors like silicon. In silicon, anti-bonding (σ*) and bonding (σ) states of Si sp^3 hybridized orbitals form the conduction band minimum (CBM) and valence band maximum (VBM) (Figure 2-1a).[42] The charge carrier transport paths are built from these strongly directive sp^3 orbitals, and any structural random will degrade the magnitude of bond overlap (Figure 2-1b), that is charge carrier mobility.[24] For instance, intrinsic crystalline silicon (c-Si) exhibits an electron mobility of 1,500 $cm^2/V{\cdot}s$, whereas in hydrogenated amorphous silicon a-Si:H it is 2 $cm^2/V{\cdot}s$. In contrast, metal oxide semiconductors exhibit strong ionicity, the CBM is primarily formed by the unoccupied metal s orbitals (in post transition metal oxides) or the d orbitals (in transition metal oxides) and the VBM is formed by fully occupied O 2p orbitals (Figure 2-1a).[42] The large direct overlap of metal ns (n is the principal quantum number) orbitals is insensitive to distorted metal–oxygen–metal bonds (Figure 2-1b). Therefore, amorphous post transition metal oxides exhibit similar Hall-effect charge carrier mobilities respect to the corresponding crystalline phase states.[24] On the other hand, unfilled d orbitals in transition metal ions often form Fermi levels and alters the above discussion largely.[43]

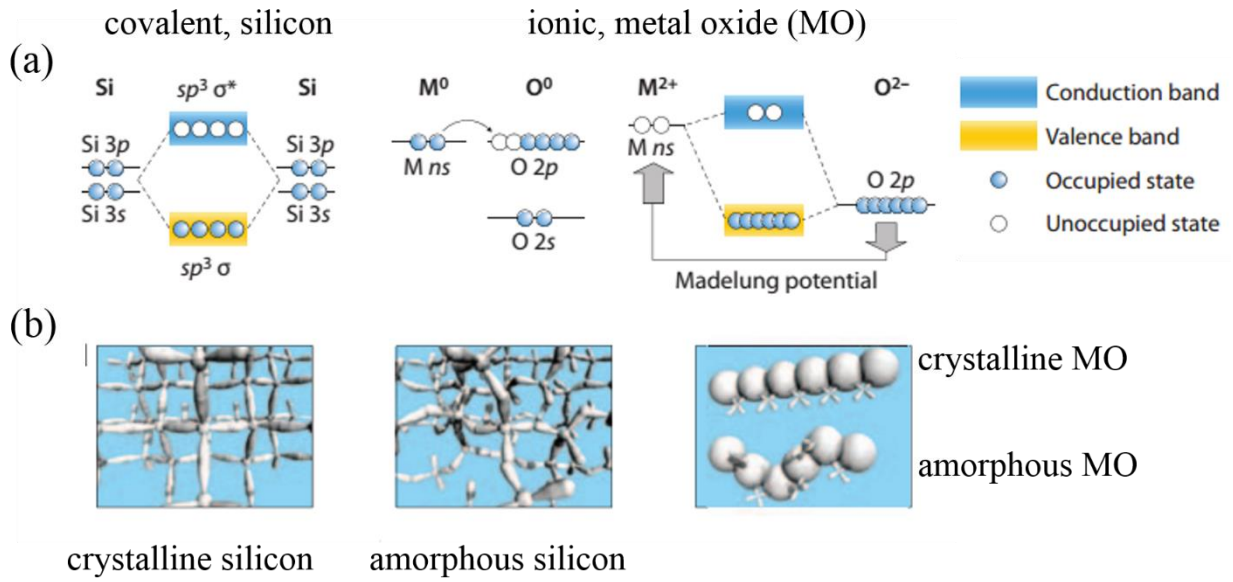

Figure 2-1 Schematic of (a) bandgap formation mechanism and (b) carrier transport paths for covalent (silicon) and ionic oxide semiconductors. (Reprinted with permission from Ref. 42, Copyright © 2010, Nature Publishing Group)

2.2 Tungsten oxide

2.2.1 Structural, electronic, optical and (electro)chemical properties of WO_3

Crystal Structures WO_3 exhibits a perovskite-like structure based on corner and edge sharing of WO_6 octahedra with O at the corner and W at the center of each octahedra.[44] WO_3 crystals go through structural transformations according to the sequence: tetragonal (> 740 °C) → orthorhombic (740 °C to 330 °C) →monoclinic (330 °C to 17 °C) →triclinic (17 °C to −43 °C) → monoclinic (< −43 °C) as the temperature changes (Figure 2-2).[44-47] Hexagonal WO_3 is particularly relevant to electrochromism (change in the optical absorption properties of a material as a function of the electrical bias applied). The electrochromism of WO_3, first reported in 1979, benefits from its open tunnel structure and intercalation chemistry.[48] In hexagonal WO_3, three- and six-membered rings are formed by WO_6 octahedra in the ab-plane and these octahedra are stacked by sharing the axial oxygen and form 4-coordinated square windows in the c-axis.[45] Amorphous WO_3 is built up of tightly bound $(WO_6)_n \cdot mH_2O$ clusters with a large number of W=O and W-O-W bonds between the clusters. The porous structure of amorphous WO_3 is enhanced by the corner or edge sharing octahedrons (3-8 membered rings network) forming clusters smaller than 20-30 Å.[49,

[50] Water molecules are easily filled in the open structure of amorphous WO_3 films due to the random packing of the clusters. Water molecule have strong effects on the physical properties of films and they can only partly removed by heating.[51]

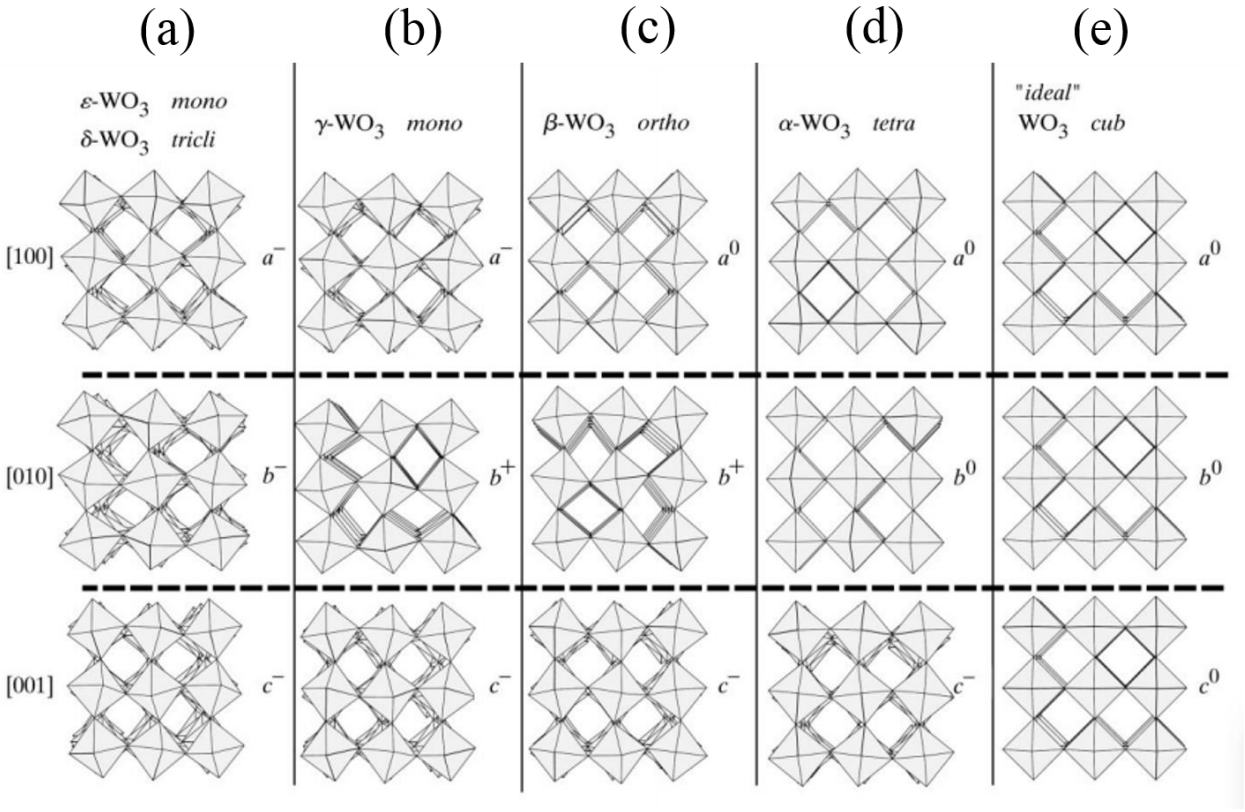

Figure 2-2 Structural models for tungsten oxide: (a) low temperature monoclinic, triclinic; (b) room temperature monoclinic; (c) orthorhombic; (d) tetragonal and (e) simple cubic. (Reprinted with permission from Ref. 52, Copyright 2000, International Union of Crystallography)

Electronic band structure WO_3 is an n-type semiconductor with bandgap E_g of about 2.6 -3.2 eV, function of the synthesis and processing conditions. Granqvist et al. calculated the density of states (DOS) for cubic WO_3 (Figure 2-3).[53] The results show that the O p states would form the valence band and W d states the conduction band; in addition, there would be considerable hybridization between the valence and the conduction bands. However, the value of E_g of 0.6 eV obtained from their calculations is quite different from the experimental results due to the fundamental limitations of local density approximation in semiconductor systems.[54] For instance, amorphous WO_3 with the

most distorted structure has E_g of ≈3.25 eV, whereas monoclinic WO_3, in bulk form, has E_g of ≈ 2.6 eV at room temperature.[55]

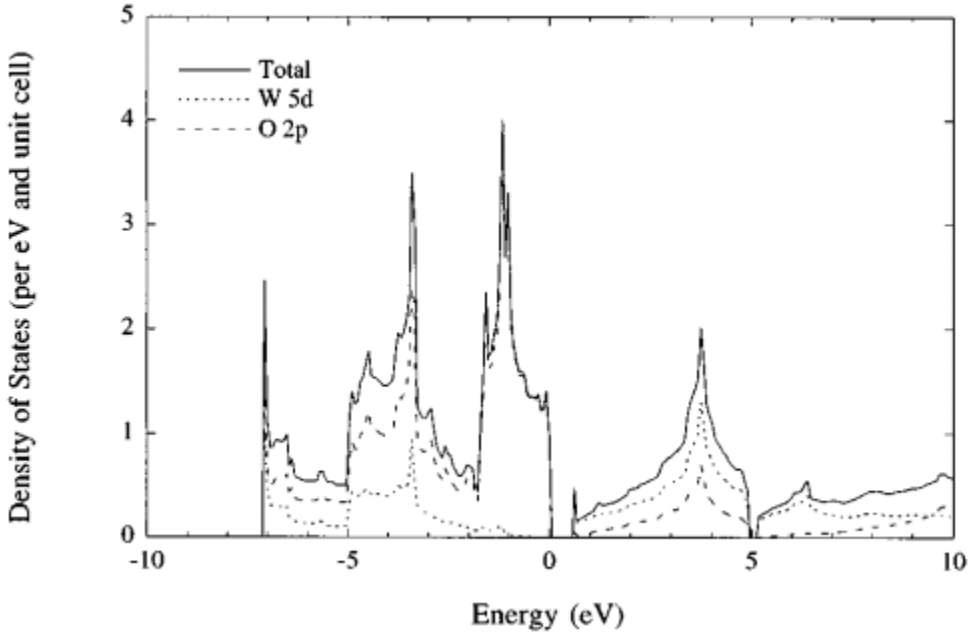

Figure 2-3 DOS of cubic WO_3. When energy is below 0 eV, filled states are found; empty states are found when energy is above 0 eV. (Reprinted with permission from Ref. 53, Copyright © 1996, American Physical Society)

Electrical conductivity (σ) For n-type metal oxide semiconductors, the electrical conductivity depends on the concentration of mobile electrons, which is mainly determined by the concentration of stoichiometric defects. Defects, such as oxygen vacancies, in the lattice of WO_3 are able to increase σ by many orders of magnitude.[56] Gillet et al. investigated WO_3 conductivity variations as a function of temperature with different pressures of oxygen. The results indicated that the surface oxygen vacancies introduce donor levels in the gap and mobile electrons are produced by thermal activation. In addition, dopants[57], microstructure characteristics (including grain size, nature of grain boundaries and specific crystalline phase) and film thickness also have a great influence on the conductivity. The electrical properties of WO_3 are strongly dependent on the synthesis technique and growth conditions. For example, Vemuri et al. reported the effect of structure and size of nanocrystalline WO_3 films on their electrical properties.[58] They found that the lower conductivity of WO_3 films treated at room temperature (RT) is due to their amorphous nature

and thus the conductivity increases with increasing substrate temperature because of the increasing crystalline nature and preferred orientation of the nanocrystalline WO_3 films along (00L).[58]

Optical properties The optical properties of WO_3 in the visible region are dominated by the absorption threshold. When the photon energy is smaller than E_g, i.e. for wavelength λ longer than hc/E_g, where h is the Planck constant and c is the speed of the light, the material does not absorb light. When the photon energy is equal to E_g, absorption from interband transitions will start to occur. For photon energies greater than the E_g, the light absorption coefficient α can be described:

$$\alpha h\nu \propto (h\nu - \mathrm{Eg})^{\eta}$$

Where ν (= c/λ) is the photon's frequency, hν is the photon's energy and η is an exponent. For WO_3, since the band gap is indirect (the crystal momentums of electrons and holes are not the same in the conduction band minimum and valence band maximum), the transitions are indirect and allowed, i.e. η = 2.[53] Typical transmission spectra of WO_3 are shown in Figure 2-4.

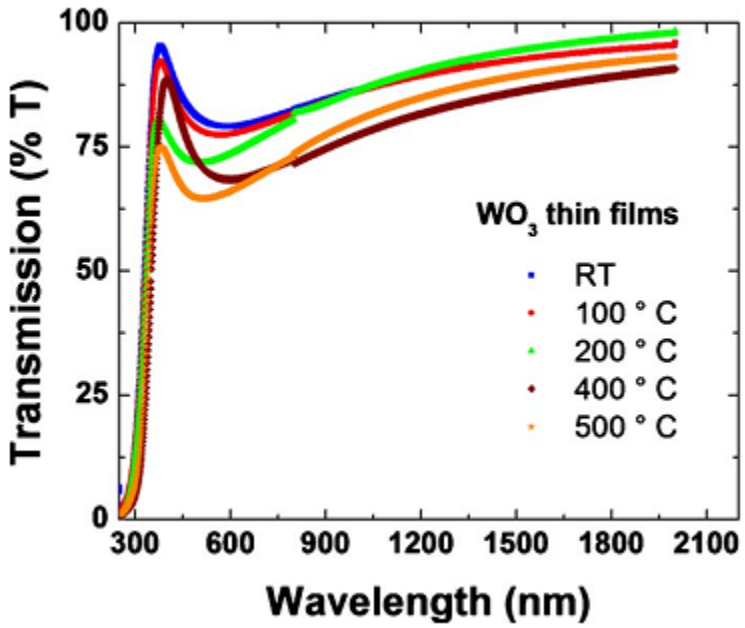

Figure 2-4 Transmission spectra of radio-frequency (RF) magnetron sputtered WO_3 films on optical grade quartz substrates with different substrate temperatures (Reprinted with permission from Ref. 59, Copyright 2010, AIP Publishing LLC)

Electrochemistry WO_3 is well known for its electrochromism.[60-63] The electrochromic process can be described by considering the injection of a quantity (x) of positive ions (M^+) and an equal quantity of electrons (e^-):

$$WO_3 + xM^+ + xe^- \leftrightarrow M_xWO_3$$

Typical M^+ ions can be H^+, Li^+ and Na^+. The quantity x can vary between 0 and 1. In an electrochromic thin film device, the ions are inserted from an ion-containing medium usually in liquid or solid form.[44, 64, 65]

Crandall et al. found that the diffusion coefficient of the electrons has values (D_{e-}) $2.5 \times 10^{-3} < D_{e-} < 7.5 \times 10^{-3}$ cm^2/s, rather insensitive to temperature changes.[66] On the other side, the values of the ion diffusion coefficient D_{M^+} cover the range $6 \times 10^{-20} < D_{e-} < 2.5 \times 10^{-7}$ cm^2/s and depend critically on the diffusing ionic species (H^+, Li^+, Na^+, etc), the nature of the film (crystallinity, porosity, hydration, etc.), the electrolyte and the temperature.[44] The great difference between De^- and D_{M+} results in a simple model for charge transport. Transfer of M^+ ions occurs at the electrolyte/oxide interface and electrons are then ejected by the electrode. "Inside the oxide film, the diffusion of M^+ ions manifests itself as even (or uneven) spreading of a plasma region from the electrolyte interface towards the electrode interface." In some other works, ion density was assumed uniformly changed over the film cross-section upon intercalation/deintercalation.[67, 68]

2.2.2 Nanostructured WO_3

Nanostructured WO_3 shows materials performance and properties that do not exist in bulk analogs. Briefly, comparing with the bulk materials, nanostructured WO_3 has 1) increased surface-to-volume ratio, i.e. nanostructured WO_3 provides more surface area for both chemical and physical interactions; 2) quantum confinement effects (when crystal size is smaller than ca. 3 nm) that influence electronic band structure, optical properties and charge transport; 3) altered surface energies, which allows us to tune and engineer the materials properties, due to the different bond structures near the surface from those in the bulk.[45]

Reviews on the fabrication and application of nanostructured WO_3 materials are reported in [45, 69].

2.3 Electrical double layer

Solid (electrode)-liquid (electrolyte) interfaces have attracted extensive interest due to the formation of an electrical double layer (EDL) in the presence of an electrical potential between them. As a result, various models have been proposed to describe the features of these interfaces.

Helmholtz Model Helmholtz proposed the first model of the EDL in 1853.[70] In this model (Figure 2-5a), an EDL can be treated as a simple planar capacitor at the atomic scale, i.e. charges on the electrode surface, on one plane of the capacitor, and immobilized counter ions of opposite sign at the electrode on the second plane. The potential drop across this layer is linear and very steep. The hypothesis of rigid layers of charges of opposite sign, which does not happen in reality, limits the applications of the model.

Gouy–Chapman Model Gouy and Chapman improved the Helmholtz model by introducing diffusion in the EDL.[71, 72] In this case, ions are mobile and distributed unequally at the interface, where they form a diffuse layer (Figure 2-5b). In the diffuse layer, ions with opposite polarity with respect to the electrode have a higher concentration compared to the bulk of the electrolyte. The electrical potential decreases exponentially with the distance from the interface toward the solution.

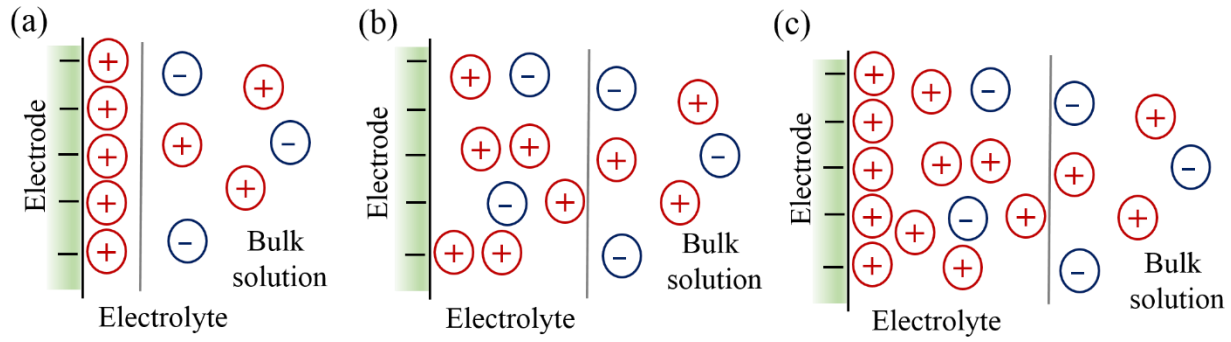

Figure 2-5 Scheme of the (a) Helmholtz, (b) Gouy-Chapman and (c) Gouy-Chapman-Stern Models for the electrical double layer at an electrolyte/electrode interface.

Gouy-Chapman-Stern Model In 1924, Stern suggested a new model that combines the Helmholtz model with the Gouy-Chapman model, i.e. Gouy-Chapman-Stern Model.[73] In this model, the

electrolyte is divided into two different layers: the internal layer is the Helmholtz layer (Stern layer) and the outer layer is the Gouy-Chapman diffuse layer (Figure 2-5c).

These models are established for describing the double layers based on dilute electrolyte solutions, in which solute ions are well-separated and have no interactions.[74] Unfortunately this model does not work for EDL based on ionic liquids.

2.3.1 Ionic liquid based EDL

When ionic liquids (liquid salts with ionic, solvent-free features at temperatures below 100 °C, typically formed from organic cations and inorganic anions) interface with a polarized electrode, classical EDL models cannot be used. As discussed by Li[75], this is because: (i) Debye lengths (i.e. the characteristic shielding distance of a charge carrier's net electrostatic effect in solution) are smaller than the ion-pair dimensions due to the very high ionic strength (i.e. a measure of the concentration of ions in the solution); (ii) large ions cannot be modeled as point charges; (iii) ionic liquids frequently have self-assembled structures in the bulk and at interfaces; and (iv) the ion concentration of charged species at the interface does not differ significantly from the bulk. A multilayer model (Figure 2-6a), established for molten salts, gives a better agreement with the experimental results obtained with double layers observed with ionic liquids.[76]

From 2009, Atkin et al. started to study the structure of Au (111)/ionic liquid interfaces by AFM.[77-79] They measured the cohesion force of the different layers of ions adsorbed near the surface, which can be displayed in the form of a solvation force profile, by using the AFM tip to poke through the layers. The results reveal that multiple ion pair layers are observed extending from the Au (111) surface, the number of observable layers increases with the applied potential due to a templating effect at the interface, the strength of the interaction between the innermost layer and the substrate is dependent on the cation. Other techniques including cyclic voltammetry, scanning tunneling microscopy (STM) and X-ray interface scattering were also used to investigate the solid-ionic liquid interface.[77, 80]

In an electrode/ionic liquid/semiconductor configuration, electrical double layers are formed at the liquid–solid interfaces upon application of a voltage. The potential drops are confined within ultrathin regions regardless of the thickness of the electrolyte (Figure 2-6b) and this allows a high charge carrier density accumulation.

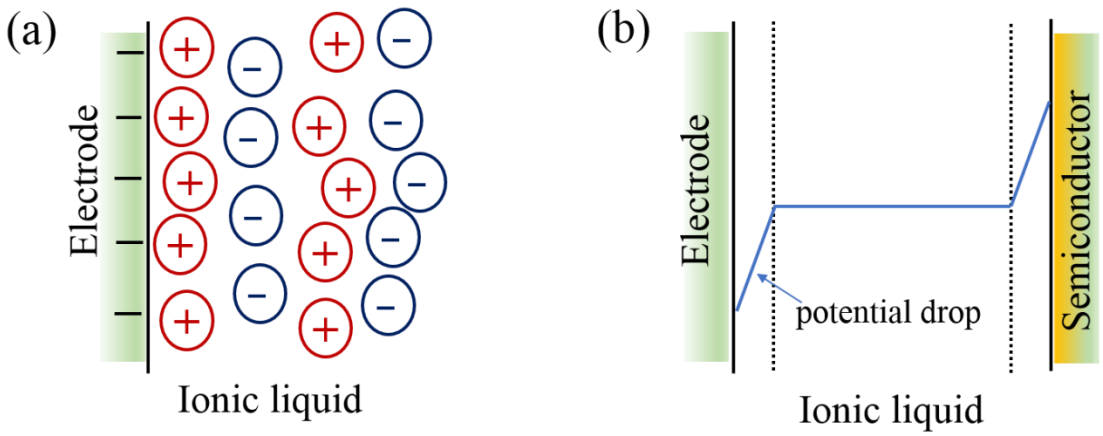

Figure 2-6 (a) Scheme of the multilayer model for electrical double layers at ionic liquid/ electrode interface. (b) Potential changes in an electrode/ionic liquid/semiconductor configuration.

2.3.2 Capacitance of solid-ionic liquid interfaces

To evaluate the performance of devices based on electrical double layers, the capacitance of solid-ionic liquid interfaces has been studies by many researchers. Thiemann et al. examined the specific capacitance of Pt-ionic liquid interfaces of eight ionic liquids, [EMIM][TFSI], [EMIM][TCB], [EMIM][FAP], [BMIM][TFSI], [BMIM][FAP], [HMIM][FAP], [EMMIM][TFSI] and [BMMIM][TFSI] by different techniques and theoretical models (Table 2-1).[81] The results of their studies show that Pt-[EMIM][TCB] and Pt-[EMIM][TFSI] interfaces exhibit the highest capacitances and Pt-[HMIM][FAP] the lowest capacitance. This is because smaller and less sterically demanding ions form more densely packed EDL leading to higher capacitances.[82]

Table 2-1 Specific capacitance calculated from different theoretical models for Pt-ionic liquid interfaces. Cap[d] indicates the capacitance obtained by fitting their EIS data to the RC-RC-model (the electrical double layer at the Pt-ionic liquid interface is considered as a capacitor with a resistive component, in parallel whereas the bulk ionic liquid is considered as a resistor with a capacitive component, in parallel). Cap[e] is the capacitance calculated from impedance analysis according to Z´´= -1/C2πfA, where f is the frequency of the ac perturbation, A is the electrode area. Maximum capacitance, Cap[f], is measured with LCR meter using the Cp-mode (resistor and capacitor in parallel) on a Pt/IL/Pt configuration at 20 Hz, dc bias 0 V. (Adapted with permission from Ref. 81, Copyright (2012) American Chemical Society).

cation	anion	cap^d [μF·cm^{-2}]	cap^e [μF·cm^{-2}]	cap^f [μF·cm^{-2}]
[EMIM]	[FAP]	5.5	2.4	3.4
[BMIM]	[FAP]	2.0	1.3	3.2
[HMIM]	[FAP]	3.9	3.3	2.4
[EMIM]	[TFSI]	7.8	3.8	7.0
[BMIM]	[TFSI]	3.9	3.3	5.9
[EMIM]	[TCB]	5.2	8.4	8.7
[EMMIM]	[TFSI]	3.9	3.5	4.7
[BMMIM]	[TFSI]	3.7	3.1	4.0

Fujimoto et al. studied the frequency dependence of the capacitance for six ionic liquids, [DEME][TFSI], [DEME][BF4], [BMIM][TFSI], [BMIM][BF4], [BMIM][OTf] and [BMIM][PF6], in an electrochemical cell based on octathio[8]circulene on SiO_2/Si substrate with digitated array electrodes (Pt) as the working electrode, platinum wire as the counter electrode, Ag/AgCl as the reference electrode, and the ionic liquid as the electrolyte, in the range from 10^{-1} to 10^5 Hz.[83] The EDL capacitance values for all the ionic liquids are on the order of 10^{-6} F/cm^2 at frequency below 10^2 Hz and show fast decreases above 10^2 Hz. Their results also showed that the capacitance values are dependent on the ionic liquid at low frequency and independent at high frequency (Table 2-2).

Table 2-2 Capacitance of EDL at 0.1 Hz for the Octathio[8]circulene electrical double layer organic transistors. (Adapted with permission from Ref. [83]. Copyright (2012) American Chemical Society).

ionic liquid	cation	anion	C_{IL} at 0.1 Hz
1	DEME	TFSI	2.7×10^{-6}
2	DEME	BF_4	4.6×10^{-6}
3	BMIM	TFSI	3.1×10^{-6}
4	BMIM	BF_4	2.0×10^{-6}
5	BMIM	TFS	3.9×10^{-6}
6	BMIM	PF_6	2.5×10^{-6}

Ono et al. also reported on the dependence of the capacitances on the frequency for [EMIM][FSI], [EMIM][TFSI], [EMIM][BETI], [EMIM][BF4] and [EMIM][DCA] over the range from 10^{-1} Hz to 10^6 Hz.[84] For all the ionic liquids, the values of the capacitance increase with decreasing frequency in the range of 10 – 10^3 Hz. Due to the variation of the anions, the capacitance differs by two orders of magnitude and [EMIM][DCA] provided the largest value of 170 μF/cm^2 at 0.1 Hz.

2.4 Ionic liquid-gated transistors

When a voltage is applied between two electrodes in an electrochemical cell, ions in the electrolyte migrate towards the two sides according to their polarity. An electric double layer, which works as a nanometer-gap capacitor with the electrolyte as the dielectric layer, formed due to the accumulation of ions on the electrode surface. On the electrode side, an equal amount of charge with opposite polarity accumulates. If one of the electrodes is replaced by a semiconductor with source and drain electrodes, the system works as a FET.[85] This device is commonly referred to as an electric double layer transistor or electrolyte-gated transistor, i.e. an electric field applied across the semiconductor/electrolyte interface can either accumulate or deplete charge carriers, controlling the conductivity of the semiconducting channel.

Although rather neglected in the beginning, in the last decade, EGT, utilizing electrolytes as gating material in FET, are receiving renewed attention due to their significant low driving voltages (sub

2 V) and high accumulation of charge carrier density (up to 10^{15} cm^{-2}). The high capacitance, C (~1–10 μF/cm^2, about 10–1000 times higher than that of conventional dielectrics) at the electrolyte/semiconductor transistor channel interface is the underpinning of such low operation voltages and high charge carrier density according to the standard equation for the transistor drain current in the linear regime ($V_{ds} << V_{gs}$), $I_{ds} = (W/L)\ \mu C_0\ (V_{gs} - V_{th})\ V_{ds}$. For a certain μ, the same I_{ds} can be obtained at smaller V_{gs} with larger C_0.[36] In turn, the high capacitance is due to the formation of thin (2-4 nm thick) electrical double layers at the electrolyte/ channel interface. The ability to control surface carrier densities at levels up to 10^{15} cm^{-2} has led to widespread use in the study of superconductivity, insulator–metal transitions, etc. [86-88]

It is worth noting that, in fact, the total capacitance of the electrolyte layer is determined by the capacitance of the two EDL connected in series, i.e. EDL at gate electrode/electrolyte and electrolyte/semiconductor interfaces. However, the total capacitance will never be larger than the smaller of the two EDL capacitors, which usually is the EDL at the electrolyte-semiconductor interface.[36]

Electrolytic solutions, polymer electrolytes, polyelectrolyte, ionic liquids, ion gels and even water were extensively reported as gating media.[89-94] Among these, ionic liquids have attracted much attention due to their tunable physical and chemical properties, wide electrochemical stability windows, low vapour pressure and high ionic conductivities.[95, 96]

The first ionic liquid-gated transistor was reported by Hebard et al. in 2007. They used amorphous InO_x as channel material and EMI-Beti as gating medium.[97] Specific capacitance of 5.9 μF/cm^2 and field effect mobility of 37.3 $cm^2V^{-1}s^{-1}$, ca. 10 times higher than that of transistors using AlO_x dielectrics, were obtained. Later, in 2008, Ono et al. reported the first ionic liquid-gated transistors based on organic semiconductors, i.e. a rubrene single-crystal.[98] The device operated at a voltage as low as 0.2 V, displayed a specific capacitance of 11 μF/cm^2 and a field-effect mobility of 1.2 $cm^2V^{-1}s^{-1}$.

2.4.1 Channel materials

Ionic liquid-gating has been applied to various inorganic and organic semiconductors.[84, 99-101] In this section, we review ionic liquid-gated transistors of materials based on organic materials, metal oxides and metal sulfides.

Organic channel materials Due to their flexibility, low-cost fabrication and easy chemical modification of organic semiconductors, organic field-effect transistors (OFET) technology experienced rapid development in the past decades. After the first ionic liquid-gated rubrene transistor produced in 2008, high performance ionic liquid-gated organic transistors have been widely reported.

Frisbie and coworkers studied electrolyte-gated rubrene, pentacene and P3HT organic transistors. In 2011, they reported single crystal rubrene-based electrolyte-gated transistors with five ionic liquids as gating media.[102] The authors fabricated bottom-gate, bottom-contact organic EGT (OEGT) with the ionic liquids [P13][TFSI], [EMI][TFSI], [EMI][FAP], [P14][TFSI] and [P14][FAP] (Figure 2-7). A maximum carrier mobility of 3.2 $cm^2 V^{-1}s^{-1}$ was obtained by gating with [P14][FAP] at room temperature. The temperature dependence of the mobility indicates a thermally activated behavior with an activation energy of 30 meV, i.e. charge transport is dominated by shallow traps. A charge concentration of 6.3×10^{13} cm^{-2} was achieved at the freezing point of the ionic liquid (~210 K), with a gate bias of -3.5 V.

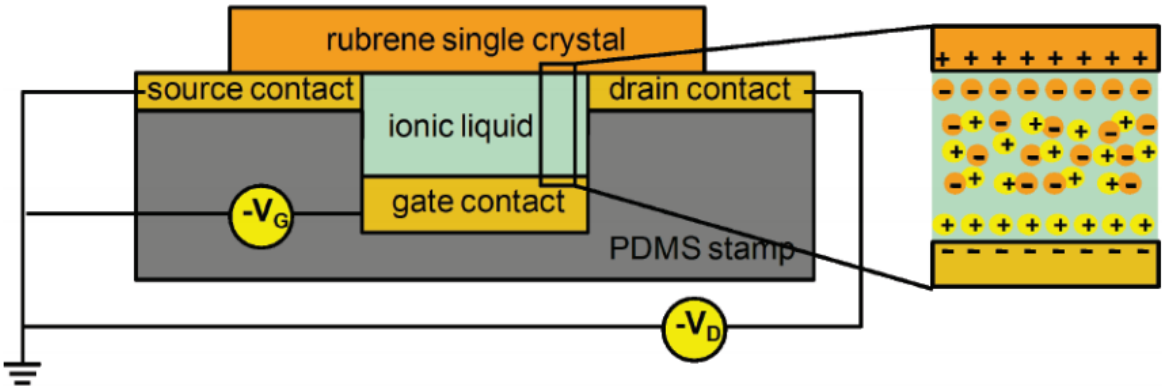

Figure 2-7 Cross section of a rubrene ionic liquid-gated transistor. (Reprinted with permission from Ref. 102, Copyright (2011) American Chemical Society).

Frisbie et al. also worked on ionic liquid-gated transistors of pentacene single-crystals.[103] These devices exhibited a field effect mobility of 0.02 $cm^2V^{-1}s^{-1}$ at room temperature. Higher mobility of 5 $cm^2V^{-1}s^{-1}$ was achieved by Matsumoto in 2012 with molecular scale step-and-terrace structure obtained by ionic liquid-assisted vacuum deposition, in bottom gate, bottom contact transistor configuration.[104]

Ionic liquid-gated transistors of polymers, e.g. P3HT, PQT-12 and MEH-PPV have been widely studied recently. In 2007, Frisbie et al. produced a [BMIM][PF6]-based ion gel-gated P3HT transistor with a hole mobility of 0.6 $cm^2V^{-1}s^{-1}$ and an ON/OFF ratio of 10^5.[93] The transistor possesses a gate capacitance of 40 μF/cm^2 and a response time of 1ms at 10 Hz. Later, in the same device configuration, [EMIM][TFSI], [EMIM][PF6] and [EMIM][OctOSO3]-based ion gels were used as the gate dielectrics to compare the device performance.[105] The average mobility was 1 $cm^2V^{-1}s^{-1}$ for the three ion gel-gated transistors whereas the ON/OFF ratios were ca. 10^5 for the cases of [EMIM][TFSI] and [BMIM][PF6] and ca. 10^4 for [EMIM][OctOSO3]. In particular, EGT making use of the [EMIM][TFSI]-based gel can operate at 1 kHz due to the high ionic conductivity of the gel. Frisbie's group also reported on [EMIM][FAP]-gated P3DTV, P3HT, MEH-PPV and F8BT transistors with mobility of 0.27, 0.86, 0.08 and 0.07 $cm^2V^{-1}s^{-1}$.[106]

Santato et al. also reported a MEH-PPV thin-film EGT with [EMIM][TFSI], [BMIM][TFSI], and [PYR14][TFSI] as gate dielectrics.[107] These transistors had top-gate, bottom-contact structure with a special gate electrode made of activated carbon on carbon paper. This activated carbon paper was put on the ionic liquid to serve as the gate electrode. Hole mobility of 2.5×10^{-2}, 1.5×10^{-2} and 2.0×10^{-2} $cm^2V^{-1}s^{-1}$ were obtained for [EMIM][TFSI]-, [BMIM][TFSI]-, and [PYR14][TFSI]-gated MEH-PPV transistors.

In addition to the above mentioned p-type and polymer organic materials, n-type and ambipolar organic materials were investigated as EGT channel materials as well.[108-110] Carbon nanotubes, graphene and perovskite have also been extensively studied as channel materials in EGT.[111-113]

Inorganic channel materials This section mainly introduces metal oxide semiconductors.

Yuan et al. reported a [DEME][TFSI]–gated ZnO transistor in top-gate, top-contact configuration in 2009 (Figure 2-8a).[92] A sheet charge carrier density of 4.5×10^{14} cm^{-2} and Hall mobility of 100 $cm^2V^{-1}s^{-1}$ was obtained at 300 K, V_{gs} = 2.5 V (Figure 2-8b). The excellent reproducibility of the current response to the repeatedly pulsed V_g excluded chemical doping or chemical reactions at the ionic liquid/ZnO interface. The weak dependence of the channel resistance on the temperature at V_g values above 1 V indicated an insulator–metal transition by electrostatic doping. At low temperatures, owing to the decreased electrochemical activity of the ionic liquids, V_{gs} as high as 5.5 V was applied without device degradation and dielectric breakdown. High charge carrier densities of 8.0×10^{14} cm^{-2} at 220 K and 5.5×10^{14} cm^{-2} at 1.8 K were achieved. Afterwards, with the

same device structure but using protic ionic liquid including a small amount of water, the authors found some new properties of protic ionic liquid EGT. Inner Helmholtz layers can be formed to increase the EDL capacitance and accumulate charged carriers. By controlling the chemisorption or physisorption of H^+ and OH^- on polar ZnO surfaces, surface polarity and surface atom recognition can be controlled. Surface hydrogenation can lead to proton memory behavior.[114]

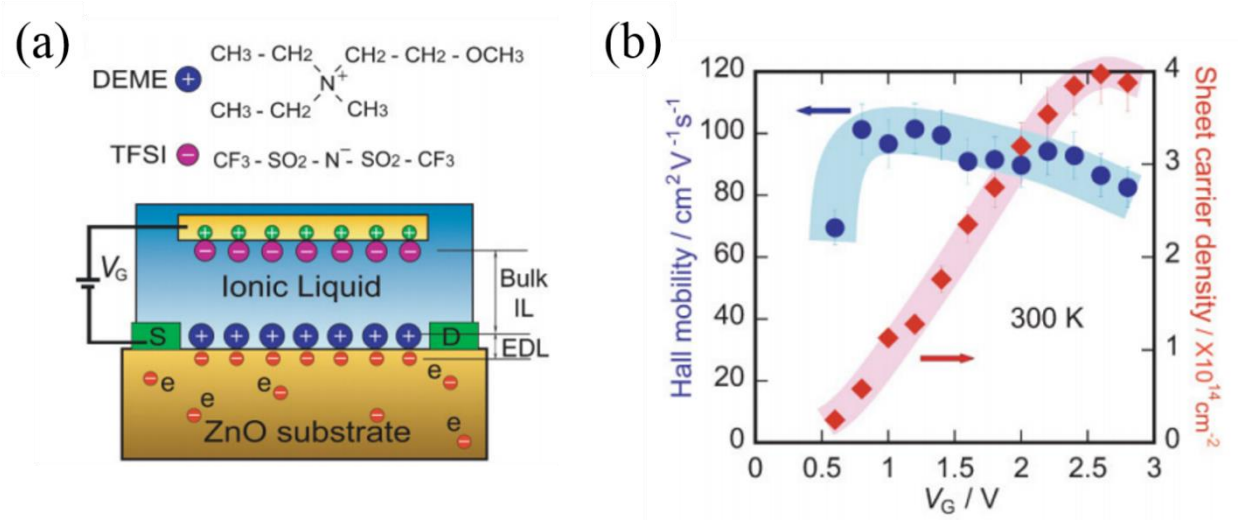

Figure 2-8 (a) Molecular structures of the ionic liquid, [DEME][TFSI] (top) and the cross-section of ionic liquid-gated ZnO transistors (bottom). (b) Sheet carrier density and Hall mobility as a function of gate voltage at 300 K, determined by Hall effect measurements. (Reprinted with permission from Ref. 92. Copyright 2009 WILEY-VCH Verlag GmbH & Co. KGaA, Weinheim)

Zaumseil et al.[81] investigated the influence of the chemical structure of the ionic liquid on the device performance of EGT based on spray-deposited polycrystalline ZnO. They found that the device is stable in nitrogen atmosphere and degrades rapidly in ambient air due to absorption of water by the ionic liquid and the resulting surface reactions of the ZnO. Finally, they improved the device environmental stability by replacing the most acidic hydrogen atom of the imidazolium cation with a methyl group and passivating the surface of ZnO with hexamethyldisilazane (HMDS).

In 2013, Zaumseil et al.[115] fabricated [EMIM][TFSI]-gated solution-processable colloidal ZnO nanorod transistors in top-gate, top-contact configuration. Nanorods with different degrees of alignment and aspect ratios were obtained by using the self-assembly properties of the colloidal dispersions at the liquid−solid−air interface. Electron mobilities depend strongly on the degree of

alignment but less on the length of the nanorods; a maximum linear mobility (9 $cm^2 V^{-1} s^{-1}$) was obtained for well-aligned ZnO nanorods. Their ZnO nanorod thin films are suitable for application on flexible polymer substrates due to the low processing temperature (150°C).

Recently, Frisbie et al.[116] reported on 2D insulator–metal transition in solution processed In_2O_3 thin film transistors gated with [EMI][TFSI]-based ion gel. They fabricated the transistor in van der Pauw geometry to allow both transistor and Hall Effect measurements (Figure 2-9a). Similar values of the electron density were extracted from Hall effect (n_{Hall}) and displacement current (n_{FET}) (Figure 2-9b). n_{Hall} of 5.6 $\times 10^{14} cm^{-2}$ (comparable with metal oxide EGT based on vacuum-deposited single crystal or epitaxial films) and μ_{Hall} of 11 $cm^2 V^{-1} s^{-1}$ (Figure 2-9c) were achieved. At high electron density (larger than 2.06 $\times 10^{14}$ cm^{-2}), they observed an insulator to 2D metal transition.

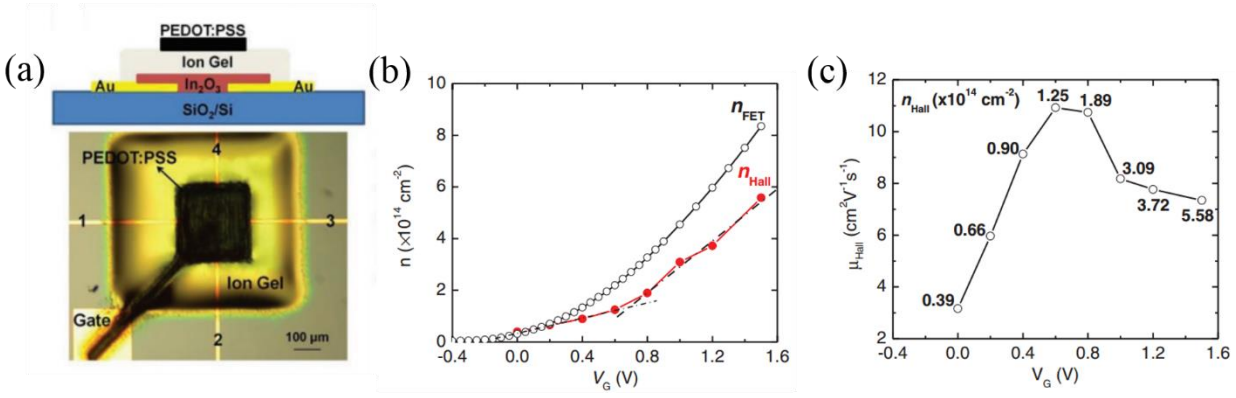

Figure 2-9 (a) Schematic and optical image of an ion-gel-([EMI][TFSI]+PS-PMMA-PS)-gated solution processed In_2O_3 transistor. (b) Electron density from Hall effect (n_{Hall}), and from displacement current (n_{FET}) versus V_g. (c) Hall mobility (μ_{Hall}) versus V_g; n_{Hall} is labeled in correspondence of each point. (Reprinted with permission from Ref. 116, Copyright 2017 WILEY-VCH Verlag GmbH & Co. KGaA, Weinheim.)

ZnO and In_2O_3 are post-transition metal oxides, where the conduction band is formed by metal s orbitals. Some transition metal oxides (d group metals) have been also studied in EGT due to the metal-insulator transition, high-temperature superconductivity and colossal magnetoresistance properties.[117]

Tokura et al. reported on an EGT making use of pulsed laser deposited VO_2 as the transistor channel and [DEME][TFSI] as the gating medium.[118] They examined the V_g effect on the metal–insulator

transition temperature (T_{MI}) (Figure 2-10a): for $V_g < 0.3$ V, T_{MI} remains unchanged, indicating that electric field effect is limited to the top most surface of VO_2 by the Thomas–Fermi screening effect as in conventional FET. For 0.3 V < V_g < 0.7 V, T_{MI} decreased with V_G, indicating the presence of a metallic state in the bulk region. For $V_g > 0.7$ V, the vanished T_{MI} implies the emergence of a metallic ground state. The V_g values where the metallic ground state arises are independent of the film thickness. Indeed, the accumulated surface charge can trigger the delocalization of previously localized electrons in the bulk VO_2 film, leading to a three-dimensional metallic ground state with charge carrier density >10^{22} cm^{-3} due to strong electron correlations (Figure 2-10b).

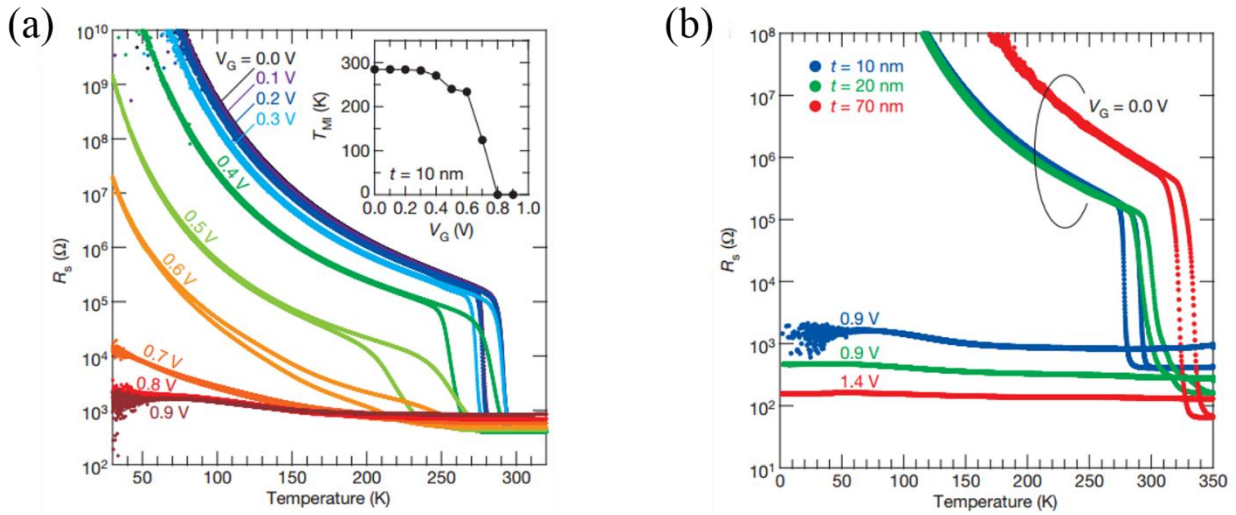

Figure 2-10 (a) Temperature dependence of the sheet resistance (R_s) for VO_2 film with different gate voltages (V_g). (b) Temperature dependence of R_s for VO_2 film with different thickness, 10-, 20- and 70-nm, showing both initial (V_g = 0 V) and electric-field-induced metallic states. (Reprinted with permission from Ref. 118, Copyright 2012 Nature Publishing Group.)

Superconductivity has been attracting much attention for its potential application in medical equipment, high-speed processing electronics and new transport systems.[119, 120] Electrolyte gating offers a new strategy to achieve superconductivity without inducing structural disorder, which is a drawback for the most commonly used strategies, i.e. substitutional or interstitial chemical doping. After the first report on the insulator-to-superconductor transition in $SrTiO_3$ by the EDLFET strategy with polymer electrolyte gate dielectrics, several works based on ternary metal oxides have been published.[86] For example, Goldman et al. reported an insulator-to-superconductor transition in $SrTiO_3$ single crystals, using ionic liquid EGT.[121] They fabricated top-gate, top-contact

transistors with [DMIM][TFSI]. The onset of the superconducting transition was observed at about 0.4 K, with charge carrier density of 9×10^{14} cm^{-2}. During the measurements, they observed an anomalous Hall effect, suggesting magnetic ordering. Electric field-induced superconductivity for other materials were also reported. In 2010, Iwasa et al. reported an EGT-induced superconductivity on an atomically flat film of layered nitride compound, ZrNCl, with [DMIM][TFSI] (Figure 2-11).[122] The charge carrier density, determined by Hall measurement, increased from 0.3×10^{14} to 2.5×10^{14} cm^{-2} with increasing V_g from 0 V to 4.5 V and Hall mobility was 50 $cm^2V^{-1}s^{-1}$.

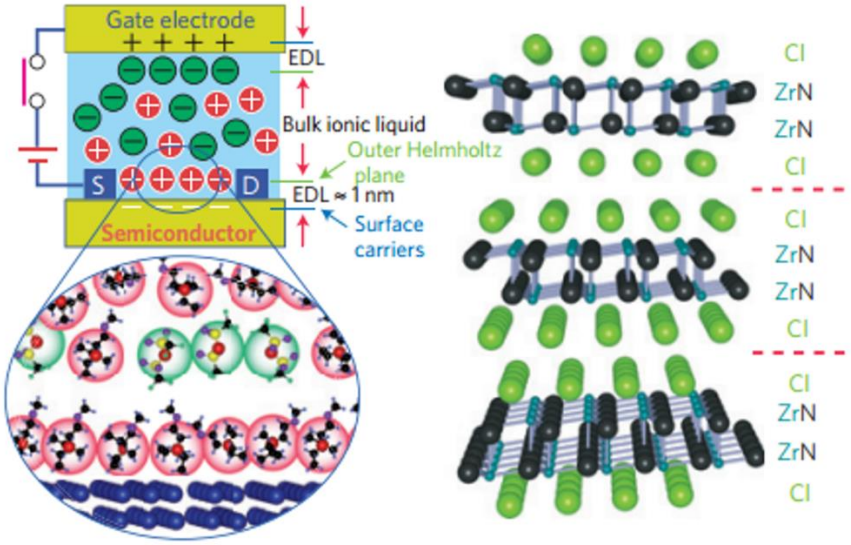

Figure 2-11 (a) Schematic of charge accumulation by an electric double layer formed at an interface between [DMIM][TFSI] and ZrNCl. (Reprinted with permission from Ref. 122, Copyright 2009 Nature Publishing Group.)

In summary, recent progress in ionic liquid-gated transistors has been remarkable. This method has been applied to various materials, organic materials, inorganic materials, carbon nanotube and graphene. Among inorganic materials, metal oxides stand out for anomalous field-induced effects. Such as insulator-to-metal transition, insulator-to-superconductor transition, or ferromagnetic transition. The device performance of ionic liquid-gated metal oxide transistors is strongly dependent on the physicochemical properties of the ionic liquids utilized, the quality of the metal oxide films (morphology, crystal structure) and the gate voltage applied. Although several works from Zaumseil[115] and Frisbie[116] showed comparable device performance of vacuum and solution

processed ZnO and In_2O_3 transistors, other solution processable metal oxides, such as WO_3, have not been systematically investigated.

2.4.2 Device architecture

Transistor performance significantly depends on the device configuration. Yang et al. studied ionic liquid-gated VO_2 transistors in vertical and planar gate geometry with [DMIM][TFSI] and [EMIM][Im] (Figure 2-12a).[123] At 25 °C, device performance for different geometries are shown in Figure 2-12b. A device with planar gate geometry (device A) showed better channel resistance modulation than one with vertical gate geometry (device D). The VO_2 channel resistance of device A decreased from 109 to 63 kΩ when V_g increased from 0 V to 2 V. Under the same V_g change, the metal-insulator transition temperature decreased about 0.5 °C (from 71.88 °C to 71.35 °C) because of the charge carrier density changes. No gate effect is observed due to the metallic state of VO_2 at high temperature.

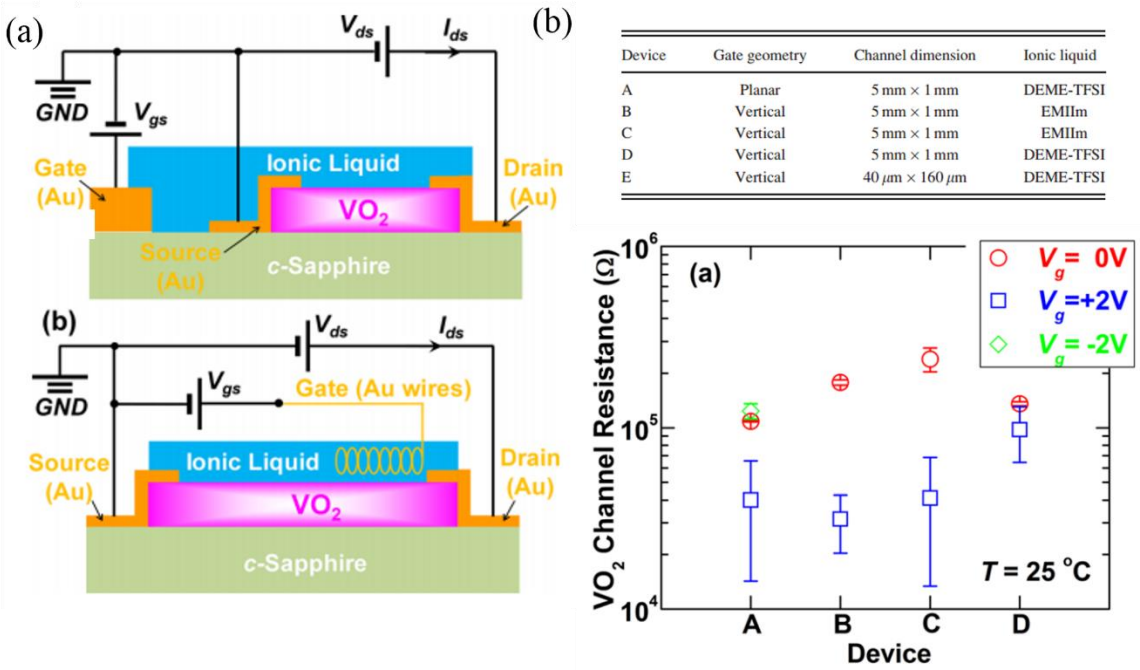

Device	Gate geometry	Channel dimension	Ionic liquid
A	Planar	5 mm × 1 mm	DEME-TFSI
B	Vertical	5 mm × 1 mm	EMIIm
C	Vertical	5 mm × 1 mm	EMIIm
D	Vertical	5 mm × 1 mm	DEME-TFSI
E	Vertical	40 μm × 160 μm	DEME-TFSI

Figure 2-12 (a) Schematics of the VO_2 EGT devices with planar (top) and vertical (bottom) gate geometry. (b) Parameters (top) (gate geometry, channel dimension, and the ionic liquid material) for different VO_2 EGT devices and their performance (bottom) at 25 °C. (Reprinted with permission from Ref. 123, Copyright 2012 AIP Publishing LLC.)

In summary, electrolyte-gating offers the opportunity to fabricate new device architectures, i.e. coplanar source-drain and gate geometry due to high capacitance at the electrolyte/channel material interface. By comparing devices with co-planar and vertical gate geometries, the former shows promise for in situ characterization and the latter usually has a faster device response time.

2.4.3 Working mechanism of ionic liquid-gated metal oxide transistors

The doping mechanism in ionic liquid-gated metal oxides transistors is a matter of debate. In section 2.4.1, we discussed electrolyte-gated transistors based on electrostatic doping upon application of a gate voltage. However, if V_g becomes sufficiently large or if the semiconductor is ion-permeable, an electrochemical process (reaction) is possible. Yuan et al. investigated the doping mechanisms in [DMIM][TFSI]-gated ZnO transistors as a function of gate voltage by combining charge transport measurements with electrochemical impedance spectroscopy (EIS).[124] First, they performed EIS measurements on a Pt/ionic liquid/Pt capacitor structure, which serves as an ideal EDL capacitor with minimal interfacial chemical processes. From 10 mHz to 1 MHz, two domains (the EDL capacitor and the bulk ionic liquid capacitor) can be observed in the angle-frequency, θ-f plot (Figure 2-13a). EIS measurement on Pt/ionic liquid/ZnO structure showed one more frequency domain below 1 Hz, due to the pseudocapacitance, i.e. electrochemical processes occurring at the IL/ZnO EDL interface (Figure 2-13b). The strong V_g dependence behavior of the capacitance indicated the contribution of pseudocapacitance at low frequency (0.1 Hz). The authors compared the amount of mobile charge carriers from the Hall effect with the total amount of accumulated charges from the capacitance-voltage integration at different frequencies (Figure 2-13c). At 1 Hz, the charges obtained from the two methods are similar (5.4×10^{14} cm^{-2} at V_g=3 V) whereas at 0.1 Hz, the charge from the Hall effect is much smaller than that from the capacitance-voltage integration method (19×10^{14} cm^{-2} at V_g = 3 V). The variation in the charge values deduced at 0.1 and 1 Hz indicated that the Faradaic charges have no contribution to charge carrier transport in the channel. Finally, the phase diagram (temperature-frequency mapping of EIS, Figure 2-13d) to distinguish the electrostatic or electrochemical nature of the doping suggested that high frequency or low temperature can confine the device operation in electrostatic region.

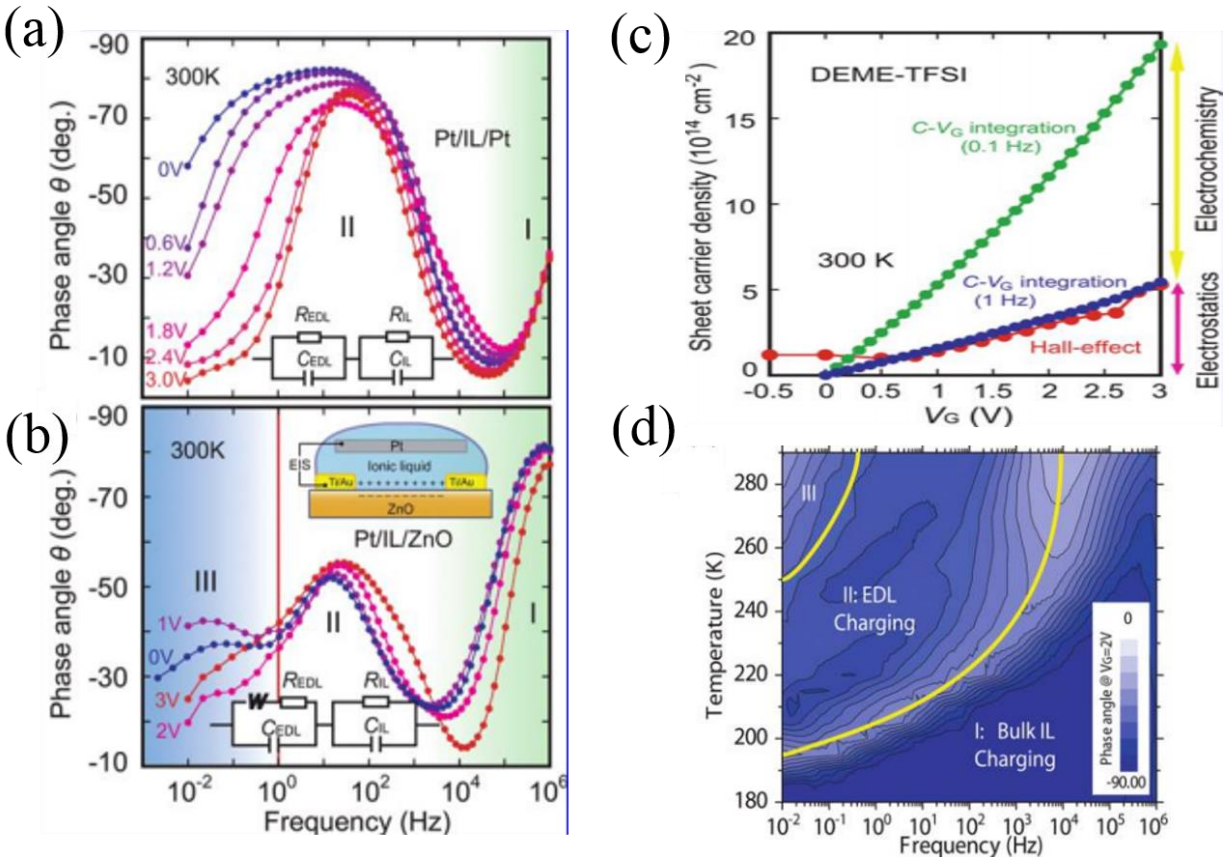

Figure 2-13 The θ-f plots in (a) Pt/ionic liquid/Pt and (b) Pt/ionic liquid/ZnO structures at varied biases. Inset: equivalent electric circuit and cross section of positively biased ZnO electrical double layer transistor. (c) Charge carrier densities as a function of V_g from Hall measurement (red dots) and from the C-V_g integration (blue dots for 1 Hz and green dots for 0.1 Hz). (d) Temperature-frequency mapping for the phase angle of the Bode plot. (Reprinted with permission from Ref. 124, Copyright (2010) American Chemical Society.)

Leng et al. investigated the doping mechanisms in [DMIM][TFSI]-gated transistors making use of RF magnetron sputtered ITO and WO_3.[125] Films were patterned on a substrate with several contacts and only one was covered with electrolyte (Figure 2-14). Long-range (2 mm) effects in oxide thin films away from the area being charged can be measured in this configuration. The results for ITO EGT were fast, reversible and showed no hysteretic charging/discharging processes and no diffusion of ions into the channel (pure electrostatic doping mechanism). WO_3 EGT, in contrast to ITO, shows a slow charging/discharging process with hysteresis and migration of ion from contact 1 to other contacts.

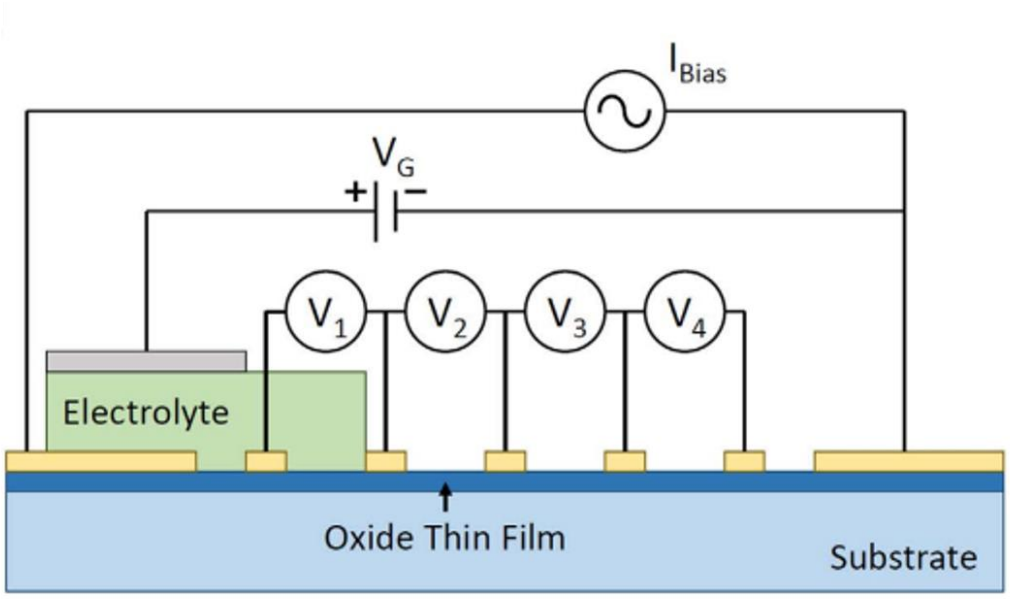

Figure 2-14 Scheme of the Hall bar device geometry to test for long-range effects in oxide thin films away from the area being charged. The spacing of voltage contacts was 300 μ m for all devices. (Reprinted with permission from Ref. 125, Copyright © 2016, X. Leng, A. T. Bollinger and I. Božović)

Recently, a new operating mechanism of ionic liquid-gated metal oxide transistors, i.e. electric field induced formation of oxygen vacancies was proposed by Parkin et al. They fabricated [HMIM][TFSI]-gated pulsed laser-deposited VO_2/TiO_2 (001) and VO_2/Al_2O_3 (1010) transistors in top contact, lateral gate configuration.[37] Metal-insulator transition temperature (MIT) is suppressed to 5 K at V_g =1.8 V. Similar effects of gate bias and oxygen content on MIT of VO_2 suggested that the electrolyte gating effect could be due to the electric field–induced formation of oxygen vacancies (Figure 2-15a and 2-15b). Hall measurement (independent of electron carrier density, n_s on gate voltage, V_g, Figure 2-15c) was used to exclude the electrostatic mechanism. The suppression of the gating effect in O_2 saturated ionic liquid supported their hypothesis furthermore (Figure 2-15d). In a later work, Parkin et al. studied the electronic structure of VO_2 during electrolyte gating.[126] They concluded that the monoclinic structure and the associated orbital degeneracy of the insulating phase is retained but modified by electrolyte gating. Then, in situ X-ray diffraction (XRD) and XAS measurements revealed that the whole film undergoes giant structural changes on gating in which the lattice expands by up to ~3% near room temperature.[127]

Recently, they metallized a 0.5 μm wide VO_2 bar with the c-axis in plane and oriented perpendicular to the length.[128]

Moreover, the crystal facet dependent metallization was also observed in ionic liquid-gated rutile TiO_2 single crystals.[129] Since WO_3 crystal structure has open channels along all three principal crystallographic directions, Parkin et al. metallized WO_3 single crystal films with facet independent.[130] They suggested that the small quantities of oxygen vacancies, induced by electric field, can lead to a phase transition (to higher symmetry phase, from monoclinic to cubic) in WO_3 and consequently significant changes in electronic structure that account for the volume metallization of the oxide.

In summary, there are intense discussions on the device operation mechanism of ionic liquid-gated metal oxide transistors due to the complex interplay of factors determining the doping process, in particular the method of film fabrication. Furthermore, it should be noted that the device geometry, the specific ionic liquid used and the applied electrical bias also affect the working mechanism.

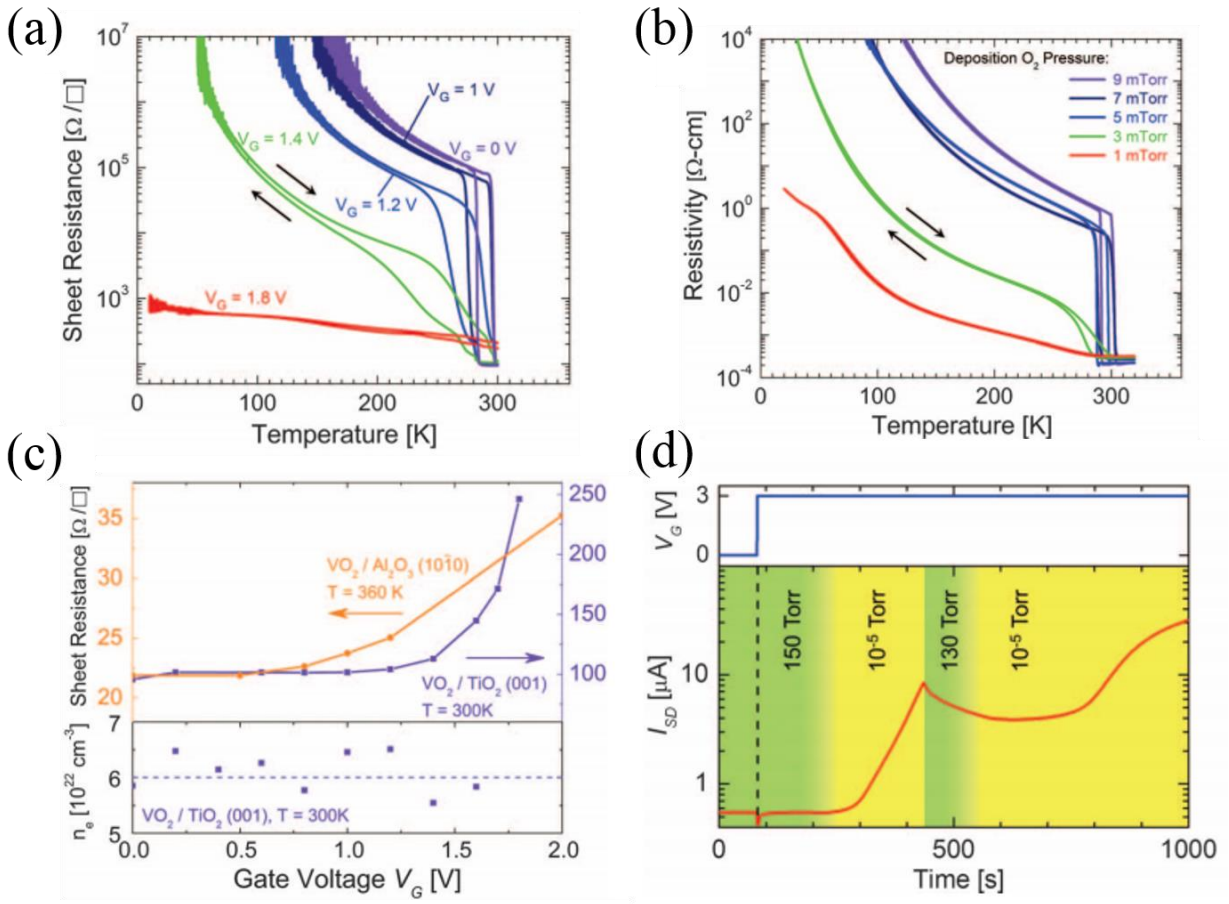

Figure 2-15 Suppression of the metal-insulator temperature in VO_2 films. (a) Sheet resistance vs temperature for various gate voltages for VO_2/TiO_2 (001). (b) Resistivity of VO_2 vs temperature as a function of oxygen pressure during film deposition. (c) Sheet resistance of VO_2 electrolyte-gated devices on TiO_2 (001) and Al_2O_3 (1010) and electron carrier density n_e from Hall measurements for an electrolyte-gated device fabricated from VO_2/TiO_2 (001), vs V_g. The dashed line is a guide to the eye. (d) Source-drain current (device fabricated from VO_2/Al_2O_3 (1010)) vs time as oxygen pressure was varied from 150 torr to 10^{-5} torr to 130 torr and to 10^{-5} torr at V_g = 3 V. (Reprinted with permission from Ref. 37, Copyright © 2013, American Association for the Advancement of Science.)

CHAPTER 3 EXPERIMENTAL METHODS AND TECHNIQUES

In this chapter, we present the synthesis of WO_3, the properties and purification of ionic liquids, the preparation of activated carbon paper and the properties of substrates used in this work, in section 3.1. Afterwards, the procedures for microfabrication, film fabrication and device assembly are illustrated, in section 3.2 and section 3.3. Techniques used in this work are introduced in 3.4.

3.1 Materials

3.1.1 WO_3 synthesis

$Na_2WO_4 \cdot 2H_2O$, Dowex 50WX2 hydrogen form resin (100-200 mesh) and ethanol were purchased from Sigma Aldrich. Poly (ethylene glycol)-200 (PEG-200) was purchased from Fluka Analytical and water used in all experiments was deionized (Milli-Q Millipore, 18.2 M Ω cm at 25 °C). The WO_3 precursor solution was obtained by an aqueous sol-gel method already reported in the literature.[131] 20 mL of 0.5 M Na_2WO_4 aqueous solution was passed through the Dowex 50WX2 proton-exchange resin to get H_2WO_4 solution. The reaction in this step is: $Na_2WO_4 + 2H^+ \rightarrow H_2WO_4 + 2Na^+$. The solution was then collected in 16 mL ethanol under continuous stirring, to slow down the condensation of tungstic acid.[132] After the solution was evaporated under reduced pressure to reach a concentration of ca. 0.5 mol/dm^3, organic stabilizer, 4 mL PEG-200 (WO_3/ PEG-200 ratio was $\approx$ 0.5 w/w) was added to the freshly evaporated stirred solution. The viscous, yellowish precursor obtained (under continuous stirring) was stored in dark condition before precipitation and used to fabricate WO_3 films for three days.

3.1.2 Ionic liquids

An ionic liquid is a salt in liquid state at room temperature.[133] The physical and chemical properties of ionic liquids can vary widely because of the vast selection of anions and cations. Ionic liquids have a wide electrochemical stability window, low vapor pressure, high ionic conductivity, such that they are attractive for electrolyte-gated transistors.[84, 92]

Ionic liquids used in this work were purchased from IoLiTec, (purity > 99 %). Their properties are listed in Table 3-1. The ionic liquids were purified under vacuum (ca 10^{-6} Torr) at 80 °C, overnight

before use, to mitigate any contamination of the ionic liquids, particularly by water. The liquids can be stored in a N_2 glovebox (H_2O and $O_2 \leqslant 5$ ppm) for 1 day at maximum prior use.

Table 3-1 Physicochemical properties of the ionic liquids considered in this PhD work.[134]

Name	Ionic conductivity (mS/cm)	Viscosity (mPa s)	Electrochemical window* (V)		Density (g/cm^3)	Melting point (°C)
			Anodic limit (V)	Cathodic limit (V)		
[EMIM][TFSI]	6.63	39.4	2.6	-2.1	1.52	-3
[PYR_{14}][TFSI]	2.12	94	2.8	-2.5	1.40	-6

* Ag/AgCl reference electrode

3.1.3 Activated carbon paper

Pieces of 6 mm × 3 mm carbon paper (Spectracarb 2050A) were coated with 6 µL high surface area carbon ink. The ink was made of activated carbon powder (PICACTIF SUPERCAP BP10, Pica, 28 mg/mL) and polyvinylidene fluoride (PVDF, KYNAR HSV900, 1.4 mg/mL) binder in N-methyl pyrrolidone (NMP, Fluka, > 99.0%) solvent. The activated carbon paper was dried under vacuum at 60 °C for 5 hours and then stored in a N_2 glovebox (H_2O and $O_2 \leqslant 5$ ppm).

3.1.4 SiO_2/Si and polyimide substrates

Si wafers with 2,000 Å ± 5% dry thermal oxide were purchased from Silicon Quest International (San Jose, California, USA). PolyFLEX XF-102 polyimide film was purchased from Polyonics. The polyimide films were 140 µm thick and able to sustain temperatures as high as 400 °C for short times.

3.2 Microfabrication and substrate cleaning

Microfabrication including photolithography and E-beam deposition were used to pattern coplanar Ti/Au (5/40 nm/nm) source and drain electrodes (channel width, W, 4000 µm and length, L, 10 µm)

on SiO_2/Si and polyimide substrates. Before the photolithography, substrates were wet-cleaned (sequential ultrasonic baths in isopropyl alcohol (IPA), acetone and IPA, then drying by nitrogen) and UV-ozone treated for 15 minutes to remove organic contaminants on the surface. Prior to the photolithography step, silicon wafers were exposed to HMDS primer in the YES vacuum oven to improve the adhesion of the photoresist on them. When the substrates were HMDS treated, a positive photoresist AZ5214-E (MicroChem)/ SPR220.3 (MicroChem) was spin coated at 4000/3000 rpm for 30/40 s to obtain a final thickness of ca. 1 µm/2.5 µm. Then, the substrates were baked at 110 °C for 90 s on the hot plate. Then, photoresist was exposed to the I-line (365 nm wavelength) through proper photomask using a Karl Suss MA6 mask aligner. After post-exposure baking (110 °C, 90 s), the exposed photoresist was removed in the developer AZ 726. E-beam deposition (4 nm Ti/ 40 nm Au) was then performed at 1 Å/s on the patterned substrates. After metal deposition, samples were transferred into PG 1165 remover for the lift-off process. Patterned Ti/Au electrodes will be obtained after two-hour lift-off process. Finally, samples were cut and cleaned in ultrasonic baths with IPA, acetone and IPA, and dried by nitrogen gun.

3.3 Fabrication: thin film and device

WO_3 films were obtained by spreading 10 µL precursor solution on the prepatterned substrate using a glass slide. Afterwards, the films were thermally treated in 80 sccm O_2 flow at a certain temperature, after the films were dried in air for 10 minutes.

After the film deposition, ionic liquid-gated WO_3 transistors were completed by sandwiching a Durapore® GVHP filter separator soaked in the ionic liquid between the WO_3 film and the activated carbon gate electrode. The final device structure is shown in Figure 3-1.

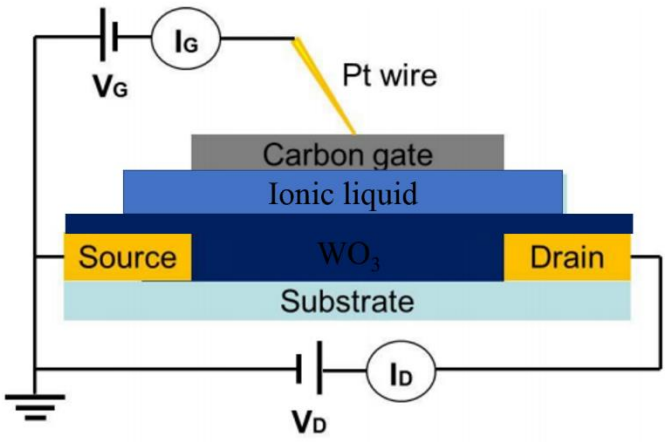

Figure 3-1 Device structure of electrolyte-gated WO_3 transistor fabricated on a SiO_2 substrate with patterned Au source and drain electrodes. A Pt wire was used as a probe to contact the gate electrode.

3.4 Techniques

3.4.1 Electrochemical characterization

Cyclic Voltammetry. Cyclic voltammetry (CV) is one of the most widely used techniques for acquiring analytical (e.g. concentration), thermodynamic (e.g. redox potentials and equilibrium constants), kinetic (e.g. rate constants for reactions involving electrogenerated species) and mechanistic information about electrochemical reactions.[135, 136]

The most common configuration for running CV experiments involves the use of three electrodes, working electrode (WE), reference electrode (RE) and counter (auxiliary) electrode (CE). The current between the working electrode and the counter electrode is plotted versus the potential, which is linearly scanned in triangular potential wave form (single or multiple cycles can be performed) at a fixed rate. The potential is measured between the working electrode and the reference electrode. Figure 3-2a is a typical three electrode system. Figure 3-2b is a potential—time profile to perform cyclic voltammetry and Figure 3-2c is a typical cyclic voltammogram. The reference electrode has a stable electrode potential usually reached by using a redox system with constant concentration of each participant in the redox reaction.[136] Saturated calomel electrode (SCE) and Ag/AgCl electrode are typical examples of reference electrodes. The counter electrode is used to pass the electric current through the solution; it should be non-reactive and of high surface

area to not limit the current flow. The working electrode is the most interesting one since all the significant processes occur here. The electroactive species under investigation can be in the electrolyte or deposited on the working electrode.

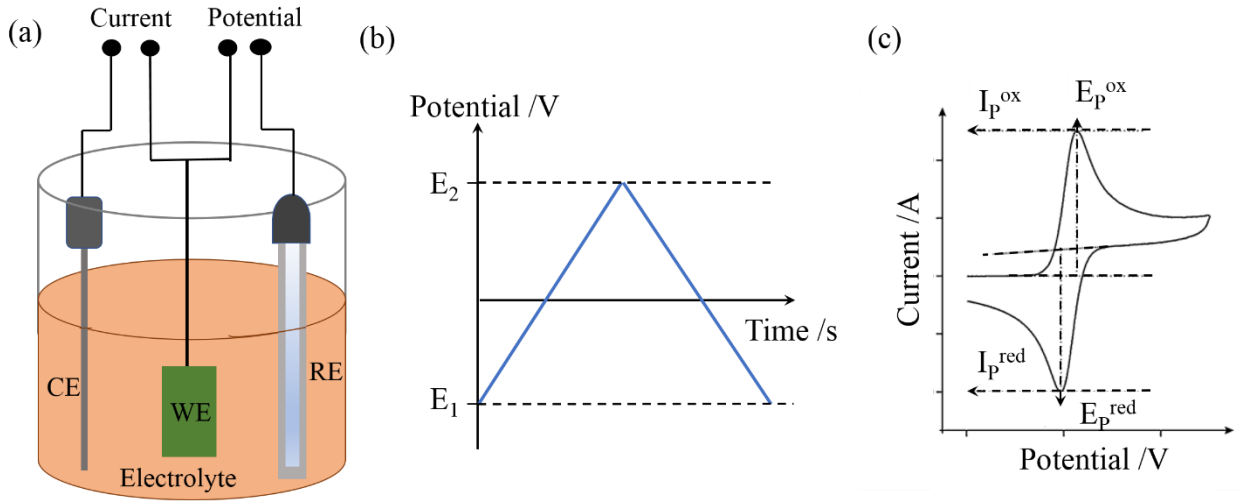

Figure 3-2 Cyclic voltammetry three electrode system cell (a), potential—time profile to perform cyclic voltammetry (b), (c) Cyclic voltammogram depicting the peak positions, E_P, and peak height, I_P.[137]

The electrochemical reaction includes the following steps: mass transfer, i.e. redox species diffuse from the solution to WE surface; electron transfer, i.e. exchange of electrons between the WE surface and the redox species by quantum mechanical tunneling. If the redox species on the electrode surface remain in Nernstian equilibrium throughout the potential scan, the redox process is said to be *reversible.*[138] A reversible process with fast electron transfer has certain characteristics in the cyclic voltammogram, i.e. at all scan rates, ΔE_p (= E_p^{ox} - E_p^{red}) = 59.2/n mV, i_p^{ox}/i_p^{red} = 1 and peak positions do not change and $i_p/\upsilon^{1/2}$ (υ is scan rate) is independent of υ, where n is the number of electrons per molecule involved in the electrochemical process. The peak current for reversible electron transfers is governed by the Randles-Sevcik equation:[139]

$$Ip = 0.446nFAC\left(\frac{nFD\upsilon}{RT}\right)^{1/2}$$

Where A is the electrode area in cm^2, F is Faraday Constant in C mol^{-1}, D is diffusion coefficient in cm^2 s^{-1}, C is concentration in mol/cm^3, R is Gas constant in J K^{-1} mol^{-1} and T is temperature in

K. Thus, peak currents will increase as a function of the square root of the scan rate for reversible electron transfers.

In this PhD thesis, we carried out the cyclic voltammetry characterization in two-electrode configuration, using WO_3 included between source and drain electrodes as the WE and the activated carbon paper as the CE and quasi-RE. The ionic liquid was the electrolyte. Electrochemical tests were performed using a PARSTAT 2273 (Princeton Applied Research) multichannel potentiostat.

Electrochemical impedance spectroscopy (EIS). Electrochemical impedance spectroscopy (EIS) is a powerful technique for characterizing a wide variety of electrochemical systems. The principle of this technique is to apply small amplitude sinusoidal excitation signals to the WE to record the response of the electrode by measuring the phase shift and amplitudes of the current (or voltage) in the time or frequency domain.[140, 141] In the frequency domain, the interface between the electrode and electrolyte can be seen as a combination of resistances, capacitances and inductances. EIS is commonly presented in the form of Bode (frequency vs impedance, frequency vs phase angle) and Nyquist (real part of impedance vs imaginary part of impedance) plots.

In this PhD work, EIS was used to provide information on the capacitive behavior of the electrolyte/semiconductor interfaces. Impedance spectra were obtained within the frequency range 10 mHz -10 kHz, with a perturbation of 10 mV. The electrochemical cell configuration and measurement conditions are the same as the CV measurements.

3.4.2 Transistor characterization

The electrolyte-gated transistor characterization was conducted using a semiconductor parameter analyzer (SPA, Agilent B1500A) coupled with a micromanipulator probe station installed in an N_2 glovebox (H_2O and $O_2 \leq 10$ ppm). The electrolyte-gated phototransistor characterization was performed in vacuum condition (ca 10^{-6} bar). As source of illumination during the phototransistor characterization, we used a solar light simulator (ORIEL® VERASOL-2 solar simulator).

3.4.3 Structural and compositional characterizations

SEM. Scanning electron microscopy (SEM) is a typical technique to investigate the morphology of samples by scanning the surface with a focused electron beam. According to the interaction

locations between the electron beam and atoms of the sample, different signals are produced: secondary electrons, emitted from the surface of the sample, carry the sample morphology information; back scattered electrons, emitted from deeper locations within the sample, provide information about the distribution of different elements in the sample; characteristic X-rays, emitted when the electron beam removes an inner shell electron from the sample, are used for quantitative analysis of the chemical composition of the sample.

SEM images of WO_3 films deposited on different substrates were obtained with a Microscope JEOL JSM7600F, in Secondary Electron Mode, at an operating voltage of 10 kV and a working distance of 5 mm.

AFM. Atomic force microscopy (AFM) is a characterization method that can be applied to thin film research to gain insight on the surface topography of films with high resolution. AFM can be operated in different modes: static mode (contact mode), where the tip is "dragged" across the surface of the sample and the feedback signal is used to keep the cantilever at a constant position; dynamic mode (tapping and non-contact mode), where the cantilever is vibrated or oscillated at a given frequency.[142]

For a hard surface such as a metal oxide, to avoid damaging the microcantilever tip, tapping mode is preferred for studying the nanoscale morphology and roughness of thin films. Samples were scanned in ambient conditions, in tapping mode, with a Digital Instruments Dimension 3100 (Santa Barbara, CA) combined with a Veeco Nanoscope V controller (Bruker). Tapping mode was performed at a scan rate of 1 Hz using etched silicon cantilevers (ACTA from Applied Nanostructures, Inc.) with a resonance frequency around 300 KHz, a spring constant of 40 N/m and tip radius < 10 nm. All images were acquired with medium tip oscillation damping (20% – 30%).

XPS. X-ray photoelectron spectroscopy is the most widely used surface analysis technique and can quantitatively provide elemental and chemical state information from the surface of the material.[143]

In this work, XPS was used to determine the W oxidation state after electrolyte gating. XPS were carried out on a VG ESCALAB 3 MKII spectrometer with a monochromatized Mg Kα source operated at 300 W (15 kV and 20 mA), an electron take-off angle of 0°, and steps of 1.0 eV for an

energy pass of 100 eV. Power analysis covered a surface of 2 mm × 3 mm and depth of 5-10 nm. The background was subtracted by the Shirley method using the Wagner sensitivity factor table.

Infrared Spectroscopy. Infrared spectroscopy is used to obtain the chemical bonds and functional groups information of a sample. When the frequency of the incident IR is the same as the vibrational frequency of a bond or collection of bonds, molecules are excited from the ground vibration state to a higher energy vibration state, i.e. absorption occurs.[144]

The attenuated total reflection (ATR) Fourier transform infrared spectroscopy (ATR-FTIR) measurements were performed in ambient conditions with a Digilab mid-IR microscope (FTS7000e spectrometer coupled to a UMA600 infrared microscope) in rapid scan mode at room temperature, using a micro-ATR Germanium crystal and doing a coaddition of 512 scans at 8 cm^{-1}spectral resolution. The analysis spot size is 100 μm^2.

Raman. Raman spectroscopy is also a powerful tool used to obtain vibrational, rotational and other low-frequency modes information of a system based on inelastic scattering.[145, 146] When a laser light strikes a molecule, the photons excite the molecule, in either the ground or rovibronic state, into a virtual energy state for a short time and then the photons are scattered with either lower or higher energy than the incident light. The shift in energy gives information about the functional groups and chemical bonds of the system. Raman also provide information about crystallinity of inorganic samples.

In the present work, Raman spectra were obtained in ambient conditions with a Renishaw Invia Raman microscope with a CCD detector. A 514-nm line from an Ar laser was used as the excitation source and a power of 50 mW was incident on the sample. The spectra were collected using a 50× collection objective.

XRD. X-Ray Diffraction (XRD) gives information about crystallinity, crystal orientation, phases, composition, internal lattice strain and particle size of crystalline materials.[147] When X-rays impinge upon a set of planes in a crystal, only if the specific conditions defined by Bragg's law ($n\lambda = 2d\sin\theta$, where d is the interplanar spacing of the crystal, θ is the incident angle, n is any integer, and λ is the wavelength of the beam) are satisfied, diffraction occurs. The diffraction pattern of a material can be produced by measuring the diffraction angles and intensities of diffracted beams.

The structure of the WO_3 films was investigated by XRD with a Bruker D8 diffractometer using a (Cu Kα) beam. X-ray scans were measured every $2\theta = 0.01$ and the time per step was 0.6 s.

3.4.4 Optical characterization

UV-Visible Spectroscopy UV-Visible spectroscopy is widely used in the semiconductor industry to measure the optical properties of thin films. In this work, A Perkin Elmer LAMBDA 1050 spectrophotometer equipped with an integrating sphere was used to obtain the UV-visible absorption spectra. The total transmittance (T) was measured by placing the film at the entrance of the sphere at normal incidence whereas the film was placed at the back of the sphere for measurements of the total reflectance (R) at 8 degrees in conjunction with using a light trap to eliminate the transmitted component. The absorbance (A) was obtained from A=1-T-R.

3.4.5 Other characterization

TGA Thermogravimetric analysis (TGA) is a thermal analysis method to obtain the information of a physical or chemical change of a material by measuring the material's mass loss or gain as a function of increasing temperature (with constant heating rate).[148] The system consists of a sample pan supported by a precision balance. The sample pan is located inside a furnace with a programmable control temperature. The mass of the sample is monitored during the temperature changing.

TGA of our WO_3 powders were performed using a TA Instruments TGA 2950 Thermogravimetric Analyzer to determine the organic and adsorbed water contents in the sample. The samples were brought from room temperature to 600 °C under N_2 atmosphere (90 cc/min), at a heating rate of 10 °C/min. The WO_3 powders we used were obtained by scratching WO_3 films from the glass substrates where they were overgrown.

BET Brunauer-Emmett-Teller (BET) is an important analysis technique for the measurement of the specific surface area of a material by physical adsorption of gas molecules. In BET surface area analysis, nitrogen is usually used because of its availability in high purity and its strong interaction with most solids. During the measurement, nitrogen gas is exposed to a solid under investigation at liquid nitrogen conditions (i.e. 77 K). The surface area of the solid is evaluated from the measured monolayer capacity and knowledge of the cross-sectional area of nitrogen molecule.

During this PhD work, BET single point specific surface area measurements were performed with an Autochem II 2920 Micrometrics, equipped with a TCD detector to determine the specific surface area of nanostructured WO_3 films.

Profilometer Profilometry is a tool used to measure film surface topography and film thickness. There are two types of profilometers: stylus vs optical. During this PhD work, Dektak 150 Profilometer, which is based on stylus profiler technology, was used to determine the thickness of differently processed tungsten oxide films. During the measurement, the probe was physically moved along the film surface to acquire the surface height.

CHAPTER 4 ARTICLE 1: ELECTROLYTE-GATED WO_3 TRANSISTORS: ELECTROCHEMISTRY, STRUCTURE, AND DEVICE PERFORMANCE

This article has been published in the Journal of Physical Chemistry C in 2015. It reports low voltage WO_3 transistors gated with [TFSI]-based ionic liquid. The electrochemistry properties, structure transformation of WO_3 film during biasing and working mechanism were investigated. The supporting information for this article is reprinted in Appendix A of this thesis. In this article, Prof. Clara Santato, Prof. Francesca Soavi and I designed the work. I conducted the experimental work which includes 1) WO_3 precursor synthesis, 2) Au electrodes microfabrication on SiO_2 substrate by photolithography, 3) device assembly, 4) WO_3 films morphology and structure characterization by AFM, XRD (assisted by Dr Nima Nateghi), XPS (assisted by Dr. Josianne Lefebvre), Raman (assisted by Dr. Samir Elouatik), ATR-FTIR (assisted by Dr. Samir Elouatik), BET (assisted by Dr. Marta Maria Natile) and TGA (assisted by Eduardo Di Mauro) characterization, 5) film electrochemistry and transistor performance characterization. I analyzed and interpreted the majority of the data. I wrote the first draft and was involved in the paper revision and final editing of the manuscript.

4.1 Authors

Xiang Meng,[1] Francis Quenneville,[1] Frédéric Venne,[1] Eduardo Di Mauro,[1] Dilek Işık,[1] Martin Barbosa,[1,2] Yves Drolet,[1] Marta M. Natile,[3] Dominic Rochefort,[4] Francesca Soavi,[5] and Clara Santato[1,*]

1. Département de Génie Physique, Polytechnique Montréal, C.P. 6079, Succ. Centre Ville, H3C 3A7, Canada

2. Departamento de Físico-Química, Universidade Estadual Paulista, Rua Professor Degni, 55, Araraquara, 14800-060, Brazil

3. CNR-IENI, Dipartimento di Scienze Chimiche, Università di Padova, Via F. Marzolo 1, 35131, Italy

4. Département de Chimie, Université de Montréal, C.P. 6128, Succ. Centre Ville, H3C 3J7, Canada

5. Dipartimento di Chimica "Giacomo Ciamician", Università di Bologna, Via Selmi, 2, 40126,

*E-mail: clara.santato@polymtl.ca

4.2 Abstract

Electrolyte-gated (EG) transistors, based on electrolyte-gating media, are powerful device structures that modulate the charge carrier density of materials by orders of magnitude, at relatively low operating voltages (sub-2 V). Tungsten trioxide (WO_3) is a metal oxide semiconductor well investigated for applications in electrochromism, sensing, photocatalysis and photoelectrochemistry. In this work, we report on EG transistors making use of mesoporous nanostructured WO_3 thin films easily permeated by the electrolyte as the transistor channel and bis(trifluoromethylsulfonyl)imide [TFSI]-based ionic liquids as gating media. The WO_3 EG transistors operate at ca. 1 V. Using a combination of cyclic voltammetry, X-ray diffraction and transistor performance characterizations, complemented by spectroscopic (Raman and infrared) investigations, we correlate the metal oxidation state and the charge transport properties of the metal oxide, shedding light on the doping process in electrically-biased WO_3 nanostructured thin films exposed to electrolytes.

KEYWORDS: Electrolyte-gated transistors, WO_3 thin films, Ionic liquids, Doping,

Thin film structure

4.3 Introduction

The intrinsic technological interest of electrolyte-gated (EG) transistors which make use of electrolytes as the gating media is paralleled by their relevance as experimental platforms to study fundamental aspects of combined electronic and ionic transport, charge carrier transport at high charge density and charge density modulation to modify the electronic properties of materials.[36, 76, 81, 92, 149-153] EG transistors are indeed attracting attention because of their low driving voltages (< 2

V) as well as the possibility of achieving charge carrier density as high as ca. 10^{14}-10^{15} cm^{-2}, owing to the high capacitance of the electrolyte/transistor channel interface (ca. 1-10 $\mu F \cdot cm^{-2}$).

Different electrolytes have been used as gating media in EG transistors, such as aqueous electrolyte solutions and ionic liquids (ILs).[36, 154] ILs are molten salts at relatively low temperature (100 ºC and below) featuring physicochemical properties suitable for their use in EG transistors. Indeed, by selecting the appropriate structure for the cation and anion, ILs can be designed to have a limited volatility, good ionic conductivity, low viscosity, high thermal stability, and a wide electrochemical stability window (up to ca. 5 V).[95, 96]

Different mechanisms can be invoked to explain the doping process leading to current modulation in EG transistors. Such mechanisms depend on a number of factors, including the nature of the transistor channel material and the electrolyte.

In electrical double layer EG transistors, the doping results from an electrostatic process at the electrolyte/channel interface, similar to that for field-effect transistors. Upon application of an electrical bias to the gate electrode, a redistribution of the ions of the electrolyte at the electrolyte/gate and electrolyte/channel interfaces takes place, paralleled by accumulation (depletion) of charge carriers in the transistor channel, which is impermeable to ions. On the other hand, in electrochemical EG transistors, the channel material undergoes a reversible faradic doping (dedoping) that can extend into the bulk of the channel. The application of a gate bias induces a reversible redistribution of ions within the transistor channel and the electrolyte that together with charge injection from source and drain, results in electrochemical doping (dedoping) of the channel, which is permeable to ions. Oxygen vacancies created by strong electric fields between the ionic liquid and the metal oxide channel have been invoked to explain the working mechanism of EG transistors making use of metal oxide channels.[37]

Metal oxide thin films have been widely investigated for a wide range of applications such as transistor materials for active matrix displays, light-emitting diodes, transparent conductive electrodes, energy conversion and energy storage devices.[25, 155-161] Among metal oxides, tungsten trioxide (WO_3, band gap ca. 2.5 eV) stands out in electrochromism, sensing, photocatalysis and photoelectrochemistry applications, in which performance is usually enhanced for high surface area mesoporous nanostructures, easily permeated by electrolytes.[65, 69, 162, 163] Such applications involve modulation in the charge carrier density. After an early report from Wrighton et al., [164]

several groups recently described the possibility of modulating the charge carrier density and, in general, enhance the charge carrier transport properties in WO_3 in transistor configuration.[165-168] In these recent reports, WO_3 was prepared by different techniques and in different forms, such as high-temperature and low-temperature sputtered films and two-dimensional nano-flakes, and often the gating was based on the use of electrolytes as the gating media.

In EG transistors based on channels of mesoporous nanostructured metal oxide thin films, the high surface area of the channel is expected to play a primary role in establishing the doping mechanism. Here, besides electrostatic and conventional faradic doping, which involves insertion/deinsertion of ions in the oxide lattice, the possibility of a non-conventional electrochemical doping, confined at the electrolyte/metal oxide interface, should be contemplated especially for electrolytes made up of ions with relatively large size, which may not be able to be inserted in the oxide lattice. Such electrochemical interface-confined doping, being characterized by no or limited ion insertion, is expected to improve the operational stability of the electrolyte/channel interface. It seems, therefore, interesting to study the electrolyte gating process in transistors based on mesoporous nanostructured metal oxide films interfaced to ionic liquids based on large ions. Our study aims at improving the fundamental understanding of electrolyte/metal oxide interfaces to pave the way towards mechanically integer, stable devices making use of ionic liquid and ionic liquid-based (e.g. ion gels) electrolytes for applications in optoelectronics, solar energy conversion and electrochromics.

In this work, we report on EG transistors making use of mesoporous nanostructured WO_3 thin films as the channel material and ionic liquids differing for their conductivity, viscosity and electrochemical stability window, as the gating media. A facile synthetic route based on a *chimie douce* approach (sol-gel) was used to prepare the WO_3 thin films.[131] We performed an electrochemical characterization of the WO_3 thin films paralleled by a structural characterization upon application of an electrical bias and characterized the EG transistor performance, thus opening the possibility of correlating the metal oxidation state and the charge transport properties of the metal oxide.

4.4 Experimental Method

4.4.1 Microfabrication, materials and device assembly

Ti/Au (5/40 nm/nm) source and drain electrodes were photolithographically patterned (channel width, *W*, 4000 µm and length, *L*, 10 µm) on cleaned SiO_2 substrates. Tungstic acid, prepared using an aqueous sol-gel method already reported in the literature, [131] was spread on pre-patterned cleaned SiO_2 substrates to form thin films. The films were subsequently thermally treated in 80 sccm oxygen flow at 550 °C to obtain the nanostructured, semiconducting thin film transistor channels (ca 200 nm thick) for 30 min. A Durapore® GVHP membrane filter soaked with the ionic liquid was placed on top of the transistor channel. The ionic liquids were purchased from IoLiTec, (purity > 99%). Prior to their use, the ionic liquids were purified under vacuum (ca 10^{-6} Torr) at 80 °C, overnight, and stored in a N_2 glove box (H_2O and $O_2 \leq 5$ ppm) for one day at maximum prior to their use. The gate electrode consisted of a carbon paper (Spectracorp 2050, 6 mm × 3 mm) coated with high surface area carbon ink made of activated carbon powder (PICACTIF SUPERCAP BP10, Pica, 28 mg/mL) and polyvinylidene fluoride (PVDF, KYNAR HSV900, 1.4 mg/mL) binder in N-methyl pyrrolidone (NMP, Fluka, > 99.0%) solvent. The final device structure is shown in Figure 4-1.

4.4.2 Characterization

Brunauer–Emmett–Teller (BET) single point specific surface area measurements were performed with an Autochem II 2920 Micrometrics, equipped with a TCD detector. From the BET measurement, we deduced a specific surface area of 14 m^2/g for our nanostructured WO_3 thin films. Thermogravimetric analyses (TGA) of WO_3 powders were performed using a TA Instruments TGA 2950 Thermo-gravimetric Analyzer. The samples were brought from room temperature to 600 °C under N_2 atmosphere (90 cc/min), at a heating rate of 10 °C/min. For both BET and TGA measurements, we used WO_3 powders obtained by scratching WO_3 films from the glass substrates where they were overgrown. Raman spectra were obtained in ambient conditions with a Renishaw Invia Raman microscope with a CCD detector using a 50 mW Ar (514 nm) laser. The spectra were collected using a 50× collection objective. The Attenuated Total Reflection (ATR) Fourier Transform Infrared Spectroscopy (ATR-FTIR) measurements were performed in ambient conditions with Digilab mid-IR microscope (FTS7000e spectrometer coupled to a UMA600

infrared microscope) in rapid scan mode at room temperature using a micro-ATR Germanium crystal and doing a co-addition of 512 scans at 8 cm^{-1} spectral resolution. The analysis spot size is 100 µm. X-ray diffraction (XRD) measurements were performed by a Bruker D8 system with Cu Kα1 and Cu Kα2 sources. To study possible structural changes in doped WO_3, XRD spectra were collected after biasing WO_3-on-ITO electrodes at -0.6 or -1 V for 5 mins: the chronoamperometry experiment was carried out in two-electrode configuration, WO_3-on-ITO electrode/[EMIM][TFSI]/activated carbon electrode, to mimic the transistor stacking. Electrochemical tests were performed using a PARSTAT 2273 (Princeton Applied Research) multichannel potentiostat. The transistor characterization was conducted by using a semiconductor parameter analyzer (SPA, Agilent B1500A). Electrochemical and electronic characterizations were performed in a N_2 glove box (H_2O and O_2 ca. 10 ppm).

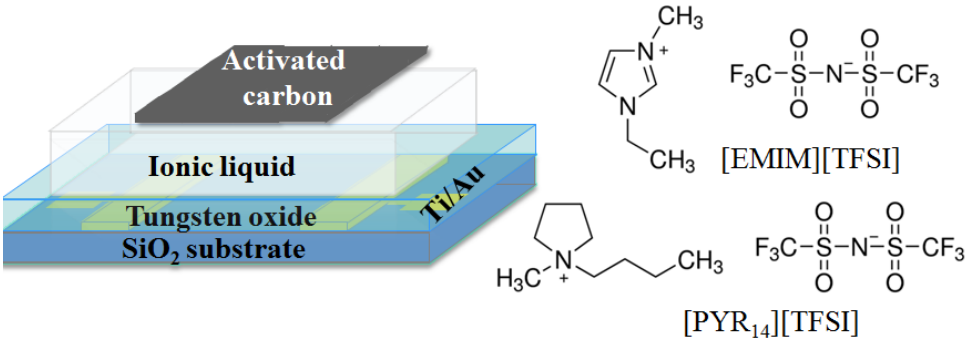

Figure 4-1 Schematic of the ionic liquid-gated WO_3 EG transistor studied in this work. Durapore® GVHP membrane filter soaked with the ionic liquid was put on top of the transistor channel, carbon paper coated with high surface area carbon ink was set in contact with the membrane and used as the gate electrode. Molecular structures of the ionic liquids [EMIM][TFSI] and [PYR_{14}][TFSI] were used to gate the transistors.

4.5 Results and Discussion

4.5.1 Electrochemistry and XRD characterization

The electrochemical characterization of the transistor channel material is a key step to gain insight on the doping mechanism of EG transistors. In this work we used, as the electrolyte, two ionic liquids, namely [EMIM][TFSI] (1-ethyl-3-methylimidazolium bis(trifluoromethylsulfonyl)imide, ionic conductivity 6.63 $mS \cdot cm^{-1}$, viscosity 39.4 mPa·s, at 20 °C) and [PYR_{14}][TFSI] (1-methyl-1-butylpyrrolidinium bis(trifluoromethylsulfonyl)imide, ionic conductivity 2.12 $mS \cdot cm^{-1}$, viscosity 94 mPa·s, at 20 °C).[134] [EMIM][TFSI] is an ionic liquid with a relatively high ionic conductivity whereas [PYR_{14}][TFSI] features a wide electrochemical stability window (ca 5.3 V) and it is particularly stable towards reduction. We carried out the channel cyclic voltammetry characterization *in situ*, in two-electrode configuration, using WO_3 included between source and drain electrodes as the working electrode and the activated carbon paper as the counter and quasi-reference electrode. Due to its high capacitive response, the potential of the activated carbon electrode does not significantly change during the cyclic voltammetry, thus offering the possibility to use it as quasi-reference electrode.[169-171] When the cyclic voltammetry is performed in such two-electrode configuration, the potential applied between the working electrode and the activated carbon quasi-reference electrode corresponds to $-V_g$ (gate-source voltage) in the transistor configuration. As shown in Figure 4-2a and b, for both [EMIM][TFSI] and [PYR_{14}][TFSI], cyclic voltammetry indicates that the electrochemical reduction of WO_3 starts at ca. 0.25 V vs. activated carbon and suggests that our WO_3 EG transistors can safely operate at relatively low V_g values, included between ca. -0.25 V and 1.5 V.

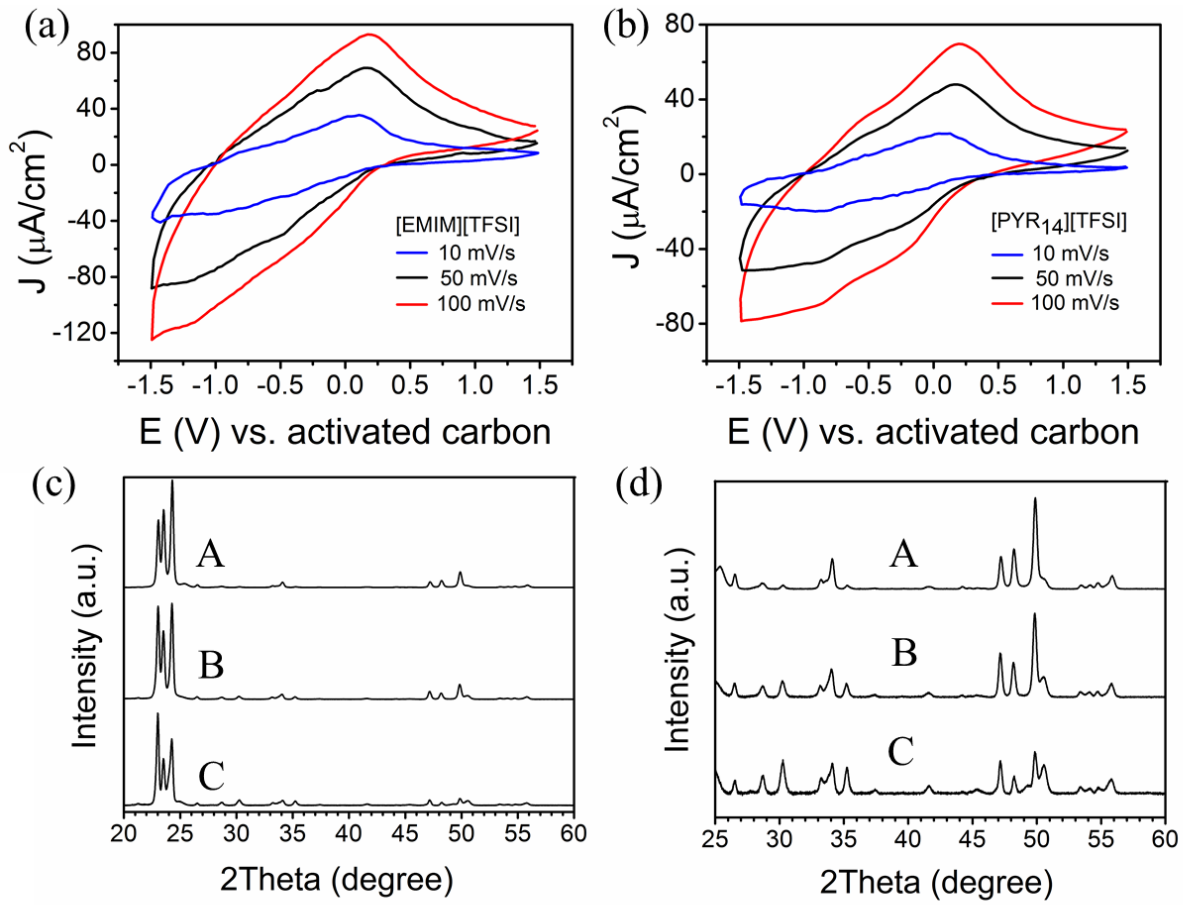

Figure 4-2 Cyclic voltammetry of the WO_3 channel in transistor configuration with [EMIM][TFSI] (a) or [PYR_{14}][TFSI] (b) as the electrolyte, at various scan rates (10, 50, and 100 mV/s). XRD patterns in the 20°-60° (c) and in the zoomed 25°-60° region (d) obtained from: as-prepared WO_3 films -on-ITO (A), WO_3 films-on-ITO electrodes biased for 5 min at -0.6 V (B) and -1 V (C), in [EMIM][TFSI].

For a scan rate of 50 $mV \cdot s^{-1}$, the cyclic voltammetry plot shows a cathodic shoulder and a broad peak located at ca -0.5 V and -1.2 V for [EMIM][TFSI] and -0.2 V and -0.9 V for [PYR_{14}][TFSI]. An anodic peak is also observable, located at ca. 0.2 V for both ionic liquids. The peaks of the voltammetric anodic current increase linearly with the square root of the scan rate (Figure S1), suggesting that the rates of the redox processes are diffusion-limited.[136] The values of the current are generally larger for [EMIM][TFSI] than for [PYR_{14}][TFSI], as expected considering the lower viscosity and higher ionic conductivity of the former ionic liquid with respect to the latter.

During the cathodic scan, upon electron injection, structural changes can take place in the WO_3 thin films. Literature reports that, in electrolytes including H^+, the structure of WO_3 changes from monoclinic to orthorhombic, to tetragonal and eventually to cubic, upon decrease of the W oxidation state from +6 to +5.9 to +5.85 and < +5.5.[44, 172] In electrolytes including Li^+, monoclinic WO_3 undergoes structural transitions to tetragonal (at ca. 2.8 V vs Li^+/Li) and finally to cubic (at ca. 2.55 V vs Li^+/Li) structures, upon decrease of the W oxidation state from +6 to +5.865, and <+5.865.[39] Considering that the activated carbon reference used in this work is located at ca. +3.0 V vs the Li^+/Li electrode,[171, 173] the shoulders and the broad peaks observed during the cathodic scans in our Li-free electrolytes could be associated to structural transitions taking place in the WO_3 thin films. We therefore followed the evolution of the structure of the WO_3 thin films in [EMIM][TFSI]. XRD patterns (Figure 4-2c) show that the diffraction peaks of as-prepared WO_3 films-on-ITO can be fitted with a monoclinic structure.[131] Biasing WO_3 films-on-ITO at -0.6 V and -1 V involved a doping charge of -0.48 mC and -3 mC, respectively, which correspond to the change of the average oxidation state of W from +6 to +5.993 and +5.96 (Figure S2 and calculations in SI). After application of an electrical bias, we observed significant changes in the XRD patterns (Figures 2 c and d). In the 22°-25° region (Figure 4-2c), the change in the relative intensity within the triplet peak suggests the presence of a transition from the WO_3 monoclinic to the orthorhombic phase.[131, 174] This is also confirmed by XRD pattern evolution in the 25°-60° region (Figure 4-2d). Indeed, the application of an electrical bias of -0.6 V results in the increase of the relative intensity of the peaks at 28.6° and 47.2°, compared to 26.6° and 48.4°. Upon application of an electrical bias of -1 V, the relative intensity of the peaks at 28.6° and 47.2° further increased. This increase is attributable to the formation of (111) and (002) diffraction planes in orthorhombic WO_3.[174] The weak broad peak in the pattern of as-prepared films in the 41°-42° region is attributable to the overlap of two diffraction peaks at 41.2° and 41.7°, corresponding to (-222) and (222) diffraction planes of monoclinic WO_3. After application of the electrical bias, a single peak located at ca. 41.5° is observable, attributable to the (221) diffraction plane of orthorhombic WO_3. Furthermore, a new peak appears in the 49°-49.5° region for WO_3 films biased at -1 V, attributable to the (400) diffraction plane in the orthorhombic structure (Table S1 in SI).

The voltammetric doping charges for a cathodic scan in [EMIM][TFSI], limited at -0.5 V (shoulder in the cyclic voltammogram) and -1.2 V (peak in the voltammogram) are -0.17 mC and -0.70 mC (for the same cathodic limits the charges are -0.15 mC and -0.45 mC for $[PYR_{14}][TFSI]$). For

[EMIM][TFSI], these charges lead to the average oxidation state of W of +5.993 and +5.97 (calculations in SI). These values compare well with those calculated for WO_3-on-ITO electrodes studied by XRD. It is therefore reasonable to expect the voltammetric response of WO_3 being shaped by the phase transition observed by XRD, as reported above.

4.5.2 Transistor characterization

The transfer characteristics in the saturation regime (drain-source current, I_{ds}, versus V_g, at a drain-source voltage, V_{ds} = 1 V) and the output characteristics (I_{ds} versus V_{ds} for increasing V_g) for WO_3 transistors gated with [EMIM][TFSI] (Figure 4-3a) and [PYR_{14}][TFSI] (Figure 4-3b) show n-type semiconductor behavior. During the forward scan, two shoulders are observable in the plot I_{ds} vs. V_g, at ca. 0.5 and 1.0 V for [EMIM][TFSI] and one at ca. 0.9 V for [PYR_{14}][TFSI]. During the backward scan a shoulder appears at ca. -0.1 V for [EMIM][TFSI] and 0 V for [PYR_{14}][TFSI].

In both ionic liquids, the transfer characteristics show hysteresis, related to the V_g scan rate. The hysteresis increases with the decrease of the scan rate (Figure S3): longer biasing times during the forward scan permit to a larger amount of ions from the ionic liquid to pack at the interface electrolyte/WO_3 or to protons from water traces to be inserted in the films (Figure S4) such that relatively long times are required to relax the ions during the backward scan. The larger hysteresis observed for [EMIM][TFSI] is attributable to the formation of a denser layer of cations in proximity of the surface of the WO_3 nanoparticles for [EMIM] compared to [PYR_{14}], in turn due to the relatively small size of [EMIM] (theoretically deduced radius of 3.5 Å) with respect to [PYR_{14}] (radius of 3.9 Å).[175, 176]

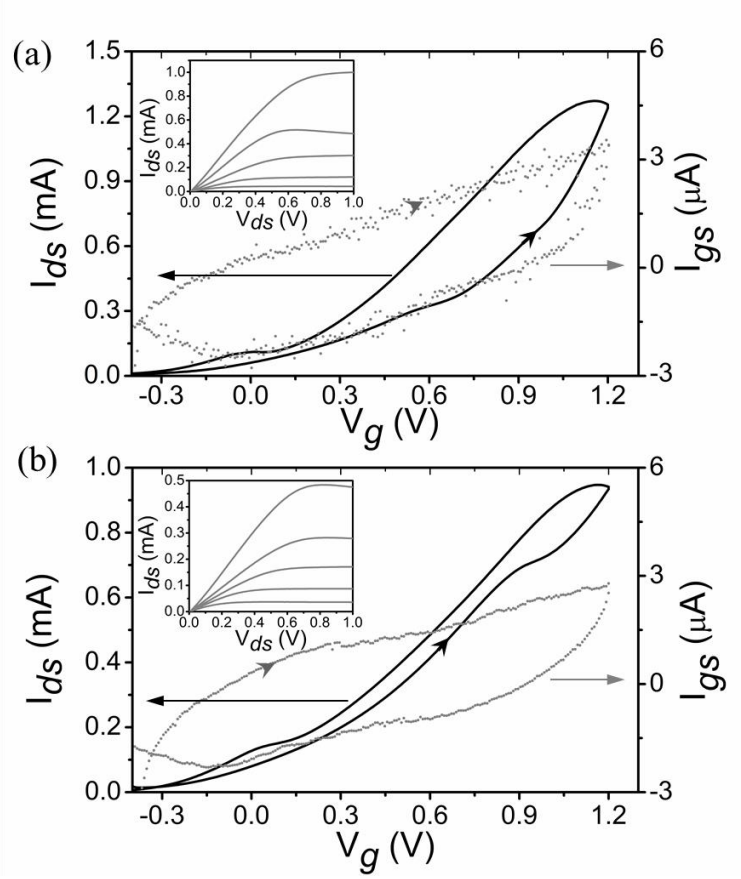

Figure 4-3 Transfer characteristics of (a) [EMIM][TFSI]-gated and (b) [PYR_{14}][TFSI]-gated WO_3 transistors in the saturation regime (V_{ds} = 1 V). I_{ds} (left axis, black solid line) and I_{gs} (gate-source current, right axis, gray dotted line) plotted vs. V_g, scan rate is 10 $mV \cdot s^{-1}$. Inset: output characteristics, V_g = 0 V to 0.8 V in steps of 0.2 V, V_{ds} scan rate is 10 $mV \cdot s^{-1}$.

For our ionic liquid-gated WO_3 thin film transistors, the I_{on}/I_{off} ratios (calculated from I_{ds} at V_{gs} =1.2 V (I_{on}) and -0.4 V (I_{off}), V_{ds} = 1 V) were ca. 10^2 for [EMIM][TFSI]- and [PYR_{14}][TFSI]-gated transistors.

The electron mobility, μ, was calculated in the linear regime of the transistors (V_{ds} = 0.3 V, Figure S5) from:

$$\mu = j_{ds}/(Eep) = (I_{ds}/ep)\,(L/W\,V_{ds}) \qquad \text{Eq. (4.1)}$$

Where j_{ds} is the source-drain current density, E is the electric field and p is the charge carrier density. To determine p, we integrated I_{gs} vs. time, during the linear forward transfer scan according to:[106, 177]

$$p = Q/eS = [\int (I_{gs}\, dV_g)]/[(dV_g/dt)\, eS] \qquad \text{Eq. (4.2)}$$

where Q is the WO_3 doping charge and S is the surface area of WO_3 in contact with electrolyte (S is 8 cm^2, calculations in the SI).

The doping charge, charge carrier density and mobility in the linear region (*vide infra* for the saturation mobility) were ca. 0.72 mC, $6 \cdot 10^{14}$ cm^{-2}, 0.05 $cm^2 \cdot V^{-1} \cdot s^{-1}$ for transistors making use of [EMIM][TFSI] and 0.30 mC, $2.5 \cdot 10^{14}$ cm^{-2}, 0.08 $cm^2 \cdot V^{-1} \cdot s^{-1}$ for $[PYR_{14}][TFSI]$. The volumic charge carrier density is ca. $6 \cdot 10^{20}$ cm^{-3} and $2.5 \cdot 10^{20}$ cm^{-3} for [EMIM][TFSI]- and $[PYR_{14}][TFSI]$-gated transistors, respectively (calculations in SI).

As observed for the saturation regime, in the linear regime, shoulders are also observable in the transfer characteristics for similar electrical biases applied (V_g ca. 0.5 and 1.0 V for [EMIM][TFSI]). We tentatively establish a correlation between the shoulders observed in the forward/backward scans of the transfer transistor characteristics and the shoulders and broad peaks in the cyclic voltammograms (cathodic/anodic scans), in turn associated with structural changes from the monoclinic to the orthorhombic structure of the WO_3 thin films. Indeed, the charge accumulated in the WO_3 thin films during transfer linear characteristics is 0.1 mC and 0.23 mC (for a V_g limit of 0.5 and 1.0 V during the forward scan, Figure S5a), leading to average oxidation states for W of +5.996, +5.99 similar to those of biased WO_3 films-on-ITO studied by XRD. It appears therefore reasonable to suggest that structural changes accompany the change of the W oxidation state during the recording of the transfer characteristics.

Furthermore, the fact that the shoulders in the forward transfer characteristics are associated with an increase in the slope of the I_{ds} vs V_g plot suggests a change in the mechanism of charge carrier transport with the increase of V_g, associated with the structural changes of the WO_3 thin films.

The electron mobility for [EMIM][TFSI]-gated transistor calculated from the slope of the $I_{ds}^{1/2}$ vs. V_g curve in the saturation regime is ca. 0.2 $cm^2 \cdot V^{-1} \cdot s^{-1}$ (Figure S6). The difference in the values of

the electron mobility in linear vs. saturation conditions is attributable to the non-optimal injection properties of the Au electrodes into WO_3.[178, 179]

4.5.3 Mechanism of doping

In principle, different scenarios are possible to explain the doping mechanism in our EG transistors. We will consider at first the possibility of electrochemical doping. The calculation of the electrochemical doping charge can be carried out as follows. The charge needed to dope W from the oxidation state +6 to +5 would be $Q_{electrochem} = n \cdot N_A \cdot e$, where n is the number of moles of WO_3 available for doping, N_A is Avogadro number and e is the elementary charge. Calculations for the electrochemical mechanism of doping for our samples, where $n = 2.5 \cdot 10^{-7}$ mol (calculations in SI) would lead to about 25 mC. This value has to be compared with 0.72 mC as deduced from Eq. (2) for experiments run in [EMIM][TFSI] and 0.30 mC for $[PYR_{14}][TFSI]$. We deduce that only ca. 3% (1.2%) (i.e. 0.72 mC (0.30 mC)/ 25 mC) of the total WO_3 available is doped in a typical transistor experiment (transfer linear characteristics) run at a scan rate of 10 $mV \cdot s^{-1}$, with a cathodic limit of V_g = 1.2 V, in [EMIM][TFSI] ($[PYR_{14}][TFSI]$). The relatively low percentage of doped WO_3 is in agreement with the large size of the cations of the ionic liquid that cannot be inserted in the relatively small cages (size of ca. 4 Å) of monoclinic WO_3.[180]

For a pure electrostatic mechanism, we can estimate the doping charge as follows: $Q_{electrostatic} = C \cdot S \cdot V_{gs}$, where C is the specific capacitance of the ionic liquid and S is the surface area of the WO_3 exposed to the electrolyte. Considering that S is 8 cm^2, that the specific capacitance of [EMIM][TFSI] in the configuration Pt/[EMIM][TFSI]/Pt is ca. 7 $\mu F \cdot cm^{-2}$ and that V_{gs} is 1.2 V, we obtain a value for the electrostatic doping charge of 0.067 mC.[4] If we compare this value with the charge deduced from Eq. (2), it is possible to conclude that likely the electrostatic mechanism cannot solely explain the extent of the doping in the films. This conclusion is in clear agreement with the type of electrochemical signal (faradic) generated by the WO_3 films during the cyclic voltammetry survey.

The discussion above calls for several contributions to explain the doping process in our mesoporous nanostructured WO_3 thin films. If, certainly, the electrostatic contribution has to be taken into account, electrochemical contributions also have their place. Besides conventional electrochemical contributions (where protons from water traces are inserted into the WO_3) electrochemical doping confined at the electrolyte/WO_3 interface should not be excluded.

4.6 Conclusions

The electrochemical, structural and device characteristics of EG transistors making use of mesoporous nanostructured WO_3 thin film channels and ionic liquids as the gating media were studied. The transistors can operate at voltages as low as 1.0 V and charge carrier density larger than 10^{14} cm^{-2} can be obtained. We propose a correlation between the cyclic voltammetry behavior of the channel material, structural changes observed by XRD in the material upon application of an electrical bias, as well as transistor transfer characteristics, anomalously shaped. Despite the large size of the ions, the doping mechanism in the films cannot be purely electrostatic since the cyclic voltammetries show a clear faradic behavior. Such electrochemical behavior can be explained by a combination of conventional electrochemical doping, where the electrons injected upon application of an electrical bias are compensated by the insertion of protons from water traces during the measurements, and non-conventional interface-confined electrochemical doping, where the injected electrons are compensated by the large cations of the ionic liquid packing at the interface.

We are currently characterizing the structural and optical changes taking place in WO_3 transistors gated by ionic liquids and ion gels in *situ*, during the application of the electrical bias. We also plan to investigate the effect of the electrical bias on the properties of the surface of our nanostructured WO_3 by X-ray Photoelectron Spectroscopy to shed light on the oxygen vacancy formation as a significant contribution to the doping. Our research efforts, bridging the knowledge between the metal oxidation state and the charge transport properties of the metal oxide, are expected to lead to high performance interfaces and devices with improved stability with broad potential impact in the fields such as transistors for active matrix displays and energy conversion and storage devices.

4.7 Acknowledgments

The authors are grateful to Prof. F. Cicoira and I. Valitova for fruitful discussions, F. Boutet for technical support and Dr. S. Elouatik for Raman and ATR-FTIR experiments and discussions. This work was financially supported by FRQNT (Team grant) and NSERC (Discovery, C.S.). X.M. acknowledges financial support by the China Scholarship Council and CMC Microsystems (MNT program). F.S. acknowledges financial support by Università di Bologna (Researcher Mobility Program, Italian-Canadian cooperation agreement).

CHAPTER 5 ARTICLE 2: ELECTROLYTE-GATED PHOTOTRANSISTORS BASED ON TUNGSTEN OXIDE FILMS

This article has been submitted to Advanced Materials Interfaces. It reports low voltage WO_3 phototransistors gated with [EMIM][TFSI]. The electrical, photosensitivity and photoresponsivity behavior of the low temperature tungsten oxide film on SiO_2 and polyimide substrates in (photo)transistor configuration were investigated. The supporting information for this article is reprinted in Appendix B of this thesis. In this article, Prof. Clara Santato and I designed the work. I did the majority of the experimental work which includes 1) synthesis of the WO_3 precursor by the sol-gel method, 2) microfabrication of the Au electrodes on SiO_2 and polyimide substrates by photolithography, 3) deposition of the WO_3 thin films at different temperatures on microfabricated substrates, 4) assembly of the devices, 5) characterization of WO_3 films morphology and structure by Atomic Force Microscopy and X-ray Diffraction, 6) characterization of the electrochemistry by cyclic voltammetry, 7) characterization and optimization (in terms of film thickness) of the device electronic and optoelectronic performance in transistor configuration under simulated solar light. I analyzed and interpreted the data. I first drafted the paper and was involved in the final editing of the manuscript.

5.1 Authors

Xiang Meng,[1] Shiming Zhang,[2] Martin S. Barbosa,[1,3] Bill Baloukas,[1] Daniel Chartrand,[4] Fabio Cicoira[2] and Clara Santato[1]*

1. Département de Génie physique, Polytechnique Montréal, C.P. 6079, Succ. Centre-ville, Montréal (QC) H3C 3A7, Canada

2. Département de Génie chimique, Polytechnique Montréal, C.P. 6079, Succ. Centre-ville, Montréal (QC) H3C 3A7, Canada

3. Departamento de Físico-Química, Universidade Estadual Paulista, Rua Professor Degni, 55, Araraquara, 14800-060, Brazil

4. Département de Chimie, Université de Montréal, C. P. 6128, Succ. Centre-ville, Montréal (QC) H3C 3J7, Canada

5.2 Abstract

We report on ionic liquid-gated phototransistors based on tungsten oxide semiconducting films, operating at about 1 V, fabricated both on rigid and flexible substrates. The temperature of thermal treatment of the sol-gel films dramatically affects the phototransistor behavior. Polycrystalline films treated at 550 ºC, operated in vacuum conditions, show persistent photoconductivity, i.e. they remain conductive in the absence of light, thus limiting their interest for phototransistor applications. On the other hand, films treated at 300 °C, a temperature compatible with the use of polyimide plastic substrates, are persistent photoconductivity-free, i.e. the current decreases once the light is switched off. In particular, with respect to SiO_2 substrates, device fabricated on polyimide shows improved performance in terms of ON/OFF ratio and photosensitivity. These low temperature tungsten oxide films, characterized for their electrical, photosensitivity and photoresponsivity behavior in transistor configuration, are promising for a new generation of large-area light detectors operating at low voltage.

KEYWORDS: Electrolyte-gated transistors, Phototransistors, Tungsten oxide, Films, Ionic Liquids

5.3 Introduction

Metal oxides are a class of materials widely investigated in energy storage, field emission, sensing and thin film transistor devices.[181-189] Particularly, the unique electrochemical, electronic and optical properties of metal oxide semiconductors make them attractive for multifunctional devices, such as electrochemical transistors, electrochromic transistors and phototransistors.[114, 165, 190] Phototransistors, widely used in security systems, light sensing devices and computer logic circuitry, use light to generate charge carriers, in addition to electrical bias applied at the gate electrode.[191] The behavior of phototransistors is explained by a photovoltaic effect when they operate in accumulation mode and by a photoconductive effect when they operate in depletion mode (the increase of the optical power leads to the increase of the transistor current).

Several materials have been investigated for applications in phototransistors, namely metal oxides,[190, 192] organic semiconductors,[191] colloidal nanocrystals,[193, 194] solution processable $CH_3NH_3PbX_3$ (where X is Cl, Br, or I) perovskites[195, 196] and two-dimensional materials.[197, 198] Among metal oxides, ZnO, SnO_2, In_2O_3 and IGZO (Indium Gallium Zinc Oxide) have been investigated (see Table S1). Despite intense research efforts, several aspects of the behavior of phototransistors, with both fundamental and practical relevance, are still undiscovered. In particular, there is a need to shed light on the combined effect of optical and electrical inputs, at high charge carrier density, on the phototransistor behavior. This situation occurs, for instance, when operating electrolyte-gated transistors under illumination (see Table S2). In electrolyte-gated transistors, the high capacitance (ca $1-10$ $\mu F \cdot cm^{-2}$) featured by electrolyte/transistor channel interfaces leads to high charge carrier densities ($10^{14}-10^{15}$ cm^{-2}),[36, 149] which permit operation at low voltages (< 2 V). Therefore, understanding the effect of the illumination in films featuring high charge density on their optoelectronic behavior will have a practical impact on the feasibility of low-voltage electrolyte-gated phototransistors. The demonstration of low-voltage phototransistors, together with processability on plastic substrates at low temperature, are expected to extend the applications of this class of devices.[199-201]

We recently demonstrated ionic liquid ([EMIM][TFSI])-gated transistors making use of channels of polycrystalline films of tungsten oxide, a semiconductor well investigated for applications in electrochromism, sensing, photocatalysis and photoelectrochemistry.[44, 163, 202-204] We observed that film doping takes place by a combination of electrostatic and electrochemical mechanisms, paralleled by a structural transformation of the metal oxide from the monoclinic to the orthorhombic crystal structure.[205]

In this work, we report on electrolyte-gated phototransistors making use of sol-gel deposited tungsten oxide films, on rigid and flexible substrates. We used an ionic liquid as the gating medium and high surface area carbon as the gate. We characterized the effect of the gate bias on the photosensitivity and photoresponsivity of the phototransistors. Finally, we discuss important effects played by the atmosphere where the devices are operated, either in ambient or vacuum conditions, on the phototransistor feasibility and behavior.

5.4 Results and Discussion

5.4.1 Photosensitive electrolyte-gated transistors (EGT) based on polycrystalline tungsten oxide films, operated in ambient conditions and under vacuum

We initially performed the characterization of EGT based on tungsten oxide polycrystalline films treated at high temperature (550 °C), both in the dark and under illumination. We used this type of films, well-known for their photoelectrochemical and transistor behavior, for a first demonstration of metal oxide electrolyte-gated phototransistors on rigid and flexible substrates, operating at low voltage. The morphology and crystal structure of the films have already been systematically studied in a previous work.[131] In ambient conditions, the transfer and output characteristics of our devices (see Figure 5-1a and 1b) show the typical signatures of n-type transistors working in accumulation mode. Under illumination (390-1100 nm, see Experimental section), the transfer (I_{ds} *vs* V_g) and output (I_{ds} *vs* V_{ds}) curves show a dramatic increase of the transistor current, as expected for our photosensitive tungsten oxide films (see Figure S1) whereas no major change was observed for the gate current (I_{gs}). The hysteresis observed in the transfer curves is likely due to the slow ionic transport limiting the doping of the films during the forward scan and, at least in part, the dedoping during the backward scan. We already reported on the effect of the scan rate on the transfer characteristics[197]: the current increased by a factor of 10 upon decrease of the scan rate from 100 mV/s to 1 mV/s. Rather low values of the ON/OFF ratios (calculated between V_g = 0.8 V, ON, and V_g = 0 V, OFF), i.e. 25 and 10, were obtained in the dark (I_{off} = 3×10^{-8} A) and under illumination (I_{off} = 1.6×10^{-7} A), mainly due to the high intrinsic conductivity of the polycrystalline oxide films. Transient current measurements, carried out under chopped light in ambient conditions, reveal that the current responds slowly to the illumination and does not reach a plateau. In addition, the current response to the illumination decreases for consecutive cycles (Figure 5-1c). This limited stability of the photoresponse in ambient air is attributable to the adsorption of water by the ionic liquid inducing metal oxide surface reactions.[81] On the basis of these results, we decided to characterize our devices under vacuum.

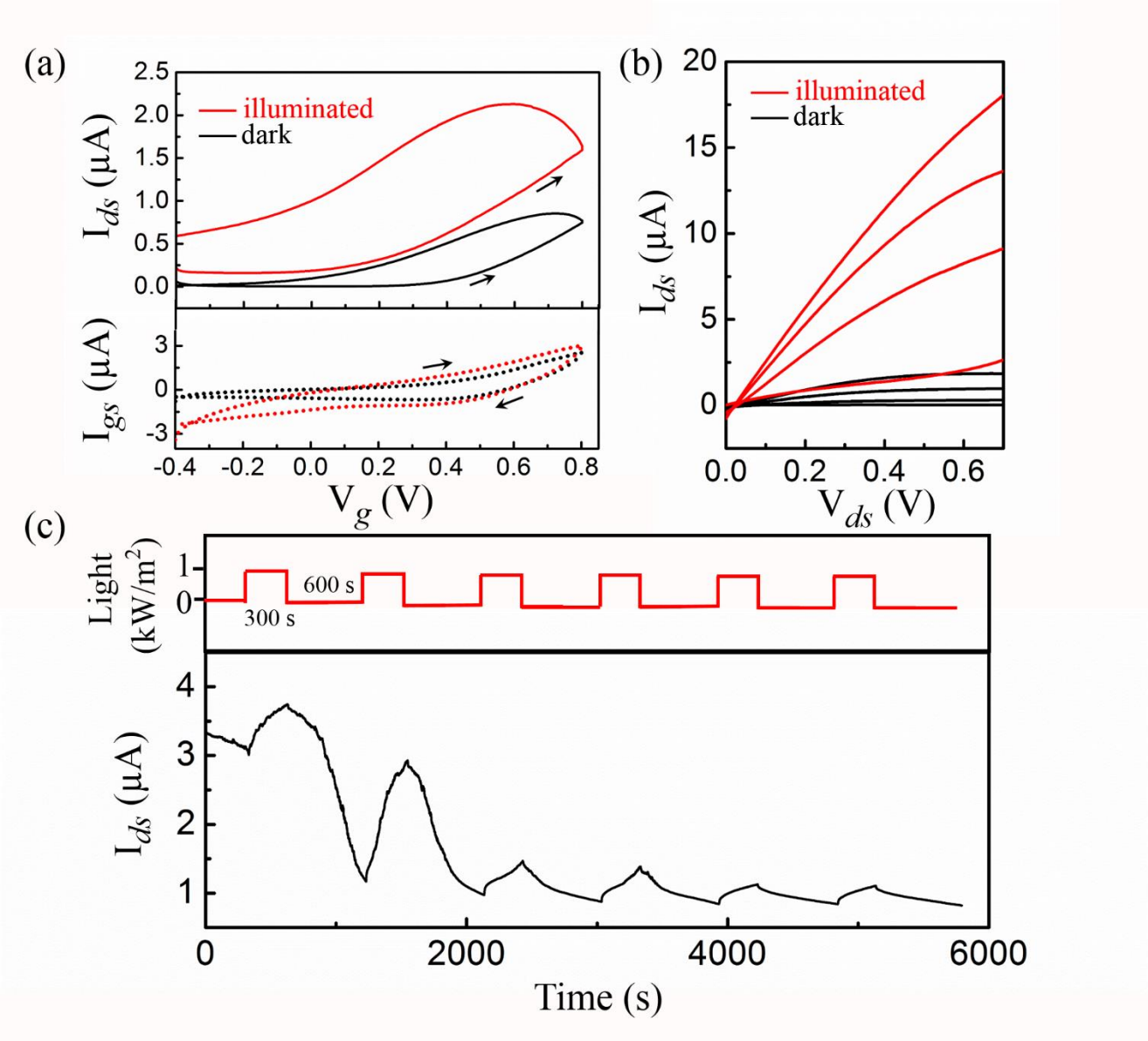

Figure 5-1 [EMIM][TFSI]-gated photosensitive transistors based on tungsten oxide films (483 ± 47 nm-thick) treated at 550 °C on SiO_2 substrates, characterized in ambient conditions. (a) Transfer characteristics in the linear regime (V_{ds} = 0.2 V), V_g scan rate 10 mV·s^{-1}, in the dark (black) and under illumination (red). (b) Output characteristics in the dark and under illumination, V_g = 0, 0.4, 0.6, 0.8 V, V_{ds} scan rate 10 mV·s^{-1}. (c) Transient (I_{ds} - time) measurements under chopped light (light on, light off indicated by red line) at V_{ds} = 0.2 V, V_g = 0.1 V.

When performing the transistor measurements under vacuum, we observed a dramatic increase of the transistor current upon illumination (about one order of magnitude, Figure 5-2a and 5-2b). In addition, the increased electrochemical stability of the devices permitted to apply higher gate biases (1.2 V) with respect to measurements carried out in ambient conditions (0.8 V). The transfer characteristics show that the transistor current under illumination, at the end of the backward scan, is close to the initial value. The values of the ON/OFF ratio were 25 in the dark (I_{off} = 1.1×10^{-6} A) and 4 under illumination (I_{off} = 1.6×10^{-5} A).

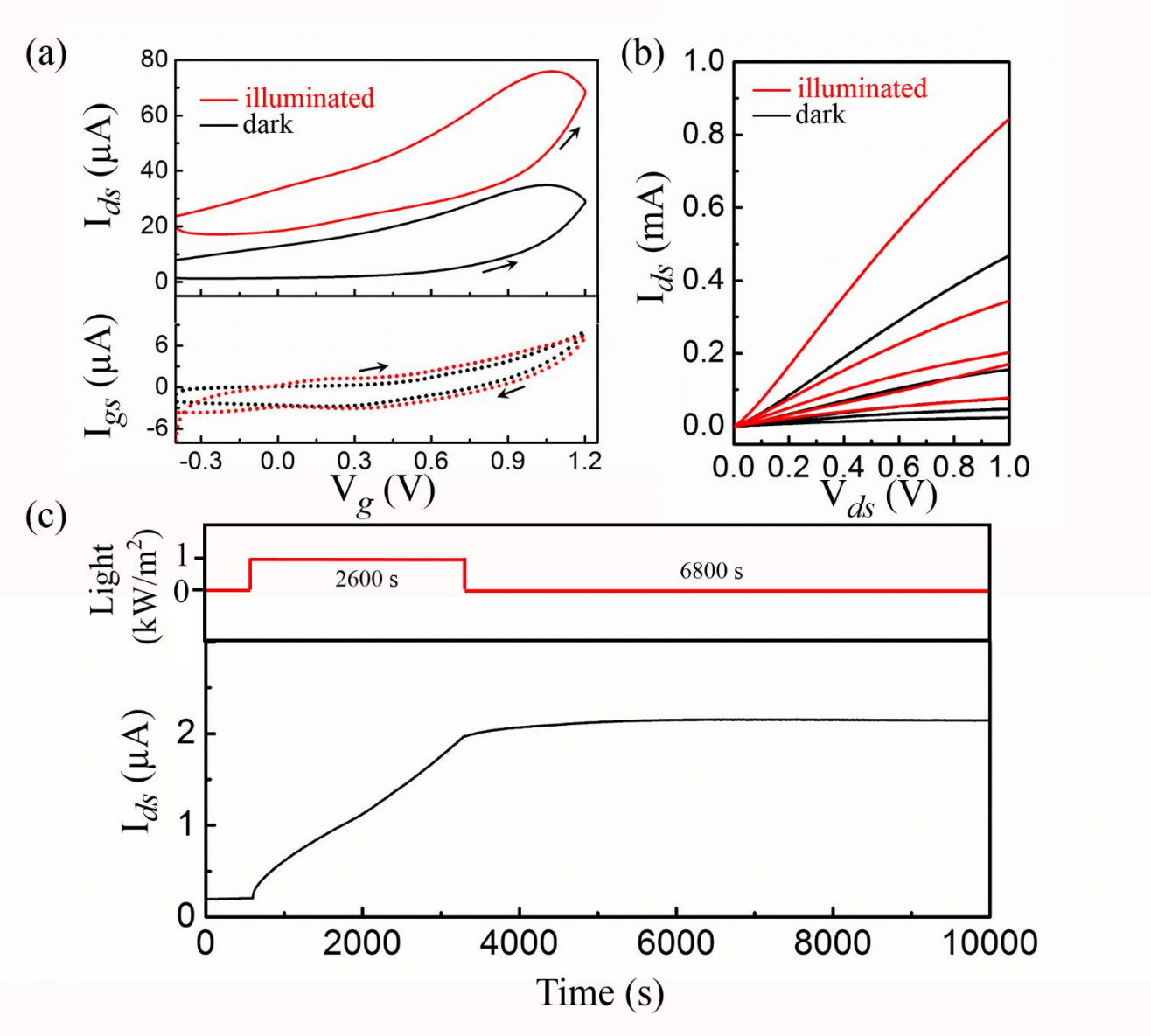

Figure 5-2 [EMIM][TFSI]-gated photosensitive transistors based on tungsten oxide films (483 ± 47 nm-thick) treated at 550 °C on SiO_2 substrates characterized in vacuum. (a) Transfer characteristics

in the linear regime (V_{ds} = 0.2 V), V_g scan rate 10 mV·s^{-1}, in the dark (black) and under illumination (red). (b) Output characteristics in dark and under illumination, V_g = 0, 0.6, 0.8, 1.0, 1.2 V, V_{ds} scan rate 10 mV·s^{-1}. (c) I_{ds}-time measurements under chopped light (indicated by red line) at V_{ds} = 0.2 V, V_g = 0.1 V.

Importantly, the transient characteristics of the devices under illumination, measured in vacuum conditions, revealed that the transistor current does not recover its initial (dark) value (Figure 5-2c) when the light is switched off, i.e. the current preserves a constant state and holds more than 5 × 10^3 s without any significant decay. This observation is explained by the persistent photoconductivity (PPC) phenomenon observed in metal oxides, whose nature is still the object of debate. One possible mechanism is that the persistent photoconductivity is caused by the ionization of oxygen vacancy (V_O) sites, i.e. the deep, neutral V_O states are ionized to shallow donor states (V_O^{2+}) under illumination with λ < 550 nm as $V_O \rightarrow V_O^{2+} + 2e^-$.[206-208] The outward relaxation of bonds surrounding the V_O sites then creates an energy barrier against neutralization of V_O^{2+}sites, thus keeping the material in a state of high conductivity. However, this mechanism prevents us from explaining the current recovery when the samples are measured in ambient conditions (Figure 1C). Another possible mechanism is that the persistent photoconductivity is due to the electron–hole separation related to the surface properties of the nanostructured metal oxide.[209-210] In dark conditions, oxygen molecules in air adsorb onto the metal oxide surface, trapping conduction electrons from the bulk.[210] As a result, the adsorbed oxygen on the surface is negatively charged and the space charge region is positively charged, i.e. a built-in electric field is formed.[211] In oxygen-rich atmospheres (ambient air), the width of the depletion layer grows, and thus lowers the electrical conductance of the materials. In contrast, a thinner depletion layer occurs with low pressure oxygen atmospheres (vacuum) and higher conductance values are obtained. This prediction is in agreement with our experimental data: I_{off} (air) = 3×10^{-8} A ≪ I_{off} (vacuum) = 1.1×10^{-6} A. Under illumination, photons generate electron–hole pairs in the bulk of the materials. At the same time, electron–hole pairs recombine in different ways. Besides the fast band-to-band recombination, indirect electron–hole recombination, i.e. holes accumulate near the surface under the built-in electric field and discharge the adsorbed oxygen (leaving an unpaired electron, inducing an increase in the electrical conductivity) dominates the photoresponse in nanostructured materials.[210] When the light is switched off, the two recombination mechanisms contribute to recover the initial current in ambient condition: the band-to-band recombination mechanism

rapidly extinguishes holes in the inner part of the film, the remaining unpaired electrons are responsible for the persistent photoconductivity which can only be reverted by the indirect oxygen-assisted recombination mechanism. However, in vacuum condition because of the absence of molecular oxygen, the indirect recombination cannot occur, so no decay current can be observed.

5.4.2 Electrolyte-gated phototransistors based on tungsten oxide films treated at 300 °C

The persistent photoconductivity phenomenon limits the interest of polycrystalline tungsten oxide films operated under vacuum for electrolyte-gated phototransistor technologies, although this aspect might be useful for other types of technologies, such as photonic neuromorphic devices.[212]

To eliminate the PPC related to surface effects, films with smooth, featureless surfaces (that is, low temperature-treated amorphous films) were employed. We were able to suppress the persistent photoconductivity and achieve electrolyte-gated phototransistors operating in vacuum conditions. Transient current measurements carried out under chopped light conditions on films treated at 300 °C, featuring smooth surfaces and amorphous microstructure (Figure S2), clearly show that when the light is switched off, the current rapidly decreases to the dark current value (Figure 5-3a).

The transfer and the output characteristics of *thin* tungsten oxide films treated at 300 °C, operated under vacuum, showed, as expected, n-type transistor current modulation (Figure 5-3b and 5-3c), alike transistors making use of films treated at 550 °C. The values of the ON/OFF ratio were 500 and 100, in the dark ($I_{off} = 1.6\times10^{-7}$ A) and under illumination ($I_{off} = 1.2\times10^{-6}$ A). We clearly observe that, decreasing the film thermal temperature from 550 °C to 300 °C, leads to a net improvement of the switching properties of the transistors operated under vacuum conditions. These characteristics make these devices promising for phototransistor applications.

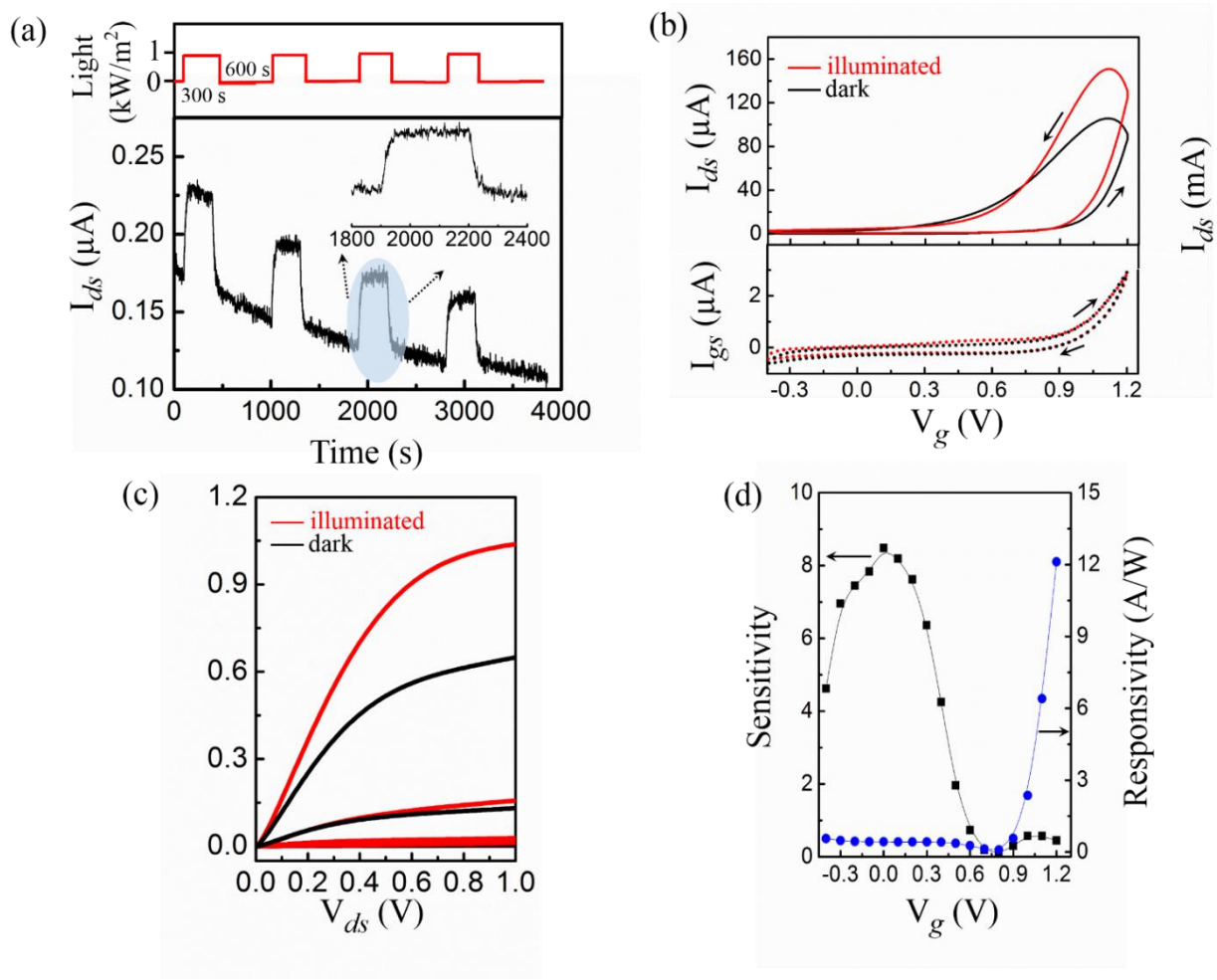

Figure 5-3 [EMIM][TFSI]-gated phototransistors based on tungsten oxide films (120 ± 26 nm-thick) treated at 300 °C on SiO_2 substrates, characterized in vacuum. (a) I_{ds}-time measurements under chopped light (indicated by red line), at V_{ds} = 0.2 V, V_g=0.1 V. (b) Transfer characteristics in the linear regime (V_{ds} = 0.2 V), V_g scan rate 10 mV·s^{-1}; dark (black) and illumination (red) conditions. (c) Output characteristics under dark and illumination conditions, V_g=0, 0.6, 0.8, 1.0, 1.2 V, V_{ds} scan rate 10 mV·s^{-1}. (d) Responsivity and sensitivity vs V_g recorded at V_{ds} = 0.2 V; lines are guides for the eye.

The electron mobility, μ, was calculated in the linear regime of the transistors as $\mu = L \cdot I_{ds}/(W \cdot e \cdot p \cdot V_{ds})$, where e is the elementary charge and p is the charge carrier density (charge carrier/cm^2).[177] The charge carrier density was extracted from $p = Q/e \cdot S = [\int(I_{gs}\, dV_g)]/[(dV_g/dt) \cdot e \cdot S]$, where Q is the doping charge obtained by integrating I_{gs} vs time during the transfer forward scan

and S is the surface area of tungsten oxide in contact with the electrolyte (0.36 cm^2). In the dark, we extracted a charge carrier density of 7×10^{14} cm^{-2} and a mobility of 1×10^{-2} $cm^2/V\cdot s$. Work is in progress to establish the long-term shelf life and operational stability, including electrochemical, of the devices. No dramatic changes were observed under illumination, where we deduced a charge carrier density of 9×10^{14} cm^{-2} and a mobility of 1×10^{-2} $cm^2/V\cdot s$.

We then studied the behavior of two key figures of merit of phototransistors: the sensitivity, defined as $(I_{ds}\text{-}I_{ds,dark})/I_{ds,\,dark}$, and the responsivity, defined as $(I_{ds}\text{-}I_{ds,dark})/P\cdot s$, where P is the power density of the incident light and s is the geometric area of the channel.[213] Upon increasing V_g from -0.3 to 1.2 V, we observed an increase of the sensitivity at the beginning of the sweeping with a maximum at ca. 0 V, followed by a decrease (Figure 5-3d). The values of the sensitivity are included between ca. 8.5 (V_g = 0 V) and 0.1 (V_g = 0.8 V). This behavior can be explained considering that at low V_g most of the charge carriers are photogenerated, whereas at high V_g most of them are produced by the action of the electrical bias applied to the gate. The dependence of the sensitivity on V_g can be exploited to control the light response of the phototransistors. The behavior of the responsivity (obtained considering $s = L\times W = 4\times10^{-4}$ cm^2) as a function of V_g, also shown in Figure 3d, reveals an increase by a factor of 120 going from 0.8 V (R is 0.1 A/W) to 1.2 V (R is 12 A/W). The value of the responsivity at V_g = 1.2 V is comparable with the value reported for reduced graphene oxide-WO_3 hybrid photodetectors (R = 6.3 A/W, Table S3). Measurements of the transistor current for increasing values of the light power show the weak effect of the power on the current (at least for the range of power densities investigated, i.e. between the dark conditions and 1 kW/m^2): the current is 1.2 µA for 0.25 kW/m^2 illumination and 1.4 µA for 1 kW/m^2 illumination, at V_g = 0 V and V_{ds} = 1 V (Figure S3).

The working mechanism of our electrolyte-gated phototransistors can be explained as follows. In absence of any V_g applied, in the dark, due to the n-type nature of our tungsten oxide films, the Fermi level is close to the conduction band edge. The illumination leads to the photogeneration of charge carriers, which are, at least in part, trapped. In this (photoconductive) regime, the responsivity remains low. As V_g increases (photovoltaic regime), the large amount of charge carriers accumulated upon application of the gate bias fills the traps, thus shifting the Fermi level towards the conduction band, resulting in an increased responsivity.

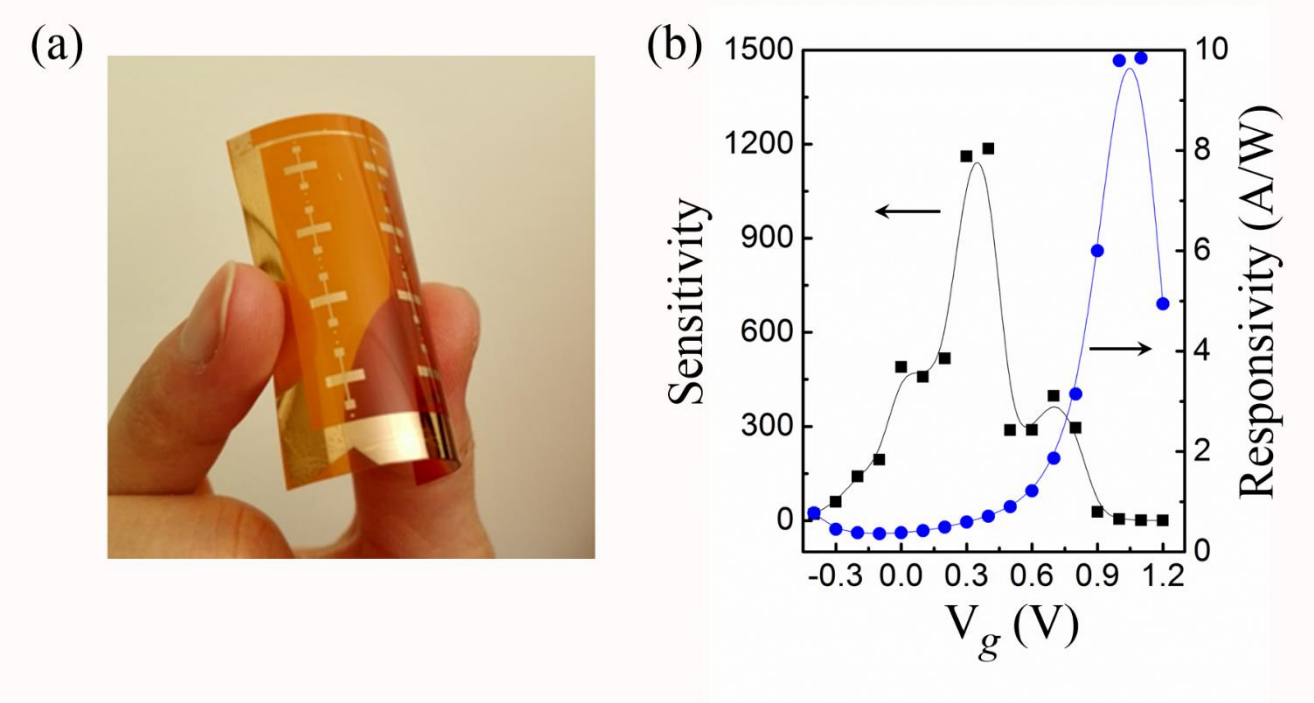

Figure 5-4 [EMIM][TFSI]-gated phototransistors based on tungsten oxide films (153 ± 25 nm-thick) treated at 300 °C on polyimide substrates, characterized in vacuum. (a) Au-patterned PI substrates. (b) Responsivity and sensitivity vs V_g recorded at V_{ds} = 0.2 V. Lines are guides for the eye.

5.4.3 Structural and electrochemical characterization of tungsten oxide films on polyimide and corresponding ionic-liquid gated phototransistors

Considering the fact that using a thermal treatment temperature of 300 °C, films operated under vacuum give persistent photoconductivity-free phototransistors and since this temperature is compatible with film processing on polyimide substrates, we investigated the possibility of fabricating phototransistors on flexible polyimide substrates.

To fabricate tungsten oxide electrolyte-gated phototransistors on flexible substrates, films were deposited on Au-patterned polyimide and treated at 300 °C (Figure 5-4a). The films showed good adhesion on the polyimide substrates. XRD patterns show that the films are amorphous, a favorable feature for efficient ionic transport (Figure S4a). SEM images reveal the presence of nanometric voids, also expected to favor ionic conduction (Figure S4b). The tungsten oxide films on polyimide were then electrochemically characterized in transistor configuration. Cyclic voltammetry measurements were carried out with the films included between source and drain electrodes as the

working electrode and the activated carbon paper gate as the counter and quasi-reference electrode (Figure S4c). The cyclic voltammograms show an electrochemical reduction starting at ca. -0.6 V vs activated carbon followed by a weak, broad oxidation signature during the backward voltammetric scan. Our n-type EGT on polyimide (Figure S4d and S4e), in dark conditions, featured ON/OFF ratios of ca. 6×10^4 (I_{off} = 2.5×10^{-9} A), a dramatic improvement with respect to films treated at 550 °C as well as to those treated at 300 °C deposited on SiO_2. For phototransistors on polyimide, in the dark, we deduced a charge carrier density of 9×10^{14} cm^{-2} and an electron mobility of 1×10^{-2} $cm^2/V\cdot s$ (using the integration of the gate current, as described before). Under illumination, the ON/OFF ratio was ca. 1.4×10^4 (I_{off} = 1.2×10^{-8} A), the charge carrier density 3×10^{15} cm^{-2} and the mobility 5.5×10^{-3} $cm^2/V\cdot s$. The slightly lower values of the mobility obtained under illumination might be due to the effect of the high charge carrier density produced under illumination.[214] Comparing films on polyimide to *low* temperature, *thin* films on SiO_2, the main difference is the lower I_{off} on polyimide, both under dark and illumination conditions. A higher density of defects in tungsten oxide films grown on polyimide, more discontinuous than films on SiO_2, can explain the lower I_{off}. The characteristics of the phototransistors on plastic substrates were also investigated (Figure 5-4b). A maximum sensitivity of ca. 1200 and responsivity of ca. 10 A/W were reached. The high value of the sensitivity, a clear improvement with respect to the value obtained with films on SiO_2 (8.5), is explained by the low values of the dark current. The responsivity increases by a factor of ca. 40 when V_g increases from 0 V to 1.1 V. Using a combination of low temperature thermal treatment (300 °C) and polyimide substrates constitutes an extremely promising route for the development of high performance low-voltage flexible phototransistors.

5.5 Conclusions

We fabricated ionic liquid-gated phototransistors capable of operating at about 1 V, based on sol-gel-deposited tungsten oxide films. The films were thermally treated at 300 °C, a temperature compatible with processing on plastic substrates, e.g. polyimide. Importantly, our films are persistent photoconductivity-free (persistent photoconductivity causes metal oxides to remain conductive for hours, even when light is switched off). Devices on polyimide substrates show high ON/OFF of 6×10^4 (500 on SiO_2) and phototransistor sensitivity of 1200 (8 on SiO_2), thus suggesting that the combined use of low temperature for film thermal treatment and plastic

substrates for film deposition represents a promising route towards high performance ionic liquid-gated metal oxide phototransistors.

We are now in the process of fabricating patterned phototransistors[214] in a way to better understand fundamental aspects of their behavior. Work is in progress to couple our oxide films to ion gels, instead of ionic liquids, in a way to demonstrate quasi solid-state devices. Furthermore, with the aim of tailoring the absorption properties of the metal oxide channel material, we are pursuing approaches such as blending tungsten oxide with upconverting materials.[215]

5.6 Experimental Section

Materials. The chemicals used for the synthesis of the tungsten oxide, i.e. $Na_2WO_4 \cdot 2H_2O$, ethanol and the Dowex 50WX2 hydrogen form resin (100-200 mesh), were purchased from Sigma Aldrich. Poly (ethylene glycol) 200 (PEG 200) was purchased from Fluka. The water used for the synthesis was of deionized quality (Milli-Q Millipore, 18.2 MΩ·cm at 25 °C). The ionic liquid, 1-ethyl-3-methylimidazolium bis(trifluoromethylsulfonyl)imide ([EMIM][TFSI]) was purchased from IoLiTec, (purity > 99 %) and purified prior use under vacuum (ca 10^{-9} bar) at 80 °C overnight. The purified ionic liquid was stored in an N_2 glovebox (H_2O and O_2 ⩽7 ppm) for a maximum of one day before electrochemical or transistor measurements. Polyimide (PolyFLE™ XF-102) sheets were purchased from POLYONICS. The gate electrode consisted of carbon paper (Spectracorp 2050, 6 mm×3 mm) coated with 6 µL of high surface area carbon ink made of activated carbon powder (PICACTIF SUPERCAP BP10, Pica, 28 mg/mL) and polyvinylidene fluoride (PVDF, KYNAR HSV900, 1.4 mg/mL) binder in the solvent N-methyl pyrrolidone (NMP, Fluka, > 99.0%). The specific capacitance of the activated carbon gate (surface area 1000–2000 m^2g^{-1}) was ca 0.1 F/m^2.[216]

Microfabrication. At first, SiO_2/Si and polyimide substrates were cleaned by sequential sonication in acetone, isopropyl alcohol (IPA) and deionized (DI) water (10 min for each step) and then dried using nitrogen flow. The polyimide substrates were laminated on glass slides with PDMS as adhesion layer, to ensure their flatness and rigidity during the following lithography steps. Both SiO_2/Si and polyimide substrates were pre-patterned by photolithography with coplanar Ti/Au (5 nm /40 nm) source and drain electrodes (channel width, *W*, 4000 µm and length, *L*, 10 µm). Prior to deposition of the tungsten oxide precursor, the substrates were wet-cleaned again by sequential

ultrasonic baths in IPA, acetone and IPA, followed by N_2 drying and UV-ozone exposure, for 15 minutes.

Sol-gel synthesis and film deposition. Tungsten oxide films were prepared from a tungstic acid precursor via a sol-gel method reported in the literature.[131] The films were deposited by gently spreading the tungstic acid-based sol, stabilized using PEG 200, on the patterned substrates. The films were first dried at room temperature for 10 min, then thermally treated at 300 °C or 550 °C (as specified below), in 80 sccm of O_2. Each thermal treatment lasted for 2 hours for 300 °C and 30 minutes for 550 °C. The number of sequential applications of the tungstic acid sol on the substrate (each application being followed by a thermal treatment) established the final thickness of the films. Films were prepared with 1 to 5 sequential applications, as specified below.

Assembly of the electrolyte-gated transistors. A Durapore GVHP membrane filter (4 mm × 9 mm = 0.36 mm^2) soaked in the ionic liquid was placed on top of the tungsten oxide film constituting the transistor channel. Afterwards, the activated carbon paper gate electrode was placed beside the channel (the distance between the gate electrode and the channel was ca. 0.5 mm).

Characterizations. A Dektak 150 Profilometer was used to measure the thickness of the films. The film thickness depends on the number of applications of the sol and the temperature of the thermal treatment. On the SiO_2 substrate, the thickness was 483 ± 47 nm for *thick* films (five applications) treated at 550 °C and 120 ± 26 nm for *thin* films (one application), treated at 300 °C. On polyimide, the thickness was 153 ± 25 nm for *thin* films (one application), treated at 300 °C. Scanning electron microscopy (SEM) was performed with a JEOL JSM7600F Microscope, in secondary electron mode, at an operating voltage of 10 kV. Atomic force microscopy (AFM) images were acquired in ambient conditions, in tapping mode, with a Digital Instruments Dimension 3100 (Santa Barbara, CA) combined with a Veeco Nanoscope V controller (Bruker). Tapping mode was performed at a scan rate of 1 Hz using etched silicon cantilevers (ACTA from Applied Nanostructures, Inc.) with a resonance frequency around 300 kHz, a spring constant of 40 N/m and tip radius <10 nm. All images were acquired with medium tip oscillation damping (20%–30%). X-ray diffraction (XRD) was performed by a Bruker D8 system with Cu Kα1 and Cu Kα2 sources. A Perkin Elmer LAMBDA 1050 spectrophotometer equipped with an integrating sphere was used to obtain the UV-visible spectra of tungsten oxide films deposited on quartz. The total transmittance (*T*) was measured by placing the film at the entrance of the sphere at normal

incidence whereas the film was placed at the back of the sphere for measurements of the total reflectance (*R*) at 8 degrees in conjunction with a light trap to eliminate the transmitted component. The absorptance (*A*) was obtained from A = 1 - *T* - *R*. The values of the optical penetration depths (1/α) of our tungsten oxide films were deduced from the knowledge of the optical absorption coefficient, α, from the approximate relation, α = [l/*t*] ln[(1-R)/T], where *t* is the film thickness. The values of the optical penetration depth were about 7.5 μm at λ = 500 nm and 0.85 μm at λ = 400 nm for films treated at 550 °C whereas the values were of 7.2 μm at λ = 480 nm and 1.2 μm at λ = 400 nm for films treated at 300 °C. The electrochemical tests were performed using a PARSTAT 2273 (Princeton Applied Research) multichannel potentiostat in an N_2 glovebox (H_2O and $O_2 \leqslant 7$ ppm). The optoelectronic characterizations were conducted by using a probe station connected to a semiconductor parameter analyzer (Agilent B1500A), at room temperature, in vacuum (ca 10^{-6} bar) or ambient conditions. The measurements of the current under illumination started after the films were illuminated for 2 minutes, to stabilize the current. A solar light simulator (ORIEL® VERASOL-2 solar simulator) was used as the source of illumination. The illumination conditions were the following: 1 kW/m^2 AM1.5G simulated irradiance covering the wavelength range of 390 nm to 1100 nm. For the determination of the responsivity of the films, the power was calculated considering the wavelength range of the film absorptance (see Figure S1), considering the certified spectral characteristics of the light simulator provided by the company. For *thin* films, treated at 300 °C, absorbing within the range λ = 390–440 nm, the value of the power density we used in the calculations was 0.08 kW/m^2.

5.7 Acknowledgements

The authors are grateful to Dr. I. Valitova for fruitful discussions and to Y. Drolet and F. Boutet for technical support. X. M. acknowledges financial support from the China Scholarship Council and CMC Microsystems (MNT program). C. S. is grateful to NSERC (DG) and Québec MESI for financial support. M. S. B. is grateful to FAPESP for financial support (grants #2016/09033-7 and 2015/50526-4).

CHAPTER 6 GENERAL DISCUSSION

In this chapter, we try to discuss the elements presented in the previous chapters as a whole, including the thesis objectives, the literature presented in Chapter 2 and the results presented in Chapter 4 and 5. The work reported in this thesis, focusing on the design, fabrication and characterization of electrolyte-gated tungsten oxide transistors, provided for a number of insights. These insights are discussed in terms of the nature of 1) the electrolyte-gating process in transistors based on nanostructured films interfaced to ionic liquids, the effect of 2) the temperature of the thermal treatment of the films and 3) the nature of the film substrate (conventional SiO_2 vs plastic) in establishing the optoelectronic characteristics of the (photo)transistors.

Considerable progress has been made by the research community in the fundamentals and practical applications of electrolyte-gated transistors with ionic liquid gate media. The high charge carrier density accumulated at the semiconductor/electrolyte interface opens opportunities for exploring phenomena such as insulator-metal transitions, superconductivity, ferromagnetism, ferroelectricity and chemical reactions, and enables the development of low-voltage, flexible devices. To help the critical evaluation of our results with respect to the rest of the scientific community, we prepared Table 6-1, where we show device fabrication and performance for ionic liquid-gated tungsten oxide transistors. In the literature, WO_3 films were typically deposited based on vapor-phase techniques, such as pulsed laser deposition (PLD) and radio frequency-magnetron sputtering (RF sputtering). In Article 1 and 2 of the thesis, our WO_3 films were solution processed via sol-gel synthesis and deposited by drop-cast. We therefore lower the device fabrication costs but also expanded application potential to large-area, flexible and printable electronics.

The operation voltages of transistors reported in the literature are typically 2-3 V and the ON/OFF ratios were as high as 10^3-10^6 for single crystal films and 10-300 for polycrystalline films. In Article 1 we demonstrated 1 V transistors with ON/OFF ratio of ca 10^2, comparable with values reported for polycrystalline films. The low operation voltage is enabled by the high charge carrier density achieved in the channel after electrolyte gating. It is worth noticing that accurate determination of the accumulated charge carrier density in electrolyte-gated transistors is nontrivial. Several approaches have been used in the literature. Hall effect measurement is the most direct way to estimate mobile charge carrier density and mobility in the electrolyte-gated transistors.[101] However, this approach is only suitable for systems with relatively high carrier

mobility. For most organic semiconductors or some inorganic semiconductors that only possess a low or modest value of carrier mobility this method is not applicable.[217] Another way to quantify the charge carrier density is by integrating the dielectric specific capacitance, C along the applied gate voltage, V sweep, $p = (\int C\, dV)/e$, where C is measured both as a function of the applied gate voltage and the appropriate frequency of the device operation. Integrating I_{gs} vs time during the linear transfer scan was also reported ($p = Q/eS = [\int (I_{gs}\, dV_g)]/[(dV_g/dt)eS]$, where Q is the doping charge and S is the surface area of semiconductor in contact with electrolyte).[106, 177] The charge carrier density value obtained through this method is similar to the values obtained by the abovementioned direct capacitance measurement at low frequency since I_{gs} measurement is a quasi-static DC measurement.

The charge carrier density values showed in Table 6-1 were mostly obtained from Hall measurements. However, due to the relatively low electron mobility of polycrystalline or amorphous nature of our tungsten oxides, we used the I_{gs} vs time approach to evaluate the charge carrier density, in Article 1 and 2. The values of *S* for the polycrystalline mesoporous and amorphous nonporous films were deduced based on the Brunauer-Emmett-Teller (BET) analysis and geometry surface area, respectively.[205, 214] Specific surface area deduced from the BET analysis likely leads to the overestimation of the surface area, given that the oxide in the film could aggregate in different manners with respect to the powders used for the BET analysis.[218] This could partially explain the two orders of magnitude lower charge carrier density in our films with respect to literatures. The other important figures of merit of an ionic liquid-gated WO_3 transistor, mobility (μ), was not systematically discussed in the literature. As discussed above, Hall effect measurement is the most direct way to estimate μ. μ can also be calculated from the standard field-effect transistor equation when devices work in electrostatic mode. Several works calculated μ from Ohm's law as $\mu = j_{ds}/(Eep) = (I_{ds}/ep)\,(L/W)\,V_{ds}$ for electrochemical transistors.[106, 177] In Article 1, according to Ohm's law, μ of our WO_3 was on the order of 10^{-2} $cm^2/V{\cdot}s$, which is comparable with the reported values for PLD polycrystalline oxides.

Overall, the studies presented in Article 1 of solution processed, ionic liquid-gated polycrystalline WO_3 transistors established outstanding thin film transistor performance, along with the operation voltages of 1 V, charge carrier densities larger than 10^{14} cm^{-2} and mobilities larger than 10^{-2} $cm^2/V{\cdot}s$, competitive with vapor phase-deposited devices. These results emphasize the potential of

solution-processed metal oxide transistors for future scientific and technological advances. Systematic investigation of ionic liquid-gated amorphous WO_3 transistors has not been reported.

Table 6-1 Comparison of the device performance of ionic liquid-gated WO_3 transistors.

WO_3 structure	Single crystal (Ref. 219, 220)	Single crystal (Ref. 221)	Single crystal (Ref. 167)	Single crystal (Ref. 222)	Polycrystalline (Ref. 223)	Single crystal (Ref. 224)
Film preparation	PLD, 750 °C	PLD, 600 °C	RF sputtering	RF sputtering	PLD	PLD
Substrate	$LaAlO_3$, Al_2O_3	$YAlO_3$	yttria stabilized zirconia	$YAlO_3$	$SrTiO_3$	$LaAlO_3$
Ionic liquid*	[HMIM]	[DEME]	[DEME]	[DEME]	[EMIM]	[DEME]
Operation Voltage	-3 V/- 3 V	-2 V/- 2 V	2 V	-2 V/- 2 V	-2 V/- 2 V	4.5 V
ON/OFF ratio	10^6	10^3	10^5	10^5	10 - 300	10^4
p	$5 \cdot 10^{21}$ (/cm^3)	$3.4 \cdot 10^{22}$ (/cm^3)	$1 \cdot 10^{16}$ (/cm^2)	$4.4 \cdot 10^{21}$ (/cm^3)	–	$1.5 \cdot 10^{22}$ (/cm^3) $3 \cdot 10^{16}$ (/cm^2)
μ (cm2/V·s)	–	–	–	1	10^{-3} - 10^{-1}	–
Working mechanism	Oxygen vacancy	Electrostatic	Electrostatic	Proton intercalation	Oxygen vacancy	Proton intercalation

* The anion of all ionic liquids is [TFSI]

Indeed, electrostatic doping dominates the working mechanism for most of the metal oxides electrolyte-gated transistors reported in literature.[76, 115] In contrast, despite the large size of the ions of ionic liquids, our nanostructured tungsten oxide electrolyte-gated transistors showed a clear electrochemical (faradic) contribution to the doping. This was supported by the cyclic voltammograms in Article 1. Thus, Article 1 revealed that, besides electrostatic doping, a combination of conventional electrochemical doping (injected electrons compensated by the insertion of protons from water traces) and nonconventional interface-confined electrochemical doping (injected electrons compensated by the cations of the ionic liquid packing at the interface) exists in nanostructured mesoporous tungsten oxide films.

It is known that tungsten oxides undergo structural transitions during small alkali ions (Li^+, Na^+) intercalation.[44, 172] Surprisingly, in Article 1 we also observed a monoclinic to orthorhombic transition during gate biasing. An orthorhombic to cubic phase transformation was observed by Parkin et al. on their single crystal WO_3 film. They suggested that the electric field-induced oxygen-vacancy formation is at the origin of the phase transformation in their electrolyte-gated tungsten oxide.[219, 220, 130] As discussed in Article 1, in situ structural and surface characterization are planned to investigate the effect of the electrical bias on the properties of our nanostructured WO_3 to shed light on the oxygen vacancy formation as a significant contribution to doping.

In Article 2, initially we performed the electrolyte-gated transistors characterization on polycrystalline and amorphous tungsten oxide films on SiO_2 substrates. The results demonstrated that film morphology and structure have an important effect on the performance of electrolyte-gated transistors, in particular in terms of ON/OFF ratio (amorphous films showed higher ON/OFF ratios). Low temperature (300 °C) of thermal treatment permit the development of flexible electronics applications. WO_3 electrolyte-gated transistors on polyimide substrates were shown in Article 2. Considering the advantages of electrolyte-gated transistors, which include large capacitances, high charge carrier density and low operation voltages, a variety of fundamental properties and applications have been reported.[76, 101] However, their applications in optoelectronics is still at its infancy. Article 2 revealed that the films treated at 300 °C, a temperature compatible with the use of polyimide plastic substrates, are persistent photoconductivity-free. Persistent photoconductivity causes metal oxides to remain conductive for hours, even when light is switched off.[193, 198] Since low temperature films do not show persistent photoconductivity they are interesting candidates for phototransistor applications. Moreover, the high density of charge carrier

accumulated by electrolyte-gating enables the improvement of the phototransistor responsivity, i.e. $(I_{ds} - I_{ds,\,dark})/P{\cdot}s$, where P is the power density of the incident light and s is the geometric area of the channel. Indeed, upon application of V_g, the large amount of charge carriers accumulated by gate voltage will shift the tungsten oxide Fermi level towards the conduction band and traps will be filled. This decreases the possibility of charge carrier trapping and improves the responsivity.

CHAPTER 7 CONCLUSION AND RECOMMENDATIONS

If we try to summarize, in this thesis, we achieved the following goals:

- we improved the current understanding of the doping process in nanostructured metal oxides interfaced to ionic liquids.
- we investigated the effect of the film structure and morphology in establishing the transistor performance,
- we fabricated tungsten oxide electrolyte-gated phototransistors on rigid and flexible substrates, operating at about 1 V.

We fabricated solution-processed tungsten oxide electrolyte-gated transistors operating at voltages as low as 1.0 V with charge carrier density larger than 10^{14} cm^{-2}, making use of high surface area activated carbon as the gate electrode and ionic liquids as the gating media. We propose a correlation between the cyclic voltammetry behavior of the channel material, structural changes observed by X-ray Diffraction in the material upon application of an electrical bias, and transistor transfer characteristics, anomalously shaped. We hypothesized that the working mechanism is based on the combination of electrostatic doping, electrochemical doping, with electron injection and proton insertion, and nonconventional electrochemical doping confined at the interface between the electrolyte and the high surface area metal oxide film.

Furthermore, we fabricated ionic liquid-gated phototransistors based on tungsten oxide films. The films were thermally treated at 300 °C, a temperature compatible with processing on plastic substrates, such as polyimide. Importantly, our films were persistent photoconductivity-free. Devices on polyimide substrates showed high ON/OFF of 6×10^4 (500 on SiO_2) and phototransistor sensitivity of 1200 (8 on SiO_2), thus suggesting that the combined use of low temperature for film thermal treatment and plastic substrates for film deposition represents a promising route towards high performance ionic liquid-gated metal oxide phototransistors.

In order to thoroughly understand interfacial and bulk doping processes, it would be useful to investigate the structural changes taking place in tungsten oxide transistors gated with ionic liquids in situ during the application of the electrical bias by X-ray Photoelectron Spectroscopy (XPS) and X-ray Diffraction. The XPS characterization of the film surface of our nanostructured tungsten oxide in situ is expected to help to shed light on the oxygen vacancy formation upon application of an electrical bias. We are presently performing in situ Atomic Force Spectroscopy to characterize the structure of the electric double layer forming at the electrolyte/metal oxide interface in

electrolyte-gated transistors, during device operation (in operando), in collaboration with Oak Ridge National Lab (Dr. N. Balke).

Future work on the electrical properties of our electrolyte-gated transistors would aim at the exploration of the metallization behavior of tungsten oxide films, which is attractive for transparent conducting oxides with potential applications in displays and touch screens.

Since tungsten oxide shows electrochromic properties upon intercalation of small alkali ions and protons, a further avenue of research put forth by this thesis is the development of electrochromic transistors for smart windows applications. For this purpose, it is necessary to introduce alkali ions or protons to the electrolyte.

Fabrication of patterned phototransistors will be a way to better understand fundamental aspects of their behavior.[214] With the aim of tailoring the absorption properties of the metal oxide channel material, blending tungsten oxide with other materials, e.g. upconverting materials, is expected.[215]

BIBLIOGRAPHY

1. B. M. Leiner, V. G. Cerf, D. D. Clark, R. E. Kahn, L. Kleinrock, D. C. Lynch, J. Postel, L. G. Roberts and S. Wolff, ACM SIGCOMM Computer Communication Review **39** (5), 22-31 (2009).
2. J. E. Lilienfeld, "Method and apparatus for controlling electric currents," United States Patent, 1930.
3. F. P. McCluskey, T. Podlesak and R. Grzybowski, *High temperature electronics*. (CRC press, 1996).
4. P. Roggwiller, *Semiconductor devices for power conditioning*. (Springer Science & Business Media, Baden, 2012).
5. "The Nobel Prize in Physics 1956". Nobelprize.org. Nobel Media AB. Retrieved December 7, 2014.
6. D. Kahng, "Electric field controlled semiconductor device," United States Patent, 1963.
7. D. Neamen, *Semiconductor physics and devices*. (McGraw-Hill, Inc., New York, 2002).
8. A. Nathan, A. Ahnood, M. T. Cole, S. Lee, Y. Suzuki, P. Hiralal, F. Bonaccorso, T. Hasan, L. Garcia-Gancedo and A. Dyadyusha, Proceedings of the IEEE **100** (Special Centennial Issue), 1486-1517 (2012).
9. M. Stoppa and A. Chiolerio, Sensors **14** (7), 11957-11992 (2014).
10. J. Li, C. Zhang, L. Duan, L. M. Zhang, L. D. Wang, G. F. Dong and Z. L. Wang, Advanced Materials **28** (1), 106-110 (2016).
11. G. Crawford, *Flexible flat panel displays*. (Wiley, Chichester, 2005).
12. N. Saito, T. Ueda, K. Miura, S. Nakano, T. Sakano, Y. Maeda, H. Yamaguchi and I. Amemiya, In SID Symposium Digest of Technical Papers, 443-446, Blackwell Publishing Ltd, 2013.
13. D.-H. Kim, J. Viventi, J. J. Amsden, J. Xiao, L. Vigeland, Y.-S. Kim, J. A. Blanco, B. Panilaitis, E. S. Frechette and D. Contreras, Nature Materials **9** (6), 511-517 (2010).
14. T. Someya, T. Sekitani, S. Iba, Y. Kato, H. Kawaguchi and T. Sakurai, Proceedings of the National Academy of Sciences of the United States of America **101** (27), 9966-9970 (2004).
15. J. Ge, L. Sun, F. R. Zhang, Y. Zhang, L. A. Shi, H. Y. Zhao, H. W. Zhu, H. L. Jiang and S. H. Yu, Advanced Materials **28** (4), 783-783 (2016).
16. C. Auth, C. Allen, A. Blattner, D. Bergstrom, M. Brazier, M. Bost, M. Buehler, V. Chikarmane, T. Ghani and T. Glassman, In VLSI technology (VLSIT), 2012 symposium on, 131-132, IEEE (2012).
17. J. S. Park, W.-J. Maeng, H.-S. Kim and J.-S. Park, Thin Solid Films **520** (6), 1679-1693 (2012).
18. S. M. Sze, *Semiconductor devices: physics and technology*. (Wiley, 2008).

19. E. H. Nicollian and J. R. Brews, *MOS (metal oxide semiconductor) physics and technology*. (Wiley, New York, 1982).

20. D. A. Neamen, *Semiconductor physics and devices*. (McGraw-Hill, Inc, New York, 2002).

21. P. K. Weimer, Proceedings of the IRE **50** (6), 1462-1469 (1962).

22. J. Kanicki, *Amorphous and Microcrystalline Semiconductor Devices: Materials and Device Physics*. (Artech House Publishers, Norwood, 1992).

23. T. P. Brody, IEEE Transactions on Electron Devices **31** (11), 1614-1628 (1984).

24. K. Nomura, H. Ohta, A. Takagi, T. Kamiya, M. Hirano and H. Hosono, Nature **432** (7016), 488-492 (2004).

25. E. Fortunato, P. Barquinha and R. Martins, Advanced Materials **24** (22), 2945-2986 (2012).

26. C. D. Dimitrakopoulos and D. J. Mascaro, IBM Journal of research and development **45** (1), 11-27 (2001).

27. B. Kumar, B. K. Kaushik and Y. S. Negi, Polymer Reviews **54** (1), 33-111 (2014).

28. D. Khodagholy, T. Doublet, P. Quilichini, M. Gurfinkel, P. Leleux, A. Ghestem, E. Ismailova, T. Hervé, S. Sanaur and C. Bernard, Nature Communications **4**, 1575 (2013).

29. R. R. Harrison and C. Charles, IEEE Journal of Solid-State Circuits **38** (6), 958-965 (2003).

30. Y. C. Lai, B. W. Ye, C. F. Lu, C. T. Chen, M. H. Jao, W. F. Su, W. Y. Hung, T. Y. Lin and Y. F. Chen, Advanced Functional Materials **26**, 1286 (2016).

31. D. Son, J. Lee, S. Qiao, R. Ghaffari, J. Kim, J. E. Lee, C. Song, S. J. Kim, D. J. Lee and S. W. Jun, Nature Nanotechnology **9** (5), 397-404 (2014).

32. T. Song, W. Rim, J. Jung, G. Yang, J. Park, S. Park, Y. Kim, K.-H. Baek, S. Baek and S.-K. Oh, IEEE Journal of Solid-State Circuits **50** (1), 158-169 (2015).

33. H.-Y. Chang, S. Yang, J. Lee, L. Tao, W.-S. Hwang, D. Jena, N. Lu and D. Akinwande, ACS nano **7** (6), 5446-5452 (2013).

34. J. Veres, S. D. Ogier, S. W. Leeming, D. C. Cupertino and S. Mohialdin Khaffaf, Advanced Functional Materials **13** (3), 199-204 (2003).

35. F. Cicoira, M. Sessolo, O. Yaghmazadeh, J. A. DeFranco, S. Y. Yang and G. G. Malliaras, Advanced Materials **22** (9), 1012-1016 (2010).

36. S. H. Kim, K. Hong, W. Xie, K. H. Lee, S. Zhang, T. P. Lodge and C. D. Frisbie, Advanced Materials **25** (13), 1822-1846 (2013).

37. J. Jeong, N. Aetukuri, T. Graf, T. D. Schladt, M. G. Samant and S. S. Parkin, Science **339** (6126), 1402-1405 (2013).

38. S. Deb, Solar Energy Materials and Solar Cells **25** (3-4), 327-338 (1992).

39. S. H. Lee, R. Deshpande, P. A. Parilla, K. M. Jones, B. To, A. H. Mahan and A. C. Dillon, Advanced Materials **18** (6), 763-766 (2006).

40. X.-L. Li, T.-J. Lou, X.-M. Sun and Y.-D. Li, Inorganic chemistry **43** (17), 5442-5449 (2004).

41. K. Huang, Q. Zhang, F. Yang and D. He, Nano Research **3** (4), 281-287 (2010).

42. T. Kamiya and H. Hosono, NPG Asia Materials **2** (1), 15-22 (2010).

43. T. Kamiya, K. Nomura and H. Hosono, Journal of display Technology **5** (7), 273-288 (2009).

44. C. G. Granqvist, *Handbook of inorganic electrochromic materials*. (Elsevier, 1995).

45. H. Zheng, J. Z. Ou, M. S. Strano, R. B. Kaner, A. Mitchell and K. Kalantar‐zadeh, Advanced Functional Materials **21** (12), 2175-2196 (2011).

46. R. Diehl, G. Brandt and E. Salje, Acta Crystallographica Section B: Structural Crystallography and Crystal Chemistry **34** (4), 1105-1111 (1978).

47. E. Salje and K. Viswanathan, Acta Crystallographica Section A: Crystal Physics, Diffraction, Theoretical and General Crystallography **31** (3), 356-359 (1975).

48. B. Gerand, G. Nowogrocki, J. Guenot and M. Figlarz, Journal of Solid State Chemistry **29** (3), 429-434 (1979).

49. H. Zeller and H. Beyeler, Applied Physics **13** (3), 231-237 (1977).

50. J. Gabrusenoks, P. Cikmach, A. Lusis, J. Kleperis and G. Ramans, Solid State Ionics **14** (1), 25-30 (1984).

51. A. Nakamura and S. Yamada, Applied Physics A: Materials Science & Processing **24** (1), 55-59 (1981).

52. P. Roussel, P. Labbe and D. Groult, Acta Crystallographica Section B: Structural Science **56** (3), 377-391 (2000).

53. A. Hjelm, C. G. Granqvist and J. M. Wills, Physical Review B **54** (4), 2436 (1996).

54. M. S. Hybertsen and S. G. Louie, Matter Phys **13** (5) (1987).

55. M. Gillet, K. Aguir, C. Lemire, E. Gillet and K. Schierbaum, Thin Solid Films **467** (1), 239-246 (2004).

56. J. M. Berak and M. Sienko, Journal of Solid State Chemistry **2** (1), 109-133 (1970).

57. V. Makarov and M. Trontelj, Journal of the European Ceramic Society **16** (7), 791-794 (1996).

58. R. Vemuri, K. K. Bharathi, S. Gullapalli and C. Ramana, ACS applied materials & interfaces **2** (9), 2623-2628 (2010).

59. S. Gullapalli, R. Vemuri and C. Ramana, Applied Physics Letters **96** (17), 171903 (2010).

60. H. Hersh, W. Kramer and J. McGee, Applied Physics Letters **27** (12), 646-648 (1975).

61. B. W. Faughnan, R. S. Crandall and P. M. Heyman, Rca Review **36** (1), 177-197 (1975).

62. S. Deb, Appl Opt **58** (3), 190 (1969).

63. R. Schöllhorn, Angewandte Chemie International Edition in English **19** (12), 983-1003 (1980).

64. C. Granqvist, Solar Energy Materials and Solar Cells **32** (4), 369-382 (1994).

65. C. G. Granqvist, Solar Energy Materials and Solar Cells **60** (3), 201-262 (2000).
66. R. S. Crandall and B. W. Faughnan, Applied Physics Letters **26** (3), 120-121 (1975).
67. J. L. Ord, Journal of the Electrochemical Society **129** (4), 767-771 (1982).
68. J. Ord and D. De Smet, Journal of he Electrochemical Society **139** (2), 359-363 (1992).
69. S. K. Deb, Solar Energy Materials and Solar Cells **92** (2), 245-258 (2008).
70. H. v. Helmholtz, Annalen der Physik **165** (6), 211-233 (1853).
71. M. Gouy, J. Phys. Theor. Appl. **9** (1), 457-468 (1910).
72. D. L. Chapman, The London, Edinburgh, and Dublin philosophical magazine and journal of science **25** (148), 475-481 (1913).
73. O. Stern, Berichte der Bunsengesellschaft für physikalische Chemie **30** (21‐22), 508-516 (1924).
74. P. Debye and E. Hückel, Physikalische Zeitschrift **24** (9), 185-206 (1923).
75. H. Li, T. Carstens, A. Elbourne, N. Borisenko, R. Gustus, F. Endres and R. Atkin, Electrodeposition from Ionic Liquids, 321-343 (2017).
76. T. Fujimoto and K. Awaga, Physical Chemistry Chemical Physics **15** (23), 8983-9006 (2013).
77. R. Atkin, S. Z. El Abedin, R. Hayes, L. H. Gasparotto, N. Borisenko and F. Endres, The Journal of Physical Chemistry C **113** (30), 13266-13272 (2009).
78. R. Hayes, N. Borisenko, M. K. Tam, P. C. Howlett, F. Endres and R. Atkin, The Journal of Physical Chemistry C **115** (14), 6855-6863 (2011).
79. R. Atkin, N. Borisenko, M. Drüschler, S. Z. El Abedin, F. Endres, R. Hayes, B. Huber and B. Roling, Physical Chemistry Chemical Physics **13** (15), 6849-6857 (2011).
80. H. Zhou, M. Rouha, G. Feng, S. S. Lee, H. Docherty, P. Fenter, P. T. Cummings, P. F. Fulvio, S. Dai and J. McDonough, ACS nano **6** (11), 9818-9827 (2012).
81. S. Thiemann, S. Sachnov, S. Porscha, P. Wasserscheid and J. Zaumseil, The Journal of Physical Chemistry C **116** (25), 13536-13544 (2012).
82. V. Lockett, R. Sedev, J. Ralston, M. Horne and T. Rodopoulos, The Journal of Physical Chemistry C **112** (19), 7486-7495 (2008).
83. T. Fujimoto, M. M. Matsushita and K. Awaga, The Journal of Physical Chemistry C **116** (8), 5240-5245 (2012).
84. S. Ono, K. Miwa, S. Seki and J. Takeya, Applied Physics Letters **94** (6), 39 (2009).
85. K. Ueno, S. Nakamura, H. Shimotani, A. Ohtomo, N. Kimura, T. Nojima, H. Aoki, Y. Iwasa and M. Kawasaki, Nature materials **7** (11), 855 (2008).
86. K. Ueno, S. Nakamura, H. Shimotani, A. Ohtomo, N. Kimura, T. Nojima, H. Aoki, Y. Iwasa and M. Kawasaki, Nature materials **7** (11), 855-858 (2008).
87. S. Asanuma, P.-H. Xiang, H. Yamada, H. Sato, I. Inoue, H. Akoh, A. Sawa, K. Ueno, H. Shimotani and H. Yuan, Applied Physics Letters **97** (14), 142110 (2010).

88. W. Xie, S. Wang, X. Zhang, C. Leighton and C. D. Frisbie, Physical review letters **113** (24), 246602 (2014).

89. D. A. Bernards and G. G. Malliaras, Advanced Functional Materials **17** (17), 3538-3544 (2007).

90. M. J. Panzer, C. R. Newman and C. D. Frisbie, Applied Physics Letters **86** (10), 103503 (2005).

91. S. W. Lee, H. J. Lee, J. H. Choi, W. G. Koh, J. M. Myoung, J. H. Hur, J. J. Park, J. H. Cho and U. Jeong, Nano letters **10** (1), 347-351 (2009).

92. H. Yuan, H. Shimotani, A. Tsukazaki, A. Ohtomo, M. Kawasaki and Y. Iwasa, Advanced Functional Materials **19** (7), 1046-1053 (2009).

93. J. Lee, M. J. Panzer, Y. He, T. P. Lodge and C. D. Frisbie, Journal of the American Chemical Society **129** (15), 4532-4533 (2007).

94. L. Kergoat, L. Herlogsson, D. Braga, B. Piro, M. C. Pham, X. Crispin, M. Berggren and G. Horowitz, Advanced Materials **22** (23), 2565-2569 (2010).

95. M. Armand, F. Endres, D. R. MacFarlane, H. Ohno and B. Scrosati, Nature materials **8** (8), 621-629 (2009).

96. N. V. Plechkova, R. D. Rogers and K. R. Seddon, *Ionic liquids: from knowledge to application*. (ACS Publications, Washington, 2010).

97. R. Misra, M. McCarthy and A. F. Hebard, Applied Physics Letters **90** (5), 052905 (2007).

98. S. Ono, S. Seki, R. Hirahara, Y. Tominari and J. Takeya, Applied Physics Letters **92** (10), 93 (2008).

99. D. Braga, I. Gutiérrez Lezama, H. Berger and A. F. Morpurgo, Nano letters **12** (10), 5218-5223 (2012).

100. F. Wang, P. Stepanov, M. Gray, C. N. Lau, M. E. Itkis and R. C. Haddon, Nano letters **15** (8), 5284-5288 (2015).

101. S. Z. Bisri, S. Shimizu, M. Nakano and Y. Iwasa, Advanced Materials 29 (25), 1607054 (2017).

102. W. Xie and C. D. Frisbie, The Journal of Physical Chemistry C **115** (29), 14360-14368 (2011).

103. Y. Xia, J. H. Cho, J. Lee, P. P. Ruden and C. D. Frisbie, Advanced Materials **21** (21), 2174-2179 (2009).

104. Y. Takeyama, S. Ono and Y. Matsumoto, Applied Physics Letters **101** (8), 083303 (2012).

105. J. H. Cho, J. Lee, Y. He, B. Kim, T. P. Lodge and C. D. Frisbie, Advanced Materials **20** (4), 686-690 (2008).

106. B. D. Paulsen and C. D. Frisbie, The Journal of Physical Chemistry C **116** (4), 3132-3141 (2012).

107. J. Sayago, X. Meng, F. Quenneville, S. Liang, É. Bourbeau, F. Soavi, F. Cicoira and C. Santato, Journal of Applied Physics **117** (11), 112809 (2015).

108. T. Fujimoto, Y. Miyoshi, M. M. Matsushita and K. Awaga, Chemical Communications **47** (20), 5837-5839 (2011).

109. S. Ono, N. Minder, Z. Chen, A. Facchetti and A. Morpurgo, Applied Physics Letters **97** (14), 220 (2010).

110. Y. Yomogida, J. Pu, H. Shimotani, S. Ono, S. Hotta, Y. Iwasa and T. Takenobu, Advanced Materials **24** (32), 4392-4397 (2012).

111. H. Okimoto, T. Takenobu, K. Yanagi, Y. Miyata, H. Shimotani, H. Kataura and Y. Iwasa, Advanced Materials **22** (36), 3981-3986 (2010).

112. B. J. Kim, H. Jang, S.-K. Lee, B. H. Hong, J.-H. Ahn and J. H. Cho, Nano letters **10** (9), 3464-3466 (2010).

113. Z. Chen, H. Yuan, Y. Zhang, K. Nomura, T. Gao, Y. Gao, H. Shimotani, Z. Liu and Y. Iwasa, Nano letters **12** (5), 2212-2216 (2012).

114. H. Yuan, H. Shimotani, A. Tsukazaki, A. Ohtomo, M. Kawasaki and Y. Iwasa, Journal of the American Chemical Society **132** (19), 6672-6678 (2010).

115. S. Thiemann, M. Gruber, I. Lokteva, J. Hirschmann, M. Halik and J. Zaumseil, ACS applied materials & interfaces **5** (5), 1656-1662 (2013).

116. W. Xie, X. Zhang, C. Leighton and C. D. Frisbie, Advanced Electronic Materials **3** (3) (2017).

117. Y. Tokura and N. Nagaosa, Science **288** (5465), 462-468 (2000).

118. M. Nakano, K. Shibuya, D. Okuyama, T. Hatano, S. Ono, M. Kawasaki, Y. Iwasa and Y. Tokura, Nature **487** (7408), 459 (2012).

119. C. Ahn, J.-M. Triscone and J. Mannhart, Nature **424** (6952), 1015-1018 (2003).

120. M. Ono, S. Koga and H. Ohtsuki, IEEE Instrumentation & Measurement Magazine **5** (1), 9-15 (2002).

121. Y. Lee, C. Clement, J. Hellerstedt, J. Kinney, L. Kinnischtzke, X. Leng, S. Snyder and A. Goldman, Physical review letters **106** (13), 136809 (2011).

122. J. Ye, S. Inoue, K. Kobayashi, Y. Kasahara, H. Yuan, H. Shimotani and Y. Iwasa, Nature materials **9** (2), 125-128 (2010).

123. Z. Yang, Y. Zhou and S. Ramanathan, Journal of Applied Physics **111** (1), 014506 (2012).

124. H. Yuan, H. Shimotani, J. Ye, S. Yoon, H. Aliah, A. Tsukazaki, M. Kawasaki and Y. Iwasa, Journal of the American Chemical Society **132** (51), 18402-18407 (2010).

125. X. Leng, A. Bollinger and I. Božović, Scientific reports **6**, 31239 (2016).

126. J. Karel, C. E. ViolBarbosa, J. Kiss, J. Jeong, N. Aetukuri, M. G. Samant, X. Kozina, E. Ikenaga, G. H. Fecher and C. Felser, ACS nano **8** (6), 5784-5789 (2014).

127. J. Jeong, N. B. Aetukuri, D. Passarello, S. D. Conradson, M. G. Samant and S. S. Parkin, Proceedings of the National Academy of Sciences **112** (4), 1013-1018 (2015).

128. D. Passarello, S. G. Altendorf, J. Jeong, C. Rettner, N. Arellano, T. Topuria, M. G. Samant and S. S. Parkin, Nano letters **17** (5), 2796-2801 (2017).

129. T. D. Schladt, T. Graf, N. B. Aetukuri, M. Li, A. Fantini, X. Jiang, M. G. Samant and S. S. Parkin, ACS nano **7** (9), 8074-8081 (2013).

130. S. G. Altendorf, J. Jeong, D. Passarello, N. B. Aetukuri, M. G. Samant and S. S. Parkin, Advanced Materials **28** (26), 5284-5292 (2016).

131. C. Santato, M. Odziemkowski, M. Ulmann and J. Augustynski, Journal of the American Chemical Society **123** (43), 10639-10649 (2001).

132. J. Lemerle and J. Lefebvre, Canadian Journal of Chemistry **55** (21), 3758-3762 (1977).

133. L. Herlogsson, Linköping University Electronic Press, 2011.

134. Data measured and provided by IoLiTec Ionic Liquids Technologies at 20 °C.

135. D. K. Gosser, Cyclic voltammetry: simulation and analysis of reaction mechanisms. (VCH, New York, 1993).

136. A. J. Bard, L. R. Faulkner, J. Leddy and C. G. Zoski, *Electrochemical methods: fundamentals and applications*. (Wiley, New York, 1980).

137. P. T. Kissinger and W. R. Heineman, J. Chem. Educ **60** (9), 702 (1983).

138. R. S. Nicholson, Analytical Chemistry **37** (11), 1351-1355 (1965).

139. P. Zanello, *Inorganic electrochemistry: theory, practice and applications*. (Royal Society of Chemistry, 2003).

140. M. E. Orazem and B. Tribollet, *Electrochemical impedance spectroscopy*. (Wiley, 2011).

141. J. R. Macdonald and W. B. Johnson, Fundamentals of impedance spectroscopy. *Impedance Spectroscopy: Theory, Experiment, and Applications.* (Wiley, Hoboken, 2005).

142. G. Binnig, C. F. Quate and C. Gerber, Physical Review Letters **56** (9), 930 (1986).

143. J. Chastain, R. C. King and J. Moulder, *Handbook of X-ray photoelectron spectroscopy: a reference book of standard spectra for identification and interpretation of XPS data*. (Physical Electronics Eden Prairie, Minnesota, 1995).

144. N. Colthup, *Introduction to infrared and Raman spectroscopy*. (Elsevier, New York, 2012).

145. P. Graves and D. Gardiner, *Practical Raman Spectroscopy*. (Springer, Cham, 1989).

146. E. Smith and G. Dent, *Modern Raman spectroscopy: a practical approach*. (Wiley, Chichester, 2013).

147. B. E. Warren, *X-ray Diffraction*. (Courier Corporation, New York, 1969).

148. A. Coats and J. Redfern, Analyst **88** (1053), 906-924 (1963).

149. G. Tarabella, F. M. Mohammadi, N. Coppedè, F. Barbero, S. Iannotta, C. Santato and F. Cicoira, Chemical Science **4** (4), 1395-1409 (2013).

150. K. Hong, S. H. Kim, K. H. Lee and C. D. Frisbie, Advanced Materials **25** (25), 3413-3418 (2013).

151. Y.-L. Han, Z.-Z. Luo, C.-J. Li, S.-C. Shen, G.-L. Qu, C.-M. Xiong, R.-F. Dou, L. He and J.-C. Nie, Physical Review B **90** (20), 205107 (2014).

152. C. Ahn, A. Bhattacharya, M. Di Ventra, J. Eckstein, C. D. Frisbie, M. Gershenson, A. Goldman, I. Inoue, J. Mannhart and A. J. Millis, Reviews of Modern Physics **78** (4), 1185 (2006).

153. Y. Zhou and S. Ramanathan, Critical Reviews in Solid State and Materials Sciences **38** (4), 286-317 (2013).

154. D. Khodagholy, J. Rivnay, M. Sessolo, M. Gurfinkel, P. Leleux, L. H. Jimison, E. Stavrinidou, T. Herve, S. Sanaur and R. M. Owens, Nature communications **4** (2133), (2013).

155. E. Fortunato, D. Ginley, H. Hosono and D. C. Paine, MRS Bulletin **32** (03), 242-247 (2007).

156. J. K. Jeong, Semiconductor Science and Technology **26** (3), 034008 (2011).

157. M. Grätzel, Nature **414** (6861), 338-344 (2001).

158. C. Yuan, H. B. Wu, Y. Xie and X. W. D. Lou, Angewandte Chemie International Edition **53** (6), 1488-1504 (2014).

159. Z. L. Wang, Advanced Materials **24** (34), 4632-4646 (2012).

160. M. M. Lee, J. Teuscher, T. Miyasaka, T. N. Murakami and H. J. Snaith, Science **338** (6107), 643-647 (2012).

161. H. Kanno, R. J. Holmes, Y. Sun, S. Kena‐Cohen and S. R. Forrest, Advanced Materials **18** (3), 339-342 (2006).

162. A. Ponzoni, E. Comini, G. Sberveglieri, J. Zhou, S. Z. Deng, N. S. Xu, Y. Ding and Z. L. Wang, Applied Physics Letters **88** (20), 203101 (2006).

163. S. H. Baeck, K. S. Choi, T. F. Jaramillo, G. D. Stucky and E. W. McFarland, Advanced Materials **15** (15), 1269-1273 (2003).

164. M. J. Natan, T. E. Mallouk and M. S. Wrighton, Journal of Physical Chemistry **91** (3), 648-654 (1987).

165. P. Barquinha, S. Pereira, L. Pereira, P. Wojcik, P. Grey, R. Martins and E. Fortunato, Advanced Electronic Materials **1** (5), 1500030 (2015).

166. S. Zhuiykov, E. Kats, B. Carey and S. Balendhran, Nanoscale **6** (24), 15029-15036 (2014).

167. P. M. Wu, S. Ishii, K. Tanabe, K. Munakata, R. Hammond, K. Tokiwa, T. Geballe and M. Beasley, Applied Physics Letters **106** (4), 042602 (2015).

168. J. Karel, C. Viol Barbosa, S. Altendorf, J. Kiss, Y. Utsumi, M. Samant, L. H. Tjeng, C. Felser and S. Parkin, presented at the APS March Meeting Abstracts, 2015 (unpublished).

169. J. Sayago, F. Soavi, Y. Sivalingam, F. Cicoira and C. Santato, Journal of Materials Chemistry C **2** (28), 5690-5694 (2014).

170. H. Tang, P. Kumar, S. Zhang, Z. Yi, G. D. Crescenzo, C. Santato, F. Soavi and F. Cicoira, ACS Applied Materials & Interfaces **7** (1), 969-973 (2014).

171. D. Weingarth, A. Foelske-Schmitz, A. Wokaun and R. Kötz, Electrochemistry Communications **18**, 116-118 (2012).

172. E. Cazzanelli, C. Vinegoni, G. Mariotto, A. Kuzmin and J. Purans, Solid State Ionics **123** (1), 67-74 (1999).

173. C. O. Laoire, E. Plichta, M. Hendrickson, S. Mukerjee and K. Abraham, Electrochimica Acta **54** (26), 6560-6564 (2009).

174. R. Roth and J. Waring, J. Res. Natl. Bur. Stand., Sect. A **70**, 281-303 (1966).

175. Theoretical calculations, assuming a spherical shape for the ions,[176] permitted to estimate the volume of the cations of the ionic liquids: 182 $Å^3$ for [EMIM] (leading to a radius of ca. 3.5 Å) and 253 $Å^3$ for [PYR_{14}] (radius ca. 3.9 Å).

176. M. N. Kobrak, Green Chemistry **10** (1), 80-86 (2008).

177. M. J. Panzer and C. D. Frisbie, Advanced Functional Materials **16** (8), 1051-1056 (2006).

178. The valence band and conduction band of WO_3 are located at ca. -7.2 eV and -4.6 eV vs. vacuum. The work function of Au is ca. -5 eV.[179]

179. W. Osikowicz, M. P. de Jong, S. Braun, C. Tengstedt, M. Fahlman and W. R. Salaneck, Applied Physics Letters **88** (19), 193504 (2006).

180. S. Tanisaki, Journal of the Physical Society of Japan **15** (4), 573-581 (1960).

181. L. Khandare, D. J. Late, Applied Surface Science **418**, 2-8 (2017).

182. K. K. Naik, R. Khare, D. Chakravarty, M. A. More, R. Thapa, D. J. Late, C. S. Rout, Applied Physics Letters **105** (23), 233101 (2014).

183. D. J. Late, R. V. Kashid, C. S. Rout, M. A. More, D. S. Joag, Applied Physics A, **98** (4), 751-756 (2010).

184. D. J. Late, P. Misra, B. Singh, L. M. Kukreja, D. S. Joag, M. A. More, Applied Physics A: Materials Science & Processing, **95** (2), 613-620 (2009).

185. A. B. Bhise, D. J. Late, P. S. Walke, M. A. More, V. K. Pillai, I. S. Mulla, D. S. Joag, Journal of Crystal Growth, **307** (1), 87-91 (2007).

186. N. S. Ramgir, D. J. Late, A. B. Bhise, M. A. More, I. S. Mulla, D. S. Joag, K. Vijayamohanan, The Journal of Physical Chemistry B, **110** (37), 18236-18242 (2006).

187. M. S. Pawar, P. K. Bankar, M. A. More, D. J. Late, RSC Advances, **5** (108), 88796-88804 (2015).

188. K. Nomura, H. Ohta, A. Takagi, T. Kamiya, M. Hirano, H. Hosono, Nature, **432** (7016), 488-492 (2004).

189. Y. H. Lin, H. Faber, K. Zhao, Q. Wang, A. Amassian, M. McLachlan, T. D. Anthopoulos, Advanced Materials, 25 (31), 4340-4346 (2013).

190. A. D. Mottram, Y.-H. Lin, P. Pattanasattayavong, K. Zhao, A. Amassian and T. D. Anthopoulos, ACS Applied Materials & Interfaces **8** (7), 4894-4902 (2016).

191. K. J. Baeg, M. Binda, D. Natali, M. Caironi and Y. Y. Noh, Advanced Materials **25** (31), 4267-4295 (2013).

192. H. C. Wu, Y. C. Huang, I. Ding, C. C. Chen, Y. H. Yang, C. C. Tsai, C. D. Chen and Y. T. Chen, Advanced Functional Materials **21** (3), 474-479 (2011).

193. E. Lhuillier, J.-F. Dayen, D. O. Thomas, A. Robin, B. Doudin and B. Dubertret, Nano Letters **15** (3), 1736-1742 (2015).

194. E. Lhuillier, A. Robin, S. Ithurria, H. Aubin and B. Dubertret, Nano Letters **14** (5), 2715-2719 (2014).

195. Y. Lee, J. Kwon, E. Hwang, C. H. Ra, W. J. Yoo, J. H. Ahn, J. H. Park and J. H. Cho, Advanced Materials **27** (1), 41-46 (2015).

196. F. Li, C. Ma, H. Wang, W. Hu, W. Yu, A. D. Sheikh and T. Wu, Nature Communications **6** (2015).

197. M. Buscema, J. O. Island, D. J. Groenendijk, S. I. Blanter, G. A. Steele, H. S. van der Zant and A. Castellanos-Gomez, Chemical Society Reviews **44** (11), 3691-3718 (2015).

198. O. Lopez-Sanchez, D. Lembke, M. Kayci, A. Radenovic and A. Kis, Nature Nanotechnology **8** (7), 497-501 (2013).

199. V. Q. Dang, T. Q. Trung, L. T. Duy, B.-Y. Kim, S. Siddiqui, W. Lee and N.-E. Lee, ACS Aapplied Mmaterials & Interfaces **7** (20), 11032-11040 (2015).

200. S. Knobelspies, A. Daus, G. Cantarella, L. Petti, N. Münzenrieder, G. Tröster and G. A. Salvatore, Advanced Electronic Materials **2** (10) (2016).

201. S. Mondal and A. Raychaudhuri, Applied Physics Letters **98** (2), 023501 (2011).

202. J. Brillet, J.-H. Yum, M. Cornuz, T. Hisatomi, R. Solarska, J. Augustynski, M. Graetzel and K. Sivula, Nature Photonics **6** (12), 824-828 (2012).

203. M. Epifani, T. Andreu, J. Arbiol, R. l. Díaz, P. Siciliano and J. R. Morante, Chemistry of Materials **21** (21), 5215-5221 (2009).

204. J. Zhao, E. Olide and F. E. Osterloh, Journal of the Electrochemical Society **162** (1), H65-H71 (2015).

205. X. Meng, F. Quenneville, F. d. r. Venne, E. Di Mauro, D. Işık, M. Barbosa, Y. Drolet, M. M. Natile, D. Rochefort and F. Soavi, The Journal of Physical Chemistry C **119** (37), 21732-21738 (2015).

206. S. Jeon, S.-E. Ahn, I. Song, C. J. Kim, U.-I. Chung, E. Lee, I. Yoo, A. Nathan, S. Lee and J. Robertson, Nature Materials **11** (4), 301-305 (2012).

207. A. Janotti, C. G. Van de Walle. Applied Physics Letters **87** (12), 122102 (2005).

208. S. Lany and A. Zunger, Physical Review B **72** (3), 035215 (2005).

209. K. Huang and Q. Zhang, Nanoscale Research Letters **6** (1), 52 (2010).

210. J. D. Prades, F. Hernandez-Ramirez, R. Jimenez-Diaz, M. Manzanares, T. Andreu, A. Cirera, A. Romano-Rodriguez and J. Morante, Nanotechnology **19** (46), 465501 (2008).

211. Y. Lin, D. Wang, Q. Zhao, Z. Li, Y. Ma, M. Yang, Nanotechnology, **17** (9), 2110-2115 (2006).

212. M. Lee, W. Lee, S. Choi, J. W. Jo, J. Kim, S. K. Park and Y. H. Kim, Advanced Materials 29 (28), 1700951 (2017).

213. K. K. Ng, *Complete Guide to Semiconductor Devices*. (Wiley, New York, 2002).

214. I. Valitova, P. Kumar, X. Meng, F. Soavi, C. Santato and F. Cicoira, ACS Applied Materials & Interfaces **8** (23), 14855-14862 (2016).

215. F. Venne, M. Quintanilla, F. Quenneville, D. Işik, B. Baloukas, F. Vetrone and C. Santato, RSC Advances **5** (100), 81875-81880 (2015).

216. M. Lazzari, C. Arbizzani, F. Soavi and M. Mastragostino, Supercapacitors: Materials, Systems, and Applications, 289-306 (2013).

217. F. Werner, Journal of Applied Physics **122** (13), 135306 (2017).

218. I. Valitova, M. M. Natile, F. Soavi, C. Santato, and F. Cicoira, ACS Applied Materials & Interfaces **9** (42), 37013-37021 (2017).

219. S. G. Altendorf, J. Jeong, D. Passarello, N. B. Aetukuri, M. G. Samant and S. S. Parkin, Advanced Materials, **28**(26), 5284-5292 (2016).

220. C. ViolBarbosa, J. Karel, J. Kiss, O.-d. Gordan, S. G. Altendorf, Y. Utsumi, M. G. Samant, Y.-H. Wu, K.-D. Tsuei and C. Felser, Proceedings of the National Academy of Sciences, **113** (40), 11148-11151 (2016).

221. S. Nishihaya, M. Uchida, Y. Kozuka, Y. Iwasa, M. Kawasaki, ACS Applied materials & Interfaces, **8**(34), 22330-22336 (2016).

222. X. Leng, J. Pereiro, J. Strle, A.T. Bollinger, G. Dubuis, A. Gozar, N. Litombe, D. Pavuna, and I. Bozovic, NPJ Quantum Materials, **2**, 35-41(2017).

223. H. Kalhori, M. Coey, I. A. Sarsari, K. Borisov, S. B. Porter, G. Atcheson, M. Ranjbar, H. Salamarti, P. Stamenov, Scientific Reports, **7**(1), 12253 (2017).

224. M. Wang, S. Shen, J. Ni, N. Lu, Z. Li, H. Li, S. Yang, T. Chen, J. Guo, Y. Wang, H. Xiang, P. Yu, Advanced Materials, 1703628 (2017).

APPENDIX A – SUPPORTING INFORMATION FOR ARTICLE 1

Electrolyte-Gated WO_3 Transistors: Electrochemistry, Structure and Device Performance

Xiang Meng,[1] Francis Quenneville,[1] Frédéric Venne,[1] Eduardo Di Mauro,[1] Dilek Işık,,[1] Martin Barbosa,[1,2] Yves Drolet,[1] Marta M. Natile,[3] Dominic Rochefort,[4] Francesca Soavi,[5] and Clara Santato[1,]*

1. Département de Génie Physique, Polytechnique Montréal, C.P. 6079, Succ. Centre Ville, H3C 3A7, Canada

2. Departamento de Físico-Química, Universidade Estadual Paulista, Rua Professor Degni, 55, Araraquara, 14800-060, Brazil

3. CNR-IENI, Dipartimento di Scienze Chimiche, Università di Padova, Via F. Marzolo 1, 35131, Italy

4. Département de Chimie, Université de Montréal, C.P. 6128, Succ. Centre Ville, H3C 3J7, Canada

5. Dipartimento di Chimica "Giacomo Ciamician", Università di Bologna, Via Selmi, 2, 40126, Italy

*Corresponding author

E-mail: clara.santato@polymtl.ca

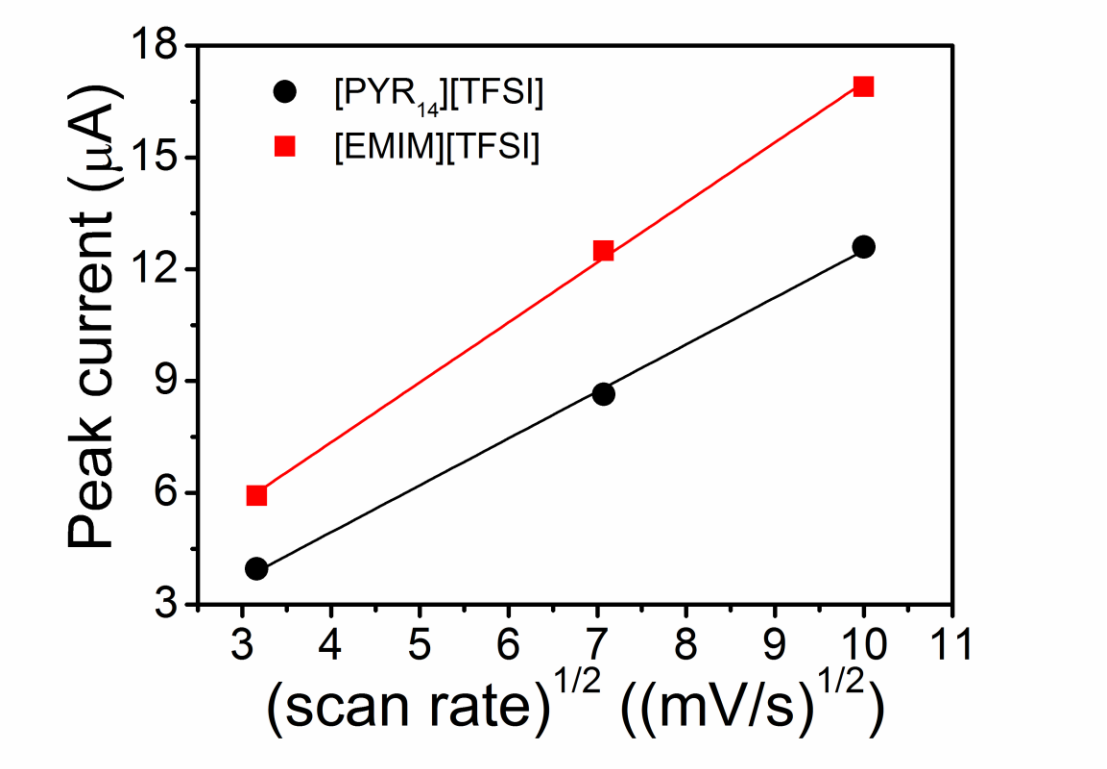

Figure S1. Dependence of the current of the anodic peak (located at about 0.2 V) on the square root of the potential scan rate for WO_3 transistors gated with [EMIM][TFSI] (red square) and [PYR_{14}][TFSI] (black circle).

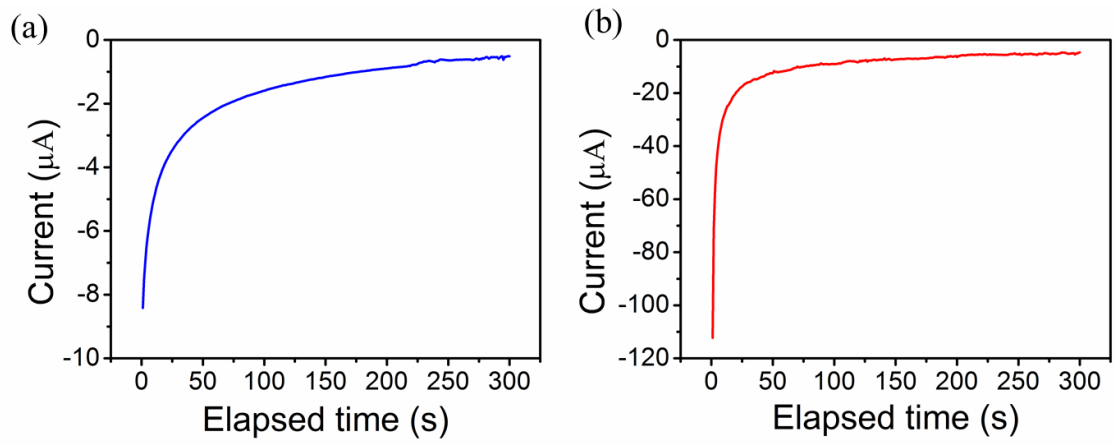

Figure S2. Chronoamperometry curves of WO_3 thin films-on-ITO in [EMIM][TFSI] biased at -0.6 V (a) and -1 V (b). The amount of doping charge is -0.48 mC and -3 mC for (a) and (b), respectively, as obtained by integrating the current over the biasing time.

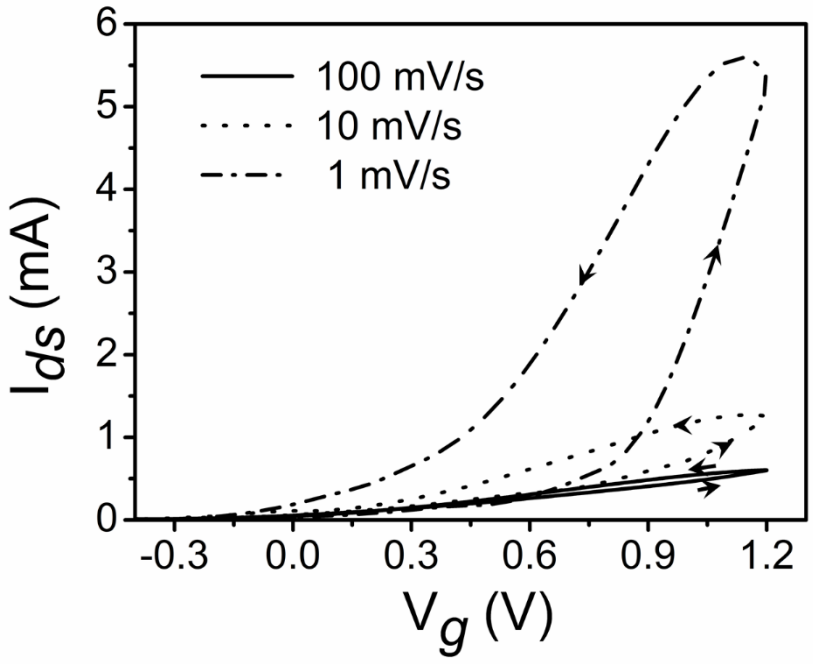

Figure S3. Transfer characteristics of [EMIM][TFSI]-gated WO_3 transistors at V_{ds} = 1 V, at different V_g scan rates.

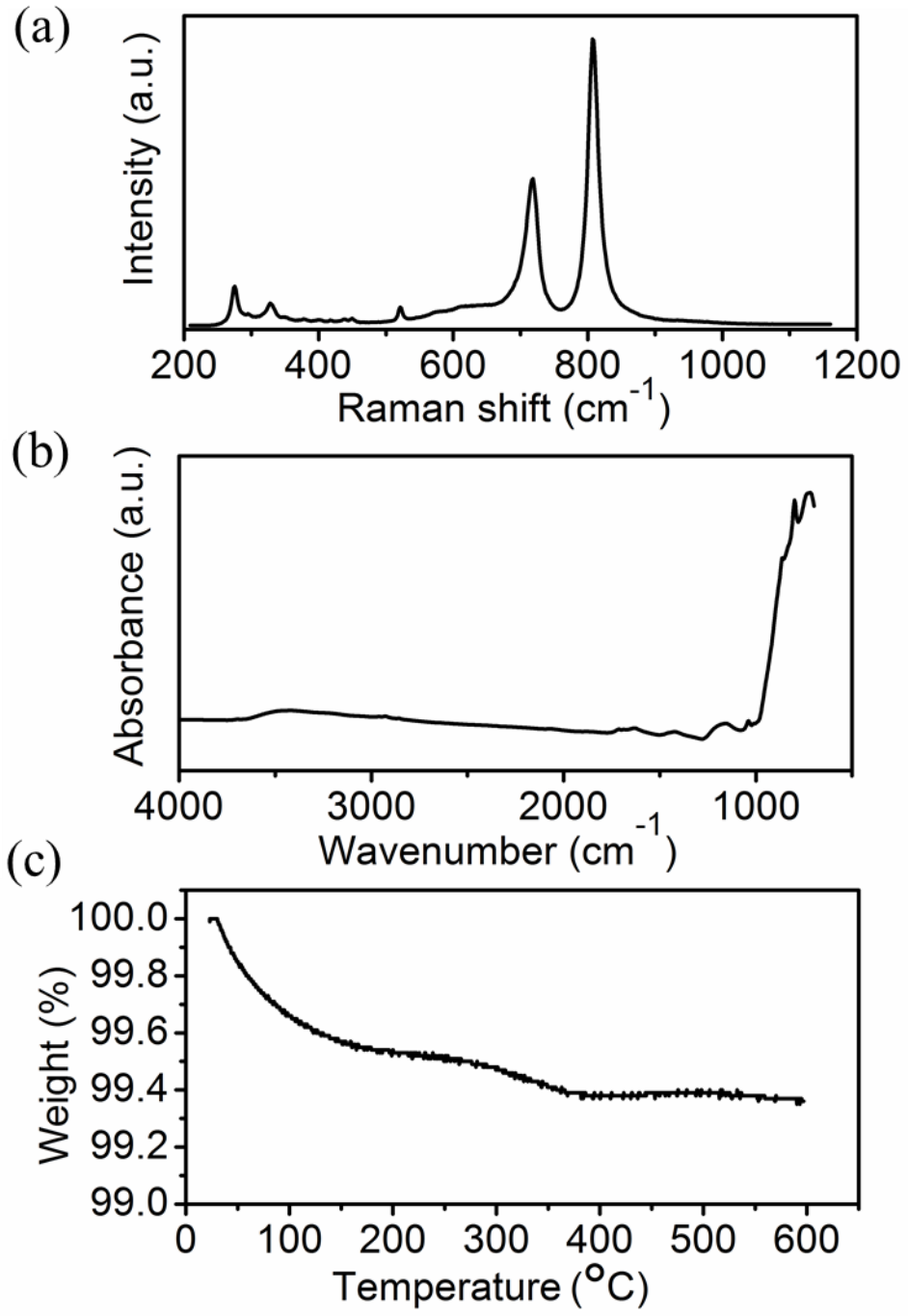

Figure S4. Analysis of possible water (potential source of protons) content in our WO_3 films. (a) Raman and (b) ATR-FTIR spectra of WO_3 films deposited on SiO_2 substrates. (c)

Thermogravimetric analysis (TGA) carried out on WO_3 powders obtained scratching the WO_3 films from the glass substrates where they were overgrown.

Comments on Figure S4

In the Raman spectrum (Figure S4a), bands at 273, 328, 716 and 810 cm^{-1} fall at the wavenumbers corresponding to the four characteristic modes of monoclinic WO_3.[1] The bands at 273 and 328 cm^{-1} correspond to O-W-O bending modes of the bridging oxygens and the bands at 716 and 810 cm^{-1} are the corresponding stretching modes. The band at 520 cm^{-1} is attributable to the SiO_2 substrate.[2] We did not observe a significant signal at 950 cm^{-1}, attributable to hydrated WO_3.[1, 3]

In the ATR-FTIR spectrum (Figure S4b), bands in the 700 to 900 cm^{-1} region correspond to W–O–W stretching modes and the bands at 1630 and around 3400 cm^{-1} region can be assigned to O-H bending and stretching modes.[3] These O-H groups likely belong to water adsorbed on the surface of WO_3. Absorption bands near 1100 cm^{-1} probably arise from the asymmetric vibration of Si–O of the SiO_2 substrate.[4]

The TGA plot (Figure S4c) shows a weight loss in two steps, the former ascribable to the loss of adsorbed water (0.5%, up to 200°C)[5] and the latter to the removal of organic matter from the WO_3 thin film sol-gel precursor (0.1%, up to 360°C). [6]

In conclusion, our Raman, ATR-FTIR and TGA measurements suggest a non-significant presence of (crystallization) water in our WO_3 films.

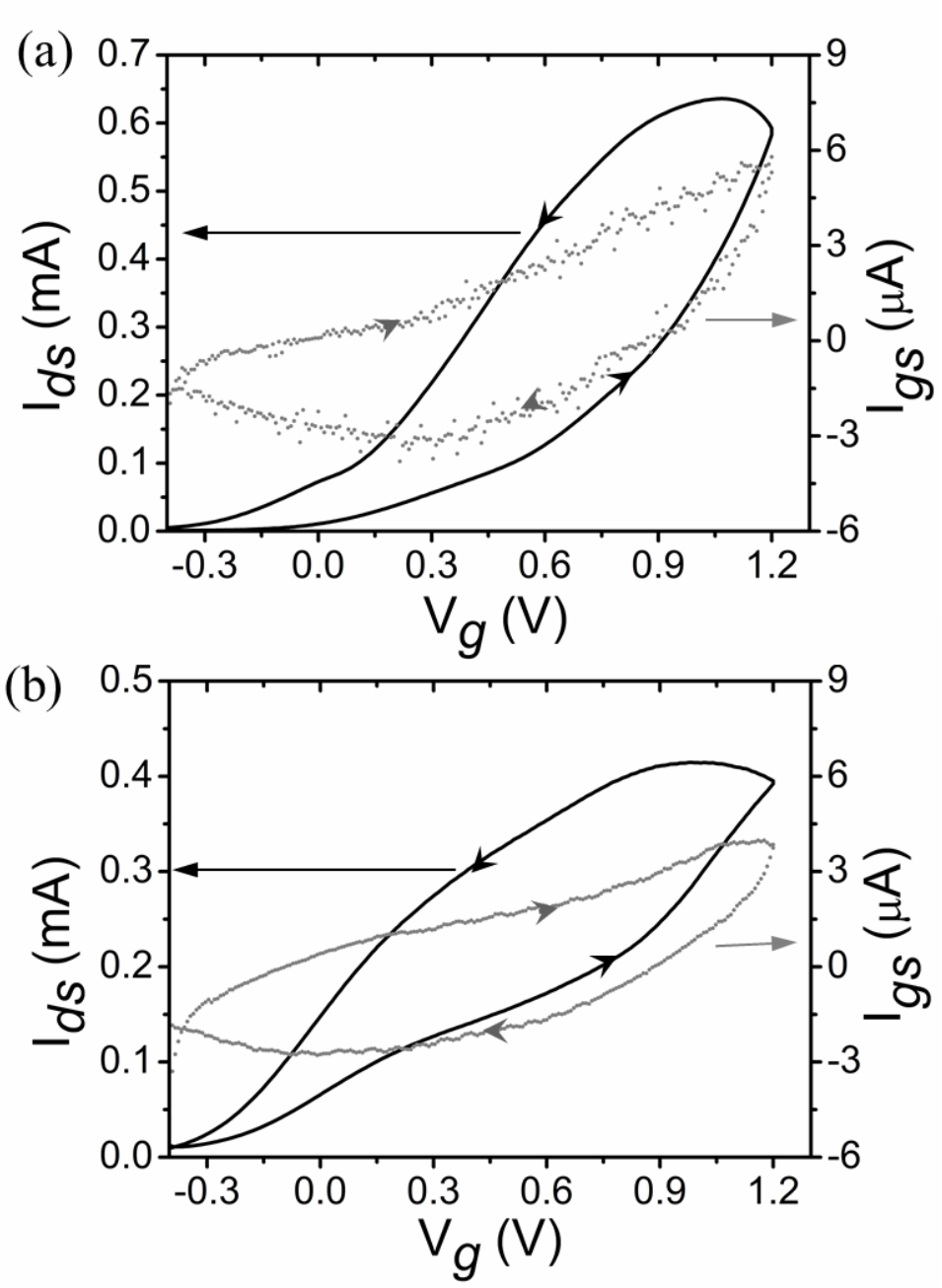

Figure S5. Transfer characteristics of (a) [EMIM][TFSI]-gated, (b) [PYR_{14}][TFSI]-gated WO_3 transistors at V_{ds} = 0.3 V, scan rate of 10 $mV \cdot s^{-1}$.

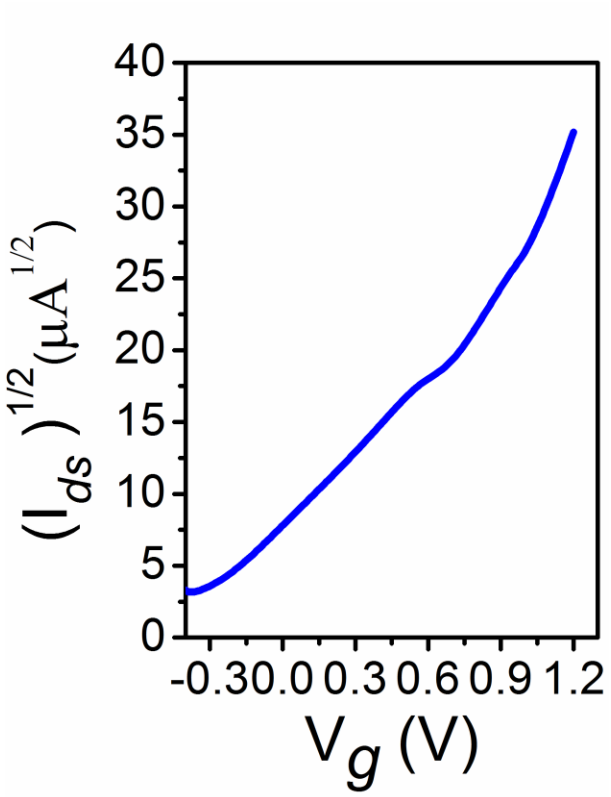

Figure S6. Transfer characteristics (forward scan) of [EMIM][TFSI]-gated WO_3 transistors at V_{ds} = 1.0 V, scan rate of 10 $mV \cdot s^{-1}$. Threshold voltage of -0.4 V.

Table S1. Comparison of the intensity of the XRD peaks: monoclinic and orthorhombic WO_3 from databases, as-prepared WO_3 films-on-ITO and WO_3 films-on-ITO after electrical biasing during 5 min at -1 V.

Monoclinic WO_3 (Ref. 7)		Orthorhombic WO_3 (Ref. 8)		As-prepared WO_3 films-on-ITO		WO_3 films-on-ITO after bias at -1 V	
2θ	I	2θ	I	2θ	I	2θ	I
23.11 23.58 24.37	100 97 99	23.08 23.70 24.09	100 65 95	23.04 23.51 24.27	61 71 100	23.00 23.50 24.23	100 50 71
26.59 28.61	19 16	26.58 28.77	10 25	26.50 28.63,	2.3 0.9	26.50 28.66	2.5 3.3
41.44 41.90	14 14	41.52	16	41.42 41.70	0.4 0.4	41.53	1.4
		49.32	20			49.27	1.6

CALCULATIONS ABOUT WEIGHT, MOLES, SURFACE AREA, VOLUME OF WO_3 AVAILABLE FOR DOPING

To calculate the number of moles *n* of WO_3 available for doping we consider the following elements. The average weight of WO_3 thick films drop-cast (without spreading) on a glass slide whose size is 75 mm × 25 mm (s=1875 mm^2) and with an average film thickness (t) of 527 nm (averaged from four different samples) is 7.8 mg. So the density (d) of our nanostructured mesoporous WO_3 films is:

$$D = weight/ (t \times s) = 7.78 \pm 0.73 \text{ mg/mm}^3$$

In this work, the geometric surface area of the WO_3 thin film transistor channel (ca 200 nm-thick) available for doping (i.e. the geometric surface area of the Durapore® GVHP membrane) is 4 mm×9 mm.

Therefore the **weight** of WO_3 (molecular weight 231.84 g/mol) available for doping is 7.78 mg/mm^3 × 200 nm × 4 mm × 9 mm = 0.056 mg.

This value corresponds to a number of **moles** 0.056 mg/(231.84 g/mol) = $2.5 \cdot 10^{-7}$ mol of WO_3 available for doping and to a **surface area** (S) of WO_3 in contact with electrolyte of 0.056 mg×14 m^2/g = 8 cm^2. For this last calculation, we used the results obtained from BET analysis, i.e. that the **specific surface area** of our nanostructured mesoporous films is 14 m^2/g.

The **volume** of WO_3 (density 7.16 g/cm^3)[9] available for doping is weight/(7.16 g/cm^3) = 0.056 mg/(7.16 g/cm^3) = $8 \cdot 10^{-6}$ cm^3.

CALCULATIONS ABOUT THE AVERAGE OXIDATION STATE CHANGE DURING CHRONOAMPEROMETRY EXPERIMENTS

The mass of WO_3 in WO_3-on-ITO electrodes analysed by XRD was ca 0.17 mg ($7.3 \cdot 10^{-7}$ mol) and the doping charges after biasing in [EMIM][TFSI] at -0.6 V and -1 V were -0.48 mC and -3 mC. These charges correspond to $7 \cdot 10^{-3}$ and $4 \cdot 10^{-2}$ electrons/WO_3 and bring the average oxidation state of W from ca +6 to +5.993 and +5.96.

CALCULATIONS ABOUT THE AVERAGE OXIDATION STATE CHANGE DURING CYCLIC VOLTAMMETRY EXPERIMENTS

The voltammetric doping charges for a cathodic scan in [EMIM][TFSI], limited at -0.5 V and -1.2 V, are -0.17 mC and -0.70 mC, respectively. These values correspond to $7 \cdot 10^{-3}$ and $3 \cdot 10^{-2}$ electrons/WO_3 and correspond to decrease in the W oxidation state from +6 to +5.993 and +5.97. It is worth noticing that these values are the average oxidation state of W. We do not expect that the redox processes happen homogeneously in the volume of the material. Redox processes are expected to happen preferentially at the interface electrolyte/WO_3. The values of the oxidation states might then be higher compared to values reported in the literature.[10, 11]

REFERENCES

1. Santato, C.; Odziemkowski, M.; Ulmann, M.; Augustynski, J., Crystallographically Oriented Mesoporous WO_3 Films: Synthesis, Characterization, and Applications. *J. Am. Chem. Soc.* **2001**, *123*, 10639-10649.

2. Camerotto, E.; De Schepper, P.; Nikiforov, A. Y.; Brems, S.; Shamiryan, D.; Boullart, W.; Leys, C.; De Gendt, S., Study of Ultrasound-Assisted Radio-Frequency Plasma Discharges in n-Dodecane. *J. Phys. D: Appl. Phys.* **2012**, *45*, 43520.

3. Daniel, M. F.; Desbat, B.; Lassegues, J. C.; Gerand, B.; Figlarz, M., Infrared and Raman Study of WO_3 Tungsten Trioxides and $WO_3 \cdot xH_2O$ Tungsten Trioxide Hydrates. *J. Solid State Chem.* **1987**, *67*, 235-247.

4. Nikabadi, H. R.; Shahtahmasebi, N.; Rokn-Abadi, M. R.; Mohagheghi, M. B.; Goharshadi, E. K., Gradual Growth of Gold Nanoseeds on Silica for SiO_2@ Gold Homogeneous Nano Core/Shell Applications by the Chemical Reduction Method. *Phys. Scr.* **2013**, *87*, 025802.

5. Li, Y. M.; Hibino, M.; Miyayania, M.; Kudo, T., Proton Conductivity of Tungsten Trioxide Hydrates at Intermediate Temperature. *Solid State Ionics* **2000**, *134*, 271-279.

6. Li, R.; Hu, F.; Bao, Q.; Bao, S.; Qiao, Y.; Yu, S.; Guo, J.; Li, C. M., Enhancement of Photoelectric Response of Bacteriorhodopsin by Multilayered $WO_3 \cdot H_2O$ Nanocrystals/PVA Membrane. *Chem. Commun.* **2010**, *46*, 689-69.

7. Grier, D.; McCarthy, G., North Dakota State University, Fargo, North Dakota, USA, ICDD Grant-in-Aid,**1991** (ICDD# 00-043-1035).

8. Roth, R. S.; Waring, J. L., Phase Equilibria as Related to Crystal Structure in the System Niobium Pentoxide–Tungsten Trioxide. *J. Res. Natl. Bur. Stand. Sect. A* **1966**, *70*, 281-303 (ICDD# 00-020-1324).

9. Deb, S. K., Optical and Photoelectric Properties and Colour Centres in Thin Films of Tungsten Oxide. *Philos. Mag.*, **1973**, *27*, 801-822.

10. Cazzanelli, E.; Vinegoni, C.; Mariotto, G.; Kuzmin, A.; Purans, J., Raman Study of the Phase Transitions Sequence in Pure WO_3 at High Temperature and in H_xWO_3 With Variable Hydrogen Content. *Solid State Ionics* **1999**, *123*, 67-74.

11. Granqvist, C. G., *Handbook of Inorganic Electrochromic Materials*. Elsevier: New York, **1995**.

APPENDIX B – SUPPORTING INFORMATION FOR ARTICLE 2

Electrolyte-Gated Phototransistors based on Tungsten Oxide Films

Xiang Meng,[1] Shiming Zhang,[2] Martin Barbosa,[1,3] Bill Baloukas,[1]Daniel Chartrand,[4] Fabio Cicoira[2] and Clara Santato [1]*

1. Département de Génie physique, Polytechnique Montréal, C.P. 6079, Succ. Centre-ville, Montréal (QC) H3C 3A7, Canada

2. Département de Génie chimique, Polytechnique Montréal, C.P. 6079, Succ. Centre-ville, Montréal (QC) H3C 3A7, Canada

3. Departamento de Físico-Química, Universidade Estadual Paulista, Rua Professor Degni, 55, Araraquara, 14800-060, Brazil

4. Département de Chimie, Université de Montréal, C. P. 6128, Succ. Centre-ville, Montréal (QC) H3C 3J7, Canada

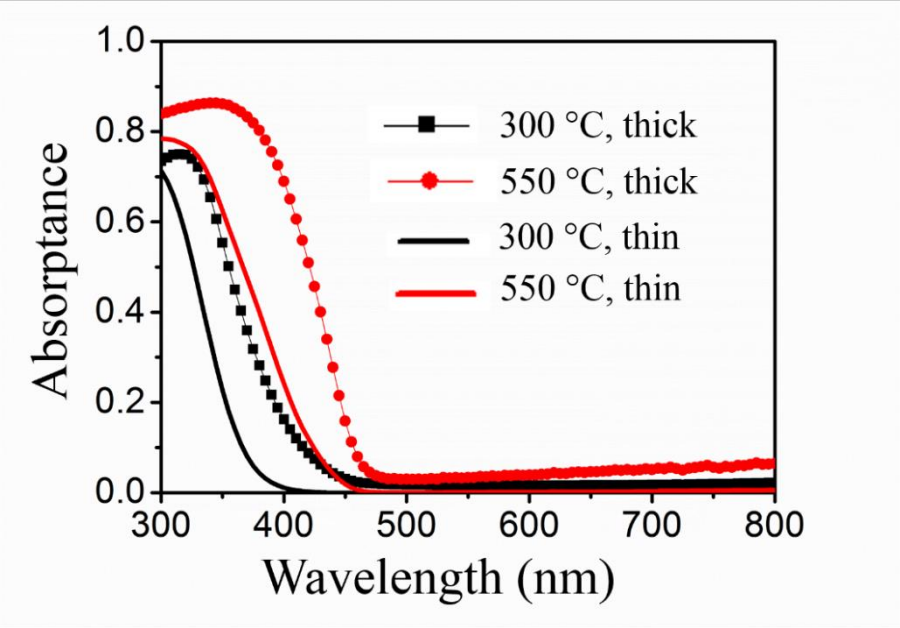

Figure S1. Absorptance of tungsten oxide films deposited on quartz with different thicknesses and temperature of thermal treatment (see also Experimental section).

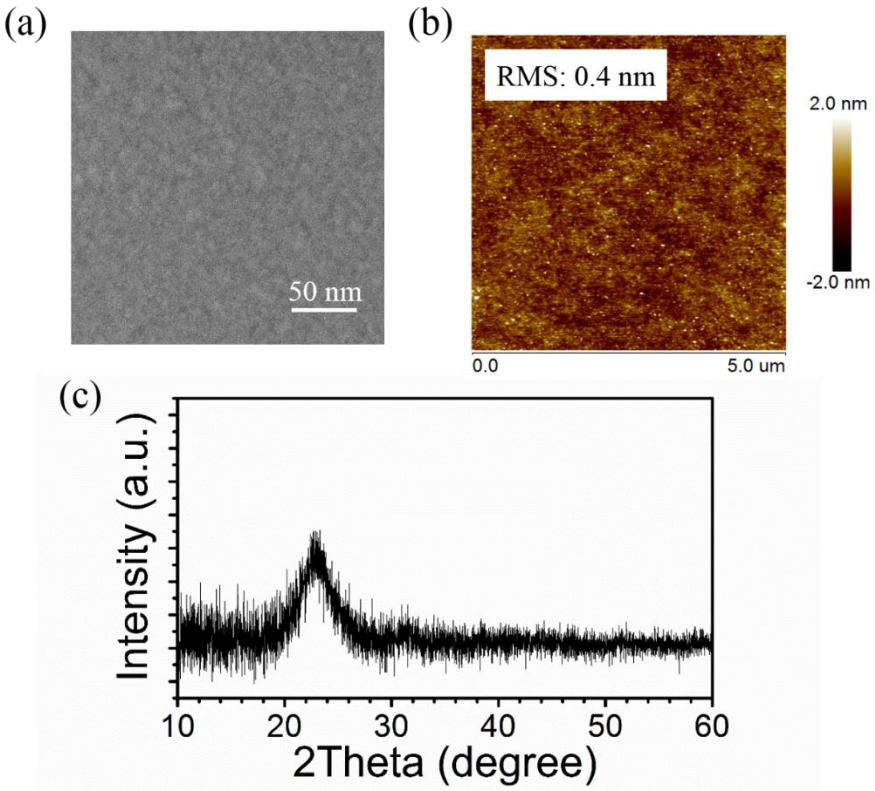

Figure S2. Tungsten oxide films (120 ± 26 nm-thick) deposited on SiO_2 substrates, thermally treated at 300 °C: (a) SEM image (10 kV); (b) AFM image and (c) XRD pattern.

Scanning electron microscopy (SEM), Atomic Force Microscopy (AFM) and X-ray diffraction (XRD) studies were performed to shed light on the morphology and structure of tungsten oxide films. Films treated at 300 °C exhibit smooth surfaces with root-mean-square (rms) surface roughness of 0.4 nm and amorphous structure. The broad peak centered at c. 23° is characteristic of SiO_2.

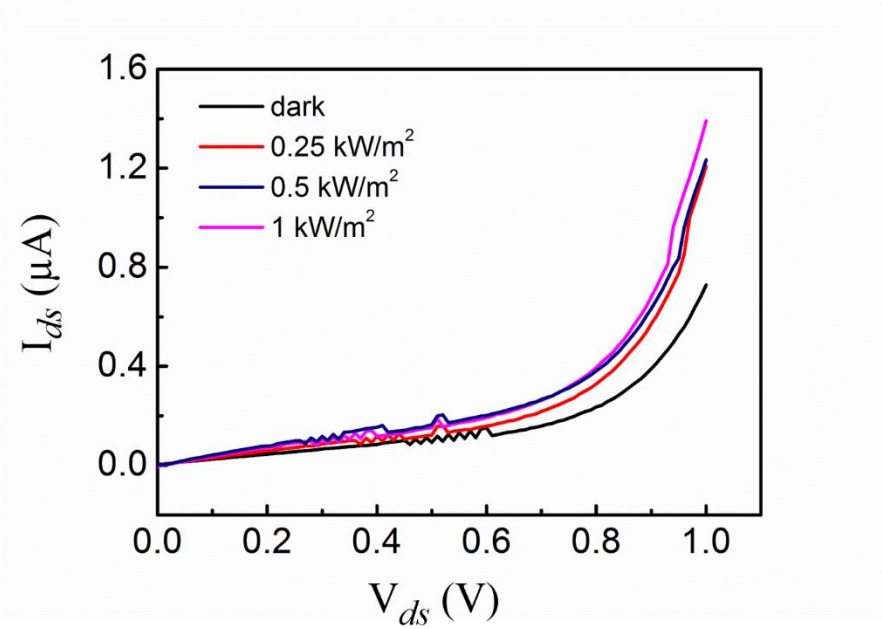

Figure S3. I_{ds}−V_{ds} curves of 300 °C-thermally treated tungsten oxide films on SiO_2 in the dark and under illumination with increasing power density, at V_g = 0 V, in vacuum.

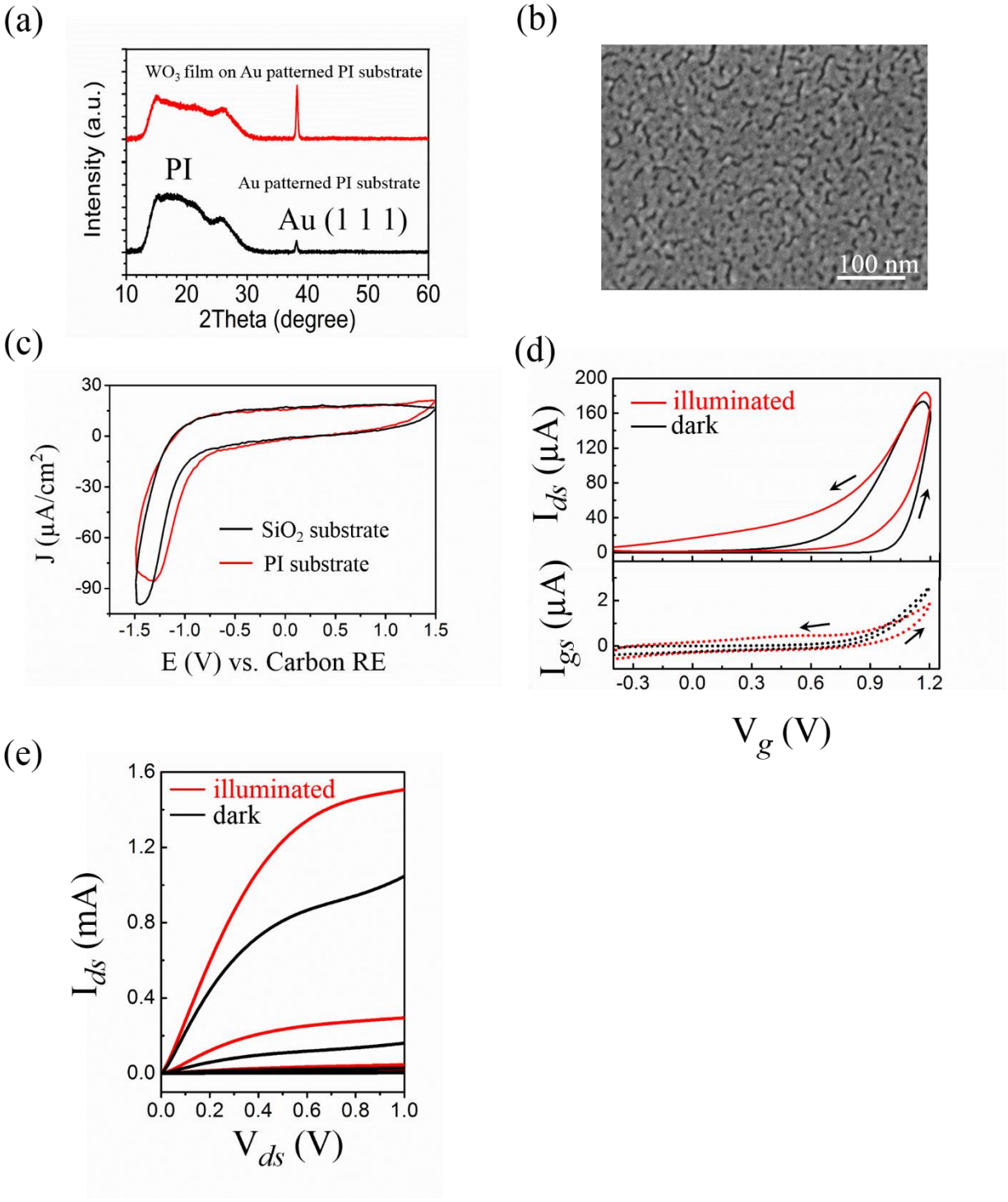

Figure S4. Tungsten oxide films (153 ± 25 nm-thick) on polyimide (PI), after treatment at 300 °C: (a) XRD patterns (the broad and the sharp signals located respectively at 2θ = 12-30° and 38° come from the PI substrate and the Au electrodes), (b) SEM image, (c) Cyclic voltammograms of the

tungsten oxide channel in transistor configuration on SiO_2 and polyimide; scan rate 50 mV/s. (d) Transfer characteristics in the linear regime ($V_{d\,s}$ = 0.2 V); V_g scan rate 10 $mV \cdot s^{-1}$; dark (black line) and illumination (red line). (e) Output characteristics in the dark and under illumination conditions, V_g = 0, 0.6, 0.8, 1.0, 1.2 V, V_{ds} scan rate is 10 $mV \cdot s^{-1}$. (c), (d) and (e) were carried out in vacuum.

Table S1. Metal oxide phototransistors: channel material, corresponding reference in the literature, type of oxide (amorphous vs crystalline etc), type of dielectric, phototransistor substrate, light to illuminate the phototransistor, responsivity (R), I_{light}/I_{dark} and operating voltages.

Channel material (reference)	**Type of channel material**	**Dielectric**	**Substrate**	**Type of light**	**R (A/W)**	**I_{light}/I_{dark}***	**Voltage**
ZnO[1]	nanofiber (crystal.)	SiO_2	SiO_2/Si	Visible 100 mW/cm^2	-	100	V_d = 50 V V_g = 50 V
ZnO[2]	-	Al_2O_3	SiO_2/Si	400-600 nm	10^{-6}	-	V_d = 3 V V_g = 6 V
ZnO-dye[3]	polycryst.	SiO_2	SiO_2/Si	Green light	10^4	10^6	V_g = 50 V
ZnO/ Graphene[4]	-	Al_2O_3-PVP	polyimide	365 nm	10^6	-	V_d = 1 V V_g = 5 V
zinc oxynitride-organic[5]	-	SiO_2	SiO_2/Si	380-940 nm 100 nW cm^{-2}	170	-	V_g = 40 V
ZITO[6]	amorphous	Ta_2O_5	glass	Deep UV	3.9	-	V_d = 2 V V_g = 2 V

$IGZO_4$[7]	amorphous	SiOx	glass	UV	-	10^4	V_d = 2 V V_g = 2 V
IGZO[8]	-	Al_2O_3	glass	370 nm	10^2	-	V_d = 1 V V_g = 5 V
IGZO[9]	amorphous	Al_2O_3	polyimide	UV		10^8	V_d = 3 V V_g = 3 V
IGZO, InZnO[10]	-	SiN/SiO_2	SiO_2/Si	<500 nm	10^4	-	V_d = 5 V V_g = 5 V
GIZO, IZO[11]	amorphous	$SiN\text{-}SiO_2$	glass	500 nm	10^4	10^7	V_d = 10 V V_g = 10 V
IGZO, Ag particle[12]	-	SiO_2	SiO_2/Si	405 nm	10^3	-	V_d = 2 V V_g = 40 V
IGZO, CdSe QDs[13]	-	SiO_2	SiO_2/Si	635 nm	10^4	-	V_d = 2 V V_g = 40 V
SnO_2[14]	single cryst. NW	SiO_2	SiO_2/Si	400-800 nm 12 $mWcm^{-2}$	-	-	V_d = 0.002 V_g =10 V
IGO[15]	amorphous	SiO_2	glass	260 nm	0.18	-	V_d = 4 V V_g = 12 V
K/ MoO_3[16]	single NW	Si_3N_4	mica	630 nm	$1.75 \cdot 10^4$	-	V_d = 10 V
$WxV_{1-x}O_2$[17]	cryst. NW	Si_3N_4	Si	532 nm	$2 \cdot 10^4$		V_d = 4 V
Mg doped In_2O_3[18]	cryst. to amorphous	SiO_2	glass	300 nm	10^4	10^8	V_d = 10 V V_g = 40 V

In_2O_3-dye[19]	-	SiO_2	SiO_2/Si	500 nm	$2 \cdot 10^3$	-	V_d = 5 V V_g = 50 V

* I_{light} is the current under illumination, I_{dark} is the current in the dark.

Table S2. Performance of electrolyte-gated phototransistors based on metal oxides with corresponding references from the literature. R is the responsivity, I_{light} is the current under illumination and I_{dark} is the current in the dark.

Channel material (reference)	**Gating medium**	**Substrate**	**Light**	**R (A/W)**	**I_{light}/I_{dark}**	**Voltage (V)**
CdSe/CdS nanoplatelets[20]	$LiClO_4$/PEG	glass	405 nm	10^{-3}	-	V_d =1 V V_g =2 V
TiO_2-dye (DSSC)[21]	Same as in DSSC	glass	AM 1.5 100 mW/cm^2	0.1	3336	V_d = 0.1 V
TiO_2-dye[22]	Same as in DSSC	glass	Xe light	-	10^4	V_c = 0.8 V V_g = -1V
ZnO[23]	$LiClO_4$/PEO	ZnO sc	UV lamp	-	1	V_d = 5 V V_g = 10 V
ZnO[24, 25]	$LiClO_4$/PEO	MgZnO+ Sapphire	365 nm	-	4.5	V_d = 5 V V_g = 5 V
ZnO[34]	$LiClO_4$/PEO	glass	365 nm	-	300	V_d = 5 V V_g = 0.5 V
ZnO[26]	$LiClO_4$/PEO	quartz	365 nm	25	10^3	V_d = 5 V V_g = 10 V

MoS_2[27]	Ionic liquid	SiO_2/Si	-	-	150	V_d = 0.1 V V_g = 2 V
MoS_2[28]	$LiClO_4$/PEO	Paper	523 nm	1500	-	V_d = 1 V V_g = 0 V
Tungsten oxide (this work)	Ionic liquid	Polyimide	390-1100 nm	10	1200	V_d = 0.2 V V_g = 1.2 V
Tungsten oxide (this work)	Ionic liquid	SiO_2/Si	390-1100 nm	12	10	V_d = 0.2 V V_g = 1.2 V

Table S3. Tungsten oxide photodetectors with corresponding literature references: type of channel material, corresponding literature reference, type of material (amorphous vs crystalline etc), quality of the light used to illuminate the transistors, device substrate, responsivity (R), $I_{light}/I_{dark,}$ and operating voltages.

Channel Material (reference)	**Type of channel material**	**Light (nm)**	**Substrate**	**R (A/W)**	**I_{light}/I_{dark}***	**Voltage**
WO_3[29]	Polycrystal.	405	SiO_2/Si	$2.6 \cdot 10^5$	1000	5 V
WO_3 nanowire[30]	Hexag. single crystal	312	-	-	172	1 V
WO_3 nanowire[31]	Monocl. single crystal	375	Carbon paper	-	1	10 V
2D WO_3 nanosheets[32]	Monoclinic	365	SiO_2/Si	293	2000	-

WO_3 nanodiscs /reduced GO[33]	Hexagonal	335	quartz	6.4	50	20 V
WO_3 nanodiscs /reduced GO[34]	-	374	-	4.2	27	20 V
WO_3 nanowire[35]	hexagonal	365	glass	-	60	1 V

* I_{light} is the current under illumination, I_{dark} is the current in the dark.

References

[1] F. Yakuphanoglu, S. Mansouri, *Microelectron Reliab* 2011, **51**, 2200.

[2] L. E. Aygun, F. B. Oruc, F. B. Atar, A. K. Okyay, *IEEE Photonics J* 2013, **5**, 2200707.

[3] P. Pattanasattayavong, S. Rossbauer, S. Thomas, J. G. Labram, H. J. Snaith, T. D. Anthopoulos, *J. Appl. Phys.* 2012, **112**, 074507.

[4] V. Q. Dang, T. Q. Trung, L. T. Duy, B.-Y. Kim, S. Siddiqui, W. Lee, N.-E. Lee, *ACS Appl. Mater. Interfaces* 2015, **7**, 11032.

[5] Y. S. Rim, K.-C. Ok, Y. M. Yang, H. Chen, S.-H. Bae, C. Wang, Y. Huang, J.-S. Park, Y. Yang, *ACS Appl. Mater. Interfaces* 2016, **8**, 14665.

[6] C. Chiu, S. Shih, W.-Y. Weng, S.-J. Chang, Z. Hung, T.-Y. Tsai, *IEEE Photon. Technol. Lett.* 2012, **24**, 1018.

[7] H.-M. Chen, T.-C. Chang, Y.-H. Tai, Y.-C. Chen, M.-C. Yang, C.-H. Chou, J.-F. Chang, S.-Z. Deng, *IEEE Trans. Electron Devices* 2014, **61**, 3186.

[8] M. G. Yun, Y. K. Kim, C. H. Ahn, S. W. Cho, W. J. Kang, H. K. Cho, Y.-H. Kim, *Sci. Rep.* 2016, **6**, 31991.

[9] S. Knobelspies, A. Daus, G. Cantarella, L. Petti, N. Münzenrieder, G. Tröster, G. A. Salvatore, *Adv. Electron. Mater.* 2016, **2**, 16000273.

[10] S. E. Ahn, S. Jeon, Y. W. Jeon, C. Kim, M. J. Lee, C. W. Lee, J. Park, I. Song, A. Nathan, S. Lee, *Adv. Mater.* 2013, **25**, 5549.

[11] S. E. Ahn, I. Song, S. Jeon, Y. W. Jeon, Y. Kim, C. Kim, B. Ryu, J. H. Lee, A. Nathan, S. Lee, *Adv. Mater.* 2012, **24**, 2631.

[12] J. Yu, S. W. Shin, K.-H. Lee, J.-S. Park, S. J. Kang, *J. Vac. Sci. Technol., B* 2015, **33**, 061211.

[13] S. W. Shin, K.-H. Lee, J.-S. Park, S. J. Kang, *ACS Appl. Mater. Interfaces* 2015, **7**, 19666.

[14] H. C. Wu, Y. C. Huang, I. Ding, C. C. Chen, Y. H. Yang, C. C. Tsai, C. D. Chen, Y. T. Chen, *Adv. Funct. Mater.* 2011, **21**, 474.

[15] T.-H. Chang, S.-J. Chang, C. Chiu, C.-Y. Wei, Y.-M. Juan, W.-Y. Weng, *IEEE Photon. Technol. Lett.* 2015, **27**, 915.

[16] J. Lu, C. Sun, M. Zheng, Y. Wang, M. Nripan, J. A. van Kan, S. G. Mhaisalkar, C. H. Sow, *J. Phys. Chem. C* 2012, **116**, 22015.

[17] J. Lu, H. Liu, S. Deng, M. Zheng, Y. Wang, J. A. Van Kan, S. H. Tang, X. Zhang, C. H. Sow, S. G. Mhaisalkar, *Nanoscale* 2014, **6**, 7619.

[18] H. Lu, X. Bi, S. Zhang, H. Zhou, *Semicond. Sci. Technol.* 2015, **30**, 125010.

[19] A. D. Mottram, Y.-H. Lin, P. Pattanasattayavong, K. Zhao, A. Amassian, T. D. Anthopoulos, *ACS Appl. Mater. Interfaces* 2016, **8**, 4894.

[20] E. Lhuillier, A. Robin, S. Ithurria, H. Aubin, B. Dubertret, *Nano Lett.* 2014, **14**, 2715.

[21] X. Wang, J. Xu, Z. Liu, Y. Lu, C. Cai, *Curr. Appl. Phys.* 2012, **12**, 147.

[22] S. Li, W. Wang, J. Xu, D. Chu, Z. J. Shen, S. Roy, *Sci. Rep.* 2013, **3**, 3391.

[23] S. Mondal, A. Raychaudhuri, *Appl. Phys. Lett.* 2011, **98**, 023501.

[24] S. Mondal, R. Ram Ghimire, A. Raychaudhuri, *Appl. Phys. Lett.* 2013, **103**, 231105.

[25] S. Mondal, R. R. Ghimire, A. Raychaudhuri, *Appl. Phys. Lett.* 2015, **106**, 041102.

[26] R. R. Ghimire, S. Mondal, A. Raychaudhuri, *J. Appl. Phys.* 2015, **117**, 105705.

[27] Z. Li, S.-W. Chang, C.-C. Chen, S. B. Cronin, *Nano Res.* 2014, **7**, 973.

[28] Q. Zhang, W. Bao, A. Gong, T. Gong, D. Ma, J. Wan, J. Dai, J. N. Munday, J.-H. He, L. Hu, *Nanoscale* 2016, **8**, 14237.

[29] Z. He, Q. Liu, H. Hou, F. Gao, B. Tang, W. Yang, *ACS Appl. Mater. Interfaces* 2015, **7**, 10878.

[30] K. Huang, Q. Zhang, F. Yang, D. He, *Nano Research* 2010, **3**, 281.

[31] L. Li, Y. Zhang, X. Fang, T. Zhai, M. Liao, X. Sun, Y. Koide, Y. Bando, D. Golberg, *J. Mater. Chem.* 2011, **21**, 6525.

[32] J. Liu, M. Zhong, J. Li, A. Pan, X. Zhu, *Mater. Lett.* 2015, **148**, 184.

[33] D. Shao, M. Yu, J. Lian, S. Sawyer, *Nanotechnology* 2013, **24**, 295701.

[34] D. Shao, M. Yu, J. Lian, S. Sawyer, Ultraviolet Photodetector Fabricated from 3D WO_3 Nanowires/Reduced Graphene Oxide Composite Material" *MRS Proceedings*, 2014.

[35] N. Huo, S. Yang, Z. Wei, J. Li, *J. Mater. Chem. C* 2013, **1**, 3999.

APPENDIX C– LIST OF PUBLICATIONS IN POLYTECHNIQUE MONTREAL NOT INCLUDED IN THE THESIS

[1] I Valitova, P Kumar, **X Meng**, F Soavi, C Santato, F Cicoira, Photolithographically Patterned TiO_2 Films for Electrolyte-Gated Transistors, *ACS Appl. Mater. Interfaces,* 2016, C 4 (7), 1382-1385.

[2] J Sayago, **X Meng**, F Quenneville, S Liang, É Bourbeau, F Soavi, F Cicoira, C Santato, Electrolyte-Gated Polymer Thin Film Transistors Making use of Ionic Liquids and Ionic LiquidSolvent Mixtures, *J. Appl. Phys.* 2015,117 (11), 112809.

APPENDIX D – PARTICIPATION AT CONFERENCES

1. **X Meng,** F Quenneville, F Soavi, C Santato; Electrolyte-Gated, WO_3 Thin Film Photo-Transistors, Oral, MRS Spring 2016, Phoenix.

2. **X Meng,** F Quenneville, A Badia, F Soavi, C Santato; Interface Investigation of Ionic Liquid-Gated WO_3 Thin Film Transistor, Poster, MRS Fall 2015, Boston.

3. **X Meng,** F Venne, F Quenneville, J Sayago, A Badia, C Santato; Metal Oxide/Electrolyte Interfaces: Unprecedented Insight by Electrochemistry and nanoIR, Oral, MRS Spring 2015, Phoenix.

4. **X Meng,** J Sayago, F Venne, A Badia, C Santato; Following the Dynamic Behaviour of Low-Voltage Electrolyte-Gated Transistors, Oral, MRS Fall 2014, Boston.

5. **X Meng,** M Barbosa, J Sayago, F Venne, M Orlandi, C Santato; Sub 1.5 V Electrolyte gated transistors based on solution processable metal oxide films, Poster, MRS Fall 2014, Boston.

6. **X Meng,** J Sayago, M Barbosa, F Soavi, F Cicoira, C Santato; Low Voltage Electrolyte-Gated Transistors Making Use of High Surface Area Activated Carbon Gate Electrodes, Poster, MRS Spring 2014, San Francisco.